Hodell, D.A., Abrantes, F., Alvarez Zarikian, C.A., and the Expedition 397 Scientists
Proceedings of the International Ocean Discovery Program Volume 397
publications.iodp.org

Site U1588[1]

F. Abrantes, D.A. Hodell, C.A. Alvarez Zarikian, H.L. Brooks, W.B. Clark, L.F.B. Dauchy-Tric, V. dos Santos Rocha, J.-A. Flores, T.D. Herbert, S.K.V. Hines, H.-H.M. Huang, H. Ikeda, S. Kaboth-Bahr, J. Kuroda, J.M. Link, J.F. McManus, B.A. Mitsunaga, L. Nana Yobo, C.T. Pallone, X. Pang, M.Y. Peral, E. Salgueiro, S. Sanchez, K. Verma, J. Wu, C. Xuan, and J. Yu[2]

[1] Abrantes, F., Hodell, D.A., Alvarez Zarikian, C.A., Brooks, H.L., Clark, W.B., Dauchy-Tric, L.F.B., dos Santos Rocha, V., Flores, J.-A., Herbert, T.D., Hines, S.K.V., Huang, H.-H.M., Ikeda, H., Kaboth-Bahr, S., Kuroda, J., Link, J.M., McManus, J.F., Mitsunaga, B.A., Nana Yobo, L., Pallone, C.T., Pang, X., Peral, M.Y., Salgueiro, E., Sanchez, S., Verma, K., Wu, J., Xuan, C., and Yu, J., 2024. Site U1588. In Hodell, D.A., Abrantes, F., Alvarez Zarikian, C.A., and the Expedition 397 Scientists, Iberian Margin Paleoclimate. Proceedings of the International Ocean Discovery Program, 397: College Station, TX (International Ocean Discovery Program). https://doi.org/10.14379/iodp.proc.397.106.2024
[2] **Expedition 397 Scientists' affiliations.**

Contents

Keywords
International Ocean Discovery Program, IODP, *JOIDES Resolution*, Expedition 397, Iberian Margin Paleoclimate, Climate and Ocean Change, Site U1588, paleo-Conductivity-Temperature-Depth, paleo-CTD, Mediterranean Outflow Water, MOW, millennial-scale, climate variability, Pleistocene

Core descriptions

Supplementary material

References (RIS)

MS 397-106
Published 11 June 2024

Funded by NSF OCE1326927, ECORD, and JAMSTEC

1. Background and objectives

Site U1588 lies on the broad, gently inclined middle-slope region of the Promontório dos Príncipes de Avis (PPA) on the southwestern Iberian margin (Figures **F1**, **F2**, **F3**, **F4**). It is the shallowest (1339 meters below sea level [mbsl]) and the closest site to the coast drilled during Expedition 397. Seismic data indicate the location is part of an extensive plastered sediment drift deposit formed under the influence of Mediterranean Outflow Water (MOW) that extends from the Gulf of Cádiz along the Portuguese margin (Hernández-Molina et al., 2003, 2006; Llave et al., 2006).

Site U1588 is positioned on Seismic Line TGS-NOPEC PD00-613 (Figures **F5**, **F6**) about 8 km northeast of the intersection with Seismic Line TGS-NOPEC PD00-510 (Figure **F7**), where the distal part of the contourite depositional system occurs as a highly expanded sedimentary record

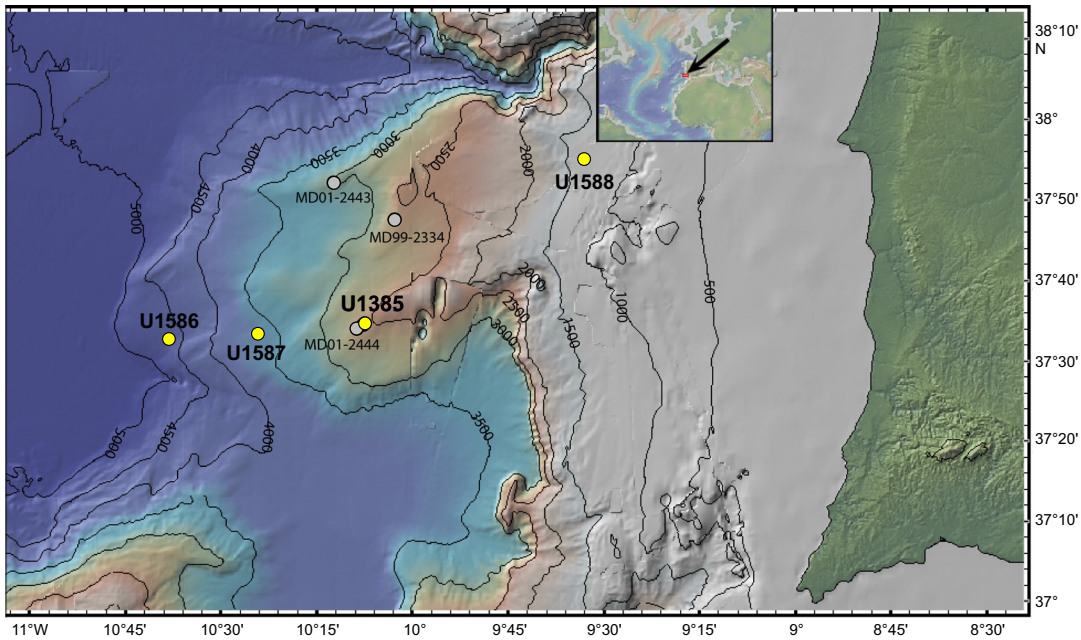

Figure F1. Location of Sites U1586, U1587, U1385, U1588, and U1391 and selected piston cores from the continental slope of the southwestern Iberian Margin. Map is modified from Hodell et al. (2023) and was made with GeoMapApp (**https://www.geomapapp.org**) using the bathymetry of Zitellini et al. (2009).

(Hernández-Molina et al., 2014). The combination of Site U1588 (1339 mbsl) and the intermediate, MOW-influenced sites drilled during Expedition 339 (560–1073 mbsl) span the full depth range of the MOW. The record of Site U1588 will be compared with the deeper sites of Expedition 397 (2591–4692 mbsl), which are removed from contourite input and are under the influence of Northeast Atlantic Deep Water (NEADW) and Lower Deep Water (LDW) (Figure **F4**). Expedition 339 and 397 sites will constitute a bathymetric transect from 560 to 4691 mbsl to be used for paleoconductivity-temperature-depth (paleo-CTD) studies.

The record at Site U1588 is expected to be similar to that of Integrated Ocean Drilling Program Site U1391, which was drilled 70 km south–southeast of Site U1588 at a water depth of 1085 mbsl (Figure **F2**). Three holes were cored and drilled to a total depth of 672 mbsf, spanning the middle Pliocene to Holocene with sedimentation rates of 13–17 cm/ky (Expedition 339 Scientists, 2013). We expected similarly high sedimentation rates at Site U1588. The high accumulation rates associated with contourite deposition provide an expanded sedimentary record to reconstruct millennial climate variability (MCV) with a resolution of a hundred years. In addition, the shallow depth of Site U1588 compared to other Expedition 397 sites is expected to yield excellent preservation of carbonate microfossils.

The primary objective of Site U1588 was to drill to 500 mbsf and recover an expanded Pliocene–Pleistocene sedimentary succession formed under the influence of lower MOW (Hernández-Molina et al., 2014). The sediments of Site U1588 and those collected during Expedition 339 pro-

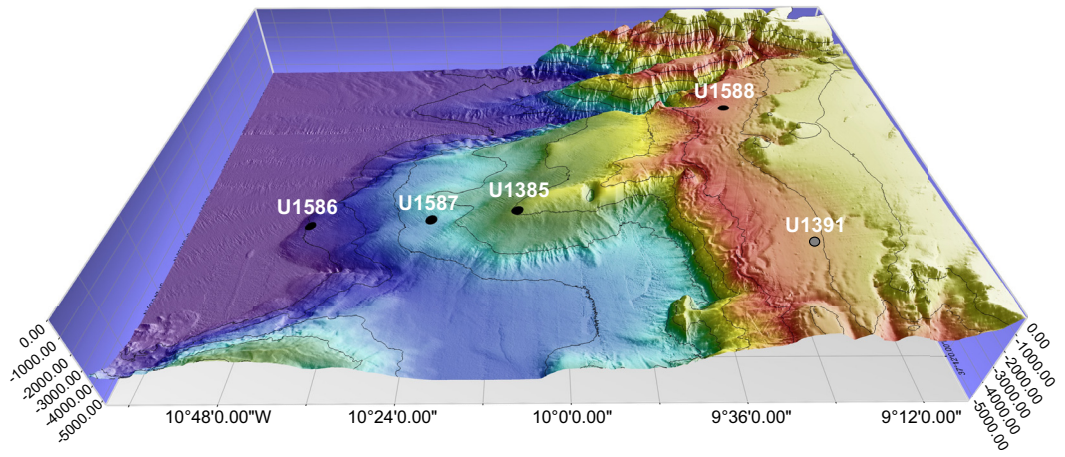

Figure F2. Bathymetric transect of Expedition 397 sites designed to simulate a paleo-CTD with which to study past changes in deep water mass structure, ventilation, and carbon storage. (Figure made by Helder Pereira using Mirone and iVew4D software).

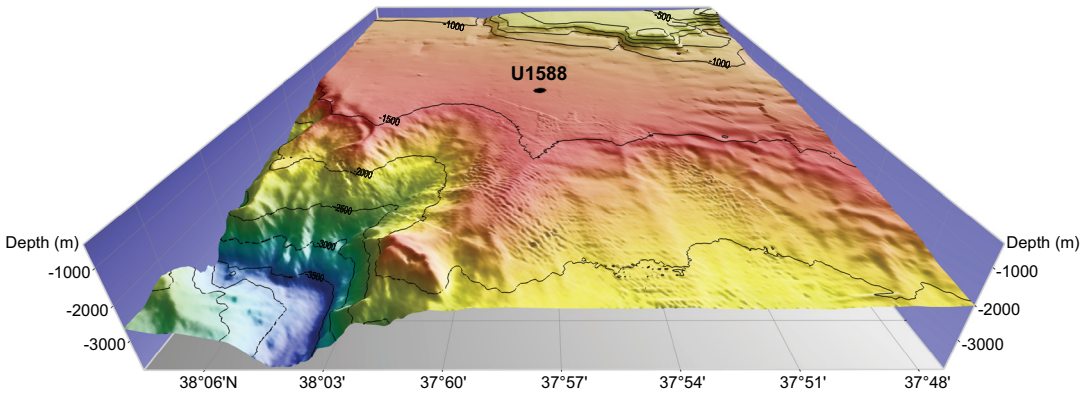

Figure F3. Location of Site U1588 on the PPA at a water depth of 1339 mbsl. See Figures F1 and F2 for broader bathymetric context. (Figure made by Helder Pereira using Mirone and iVew4D software.)

vide valuable material for studying how the depth and intensity of the MOW has varied on orbital and millennial timescales. Site U1588 will also provide a marine reference section for studying Quaternary climate variability at high stratigraphic resolution. Surface temperature proxies of Site U1588 will document MCV well beyond the base of the polar ice core. Because Site U1588 is closest to the coast, we expect preservation of terrestrial pollen and biomarkers that will allow linkage of the continental and marine records. Site U1588 should also preserve an MCV record of coastal upwelling along the Portuguese margin.

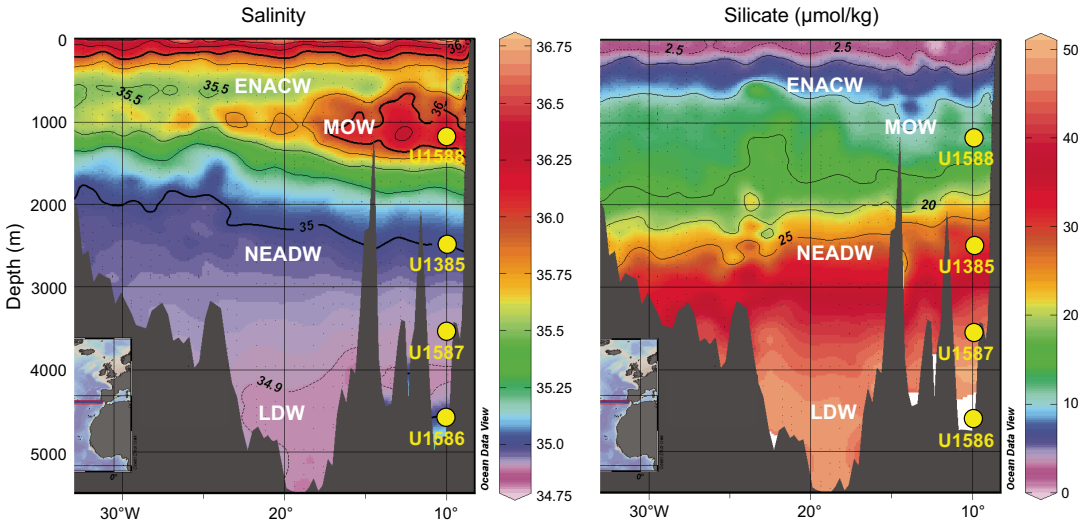

Figure F4. Salinity and silicate profiles on WOCE Line A03 (36°N) showing proposed site locations on the Iberian margin (Schlitzer, 2000). Tongue of high salinity water between 600 and 1200 m is MOW. High Si (>35 µmol/kg) below 3000 m represents a contribution from LDW sourced from the Southern Ocean. Water masses do not have clearly defined boundaries but rather consist of a series of core layers bordered by transition (mixing) zones between adjacent layers. The positions of Expedition 397 sites are shown relative to each of the identified subsurface water masses.

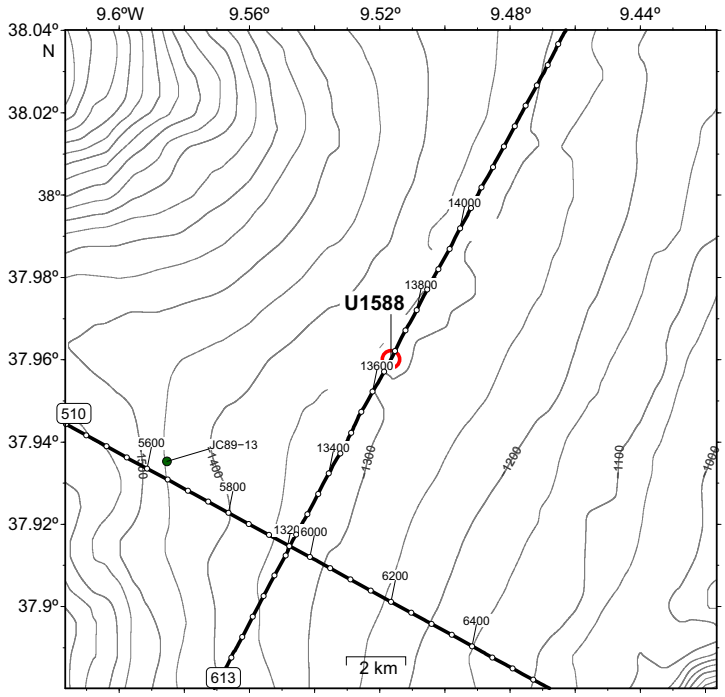

Figure F5. Bathymetric map showing Seismic Lines TGS-NOPEC PD00-613 and TGS-NOPEC PD00-510, the location of Site U1588, and Piston Core JC89-13.

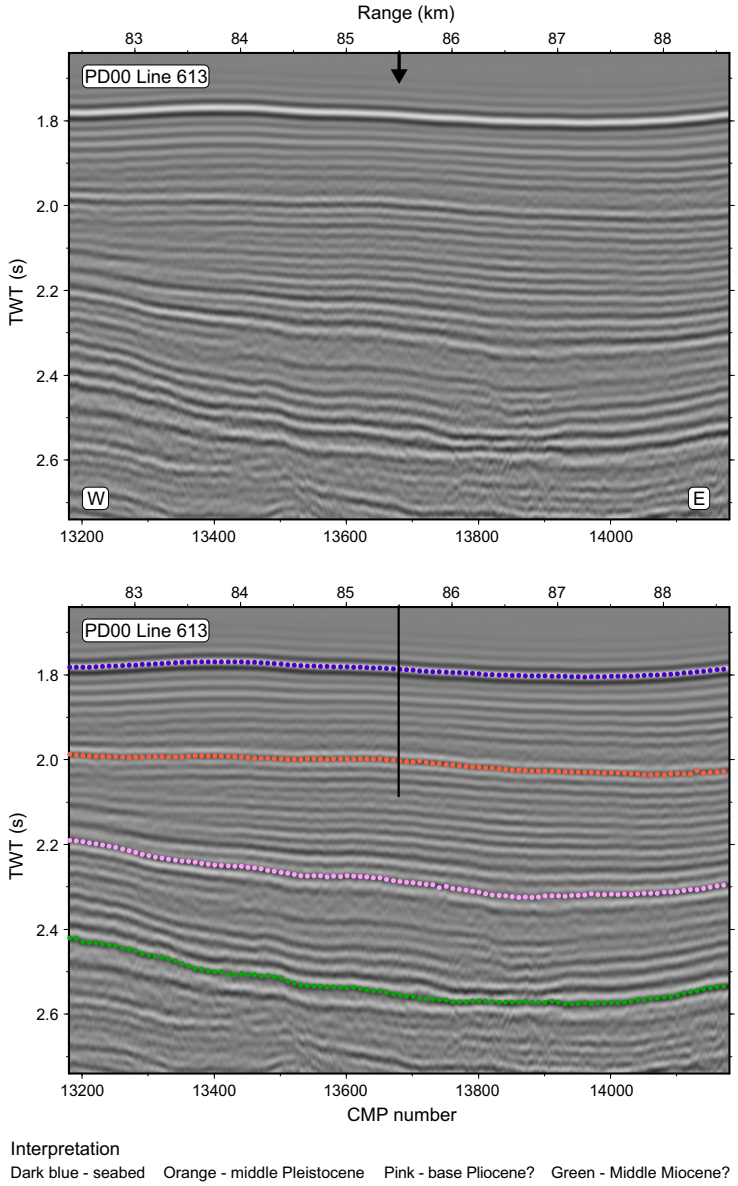

Figure F6. Original and interpreted Seismic Profile TGS-NOPEC PD00-613 showing the location of Site U1588. The depth of penetration and age of the reflectors have been revised to reflect the actual depth and age of the recovered sediment (data courtesy of TGS ASA). Penetration = ~400 mbsf. TWT = two-way traveltime, CMP = common midpoint.

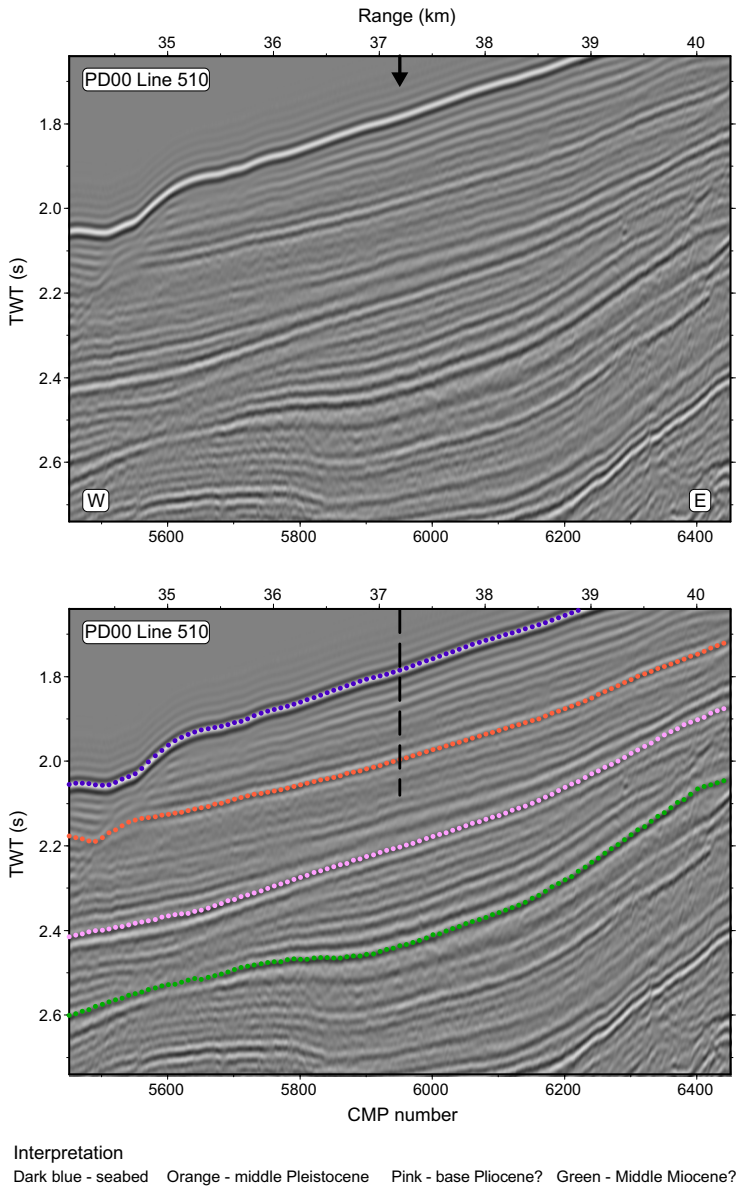

Figure F7. Original and interpreted Seismic Profile TGS-NOPEC PD00-510 showing the location of Site U1588. The depth of penetration and age of the reflectors have been revised to reflect the actual depth and age of the recovered sediment (data courtesy of TGS ASA). Penetration = ~400 mbsf. TWT = two-way traveltime, CMP = common midpoint.

2. Operations

The operational plan for Site U1588 was to core three holes to 500 mbsf (the deepest hole was to be logged with the triple combination [triple combo] tool string) and two holes to 250 mbsf with the advanced piston corer (APC) and extended core barrel (XCB) systems. Owing to time constraints toward the end of the expedition and unexpectedly high methane gas content in the cored sediments at this site, the coring plan was shortened to three holes to ~350 mbsf and a fourth hole cored as deeply as possible (412.5 mbsf) in the remaining time. Downhole logging was canceled.

Significant core expansion and curatorial difficulties encountered in Hole U1588A due to high methane gas content in the sediment led to a change in the XCB coring strategy starting with Core 397-U1588A-25X and continuing through all subsequent holes at the site. All subsequent XCB cores were taken using half advances to give the core room to expand inside the core liner as gas was released.

Holes U1588A, U1588B, and U1588D were APC cored to 154.2, 81.8, and 90.5 mbsf, respectively, and then XCB cored to their final depths. Because of deteriorating sea state, APC coring was canceled in Hole U1588C in favor of drilling ahead to 92.0 mbsf before starting to XCB core the lower section.

A total of 242 cores were taken at the site, 37 APC and 205 XCB (Table **T1**). All APC cores used nonmagnetic core barrels and were oriented using the Icefield MI-5 core orientation tool. In total, 1377.1 m was cored, recovering 1748.93 m (127%). Formation temperature measurements using the advanced piston corer temperature (APCT-3) tool were taken in Hole U1588A. Site U1588 took 186.75 h (7.8 days) to complete.

2.1. Hole U1588A

The transit from Site U1385 to Site U1588 began at 0245 h on 30 November 2022 and ended with the thrusters down and the vessel heading controlled by dynamic positioning (DP) at 0700 h. The 37.4 nmi transit was completed in 3.6 h with an average speed of 10.4 kt.

The drill crew made up an APC/XCB bottom-hole assembly (BHA), deployed the bit to 1308 meters below rig floor (mbrf), picked up the top drive, and, after spacing the bit to 1343.4 mbrf, spudded Hole U1588A (37°57.6044′N, 9°30.9961′W) at 1330 h on the same day. Based on recovery in Core 1H, the seafloor was calculated at 1339.3 mbsl. Coring continued with the APC system through Core 17H, where a partial stroke signaled APC refusal at 154.2 mbsf. The XCB system was deployed beginning with Core 18X at 154.2 mbsf. High expansion rates caused by gas in the cores led to a change in coring strategy. Beginning with Core 25X, half advances were used to allow the cores to expand in the core liner. Core expansion of 30%–40% over the cored interval was observed for the remainder of the hole. Coring was terminated at the Co-Chief Scientists' request after Core 49X at 0045 h on 2 December. The bit was pulled to the surface, clearing the seafloor at 0245 h and ending Hole U1588A. Formation temperature measurements were taken on Cores 4H (31 mbsf), 7H (59.97 mbsf), 10H (87.92 mbsf), and 13H (116.18 mbsf).

2.2. Hole U1588B

The vessel was offset 20 m north, and Hole U1588B (37°57.6149′N, 9°30.9956′W) was spudded at 0445 h on 2 December 2022 with the bit positioned at 1347.0 mbrf. Based on the 5.8 m recovered in Core 1H, the seafloor was calculated at 1339.3 mbsl. APC coring continued through Core 9H at 81.8 mbsf, where the XCB coring system was deployed to mitigate the effects of gas expansion in the cores. Cores 10X–64X were cut from 81.8 to 350.0 mbsf. Half advances were used on all XCB cores, and core expansion of 30%–40% over the cored interval was observed for all XCB cores. The bit was raised out of the hole, clearing the seafloor at 2243 h on 3 December and ending Hole U1588B. A total of 64 cores were taken over a 350 m interval (130% recovery).

2.3. Hole U1588C

After clearing the seafloor, the drill line was slipped and cut and the core winch line was cut and reheaded. The vessel was then offset 20 m east of Hole U1588B. The top drive was picked up, and the bit was spaced out for spudding. The seafloor depth was assumed to be the same as that in Holes U1588A and U1588B. Hole U1588C (37°57.6160′N, 9°30.9814′W) was spudded at 0320 h on 4 December and drilled ahead without recovery to 92.0 mbsf. The wash barrel was pulled to the surface, an XCB barrel was deployed, and coring began with Core 2X at 92.0 mbsf. Coring continued through Core 54X to a total depth of 353.6 mbsf. The bit then was raised to 1308 mbrf, clearing the seafloor at 1650 h on 5 December and ending Hole U1588C. Half advances were used on all XCB cores. A total of 53 cores were taken over a 261.6 m interval (132% recovery).

2.4. Hole U1588D

The vessel was offset 20 m south of Hole U1588C. The top drive was picked up, and the bit was spaced to 1345 mbrf. An APC core barrel was lowered, and Hole U1588D (37°57.6023′N, 9°30.9820′W) was spudded at 1845 h on 5 December 2022. The seafloor was calculated at 1338.5 mbsl based on recovery from Core 1H (4.51 m). Coring continued with the APC system to 90.5

Table T1. Core summary, Site U1588. DRF = drilling depth below rig floor, DSF = drilling depth below seafloor, HLAPC = half-length APC, RCB = rotary core barrel. (Continued on next four pages.) **Download table in CSV format.**

Hole U1588A
Latitude: 37°57.6044′N
Longitude: 9°30.9961′W
Water depth (m): 1339.3
Date started (UTC): 0600 h; 30 November 2022
Date finished (UTC): 0145 h; 2 December 2022
Time on hole (days): 1.82
Seafloor depth DRF (m): 1350.7
Seafloor depth est. method: APC Calc
Rig floor to sea level (m): 11.4
Penetration DSF (m): 353
Cored interval (m): 353
Recovered length (m): 378.37
Recovery (%): 107.19
Drilled interval (m): 0
Drilled interval (no.): 0
Total cores (no.): 49
APC cores (no.): 17
HLAPC cores (no.): 0
XCB cores (no.): 32
RCB cores (no.): 0
Other cores (no.): 0

Hole U1588B
Latitude: 37°57.6149′N
Longitude: 9°30.9956′W
Water depth (m): 1339.3
Date started (UTC): 0145 h; 2 December 2022
Date finished (UTC): 2145 h; 3 December 2022
Time on hole (days): 1.83
Seafloor depth DRF (m): 1350.7
Seafloor depth est. method: APC Calc
Rig floor to sea level (m): 11.4
Penetration DSF (m): 350
Cored interval (m): 350
Recovered length (m): 456.08
Recovery (%): 130.31
Drilled interval (m): 0
Drilled interval (no.): 0
Total cores (no.): 64
APC cores (no.): 9
HLAPC cores (no.): 0
XCB cores (no.): 55
RCB cores (no.): 0
Other cores (no.): 0

Hole U1588C
Latitude: 37°57.6160′N
Longitude: 9°30.9814′W
Water depth (m): 1339.29
Date started (UTC): 2145 h; 3 December 2022
Date finished (UTC): 1550 h; 5 December 2022
Time on hole (days): 1.75
Seafloor depth DRF (m): 1350.7
Seafloor depth est. method: Offset
Rig floor to sea level (m): 11.41
Penetration DSF (m): 353.6
Cored interval (m): 261.6
Recovered length (m): 345.04
Recovery (%): 131.9
Drilled interval (m): 92
Drilled interval (no.): 1
Total cores (no.): 53
APC cores (no.): 0
HLAPC cores (no.): 0
XCB cores (no.): 53
RCB cores (no.): 0
Other cores (no.): 0

Hole U1588D
Latitude: 37°57.6023′N
Longitude: 9°30.9820′W
Water depth (m): 1338.54
Date started (UTC): 1550 h; 5 December 2022
Date finished (UTC): 0038 h; 8 December 2022
Time on hole (days): 2.37
Seafloor depth DRF (m): 1350
Seafloor depth est. method: APC Calc
Rig floor to sea level (m): 11.46
Penetration DSF (m): 412.5
Cored interval (m): 412.5
Recovered length (m): 569.44
Recovery (%): 138.05
Drilled interval (m): 0
Drilled interval (no.): 0
Total cores (no.): 76
APC cores (no.): 11
HLAPC cores (no.): 0
XCB cores (no.): 65
RCB cores (no.): 0
Other cores (no.): 0

Core	Top depth drilled DSF (m)	Bottom depth drilled DSF (m)	Interval advanced (m)	Recovered length (m)	Curated length (m)	Core recovery (%)	Top depth cored CSF-A (m)	Bottom depth recovered CSF-A (m)	Core on deck date (2022)	Core on deck time UTC (h)	Sections (*N*)	Comments
397-U1588A-												
1H	0.0	2.2	2.2	2.18	2.18	99	0.0	2.18	30 Nov	1240	3	
2H	2.2	11.7	9.5	9.68	9.69	102	2.2	11.89	30 Nov	1325	8	
3H	11.7	21.2	9.5	9.85	9.85	104	11.7	21.55	30 Nov	1400	8	
4H	21.2	30.7	9.5	9.88	9.88	104	21.2	31.08	30 Nov	1455	8	Temperature measurement (APCT-3)
5H	30.7	40.2	9.5	9.90	9.90	104	30.7	40.60	30 Nov	1535	8	
6H	40.2	49.7	9.5	9.82	10.01	103	40.2	50.21	30 Nov	1615	8	
7H	49.7	59.2	9.5	10.12	10.27	107	49.7	59.97	30 Nov	1705	8	Temperature measurement (APCT-3)
8H	59.2	68.7	9.5	10.27	10.27	108	59.2	69.47	30 Nov	1745	8	
9H	68.7	78.2	9.5	10.18	10.18	107	68.7	78.88	30 Nov	1825	8	
10H	78.2	87.7	9.5	9.72	9.72	102	78.2	87.92	30 Nov	1925	8	Temperature measurement (APCT-3)
11H	87.7	97.2	9.5	9.69	9.69	102	87.7	97.39	30 Nov	2015	8	
12H	97.2	106.7	9.5	10.01	10.01	105	97.2	107.21	30 Nov	2150	8	
13H	106.7	116.2	9.5	9.48	9.48	100	106.7	116.18	30 Nov	2305	8	Temperature measurement (APCT-3)
14H	116.2	125.7	9.5	8.97	8.97	94	116.2	125.17	30 Nov	2350	8	
15H	125.7	135.2	9.5	9.72	9.72	102	125.7	135.42	1 Dec	0030	8	
16H	135.2	144.7	9.5	10.04	10.04	106	135.2	145.24	1 Dec	0120	9	
17H	144.7	154.2	9.5	9.63	9.63	101	144.7	154.33	1 Dec	0205	9	Partial stroke
18X	154.2	163.9	9.7	8.29	8.29	85	154.2	162.49	1 Dec	0340	7	
19X	163.9	173.6	9.7	8.12	8.12	84	163.9	172.02	1 Dec	0425	6	
20X	173.6	183.3	9.7	9.01	9.01	93	173.6	182.61	1 Dec	0505	8	
21X	183.3	193.0	9.7	9.32	9.32	96	183.3	192.62	1 Dec	0550	8	
22X	193.0	202.7	9.7	8.49	8.49	88	193.0	201.49	1 Dec	0640	8	

Table T1 (continued). (Continued on next page.)

Core	Top depth drilled DSF (m)	Bottom depth drilled DSF (m)	Interval advanced (m)	Recovered length (m)	Curated length (m)	Core recovery (%)	Top depth cored CSF-A (m)	Bottom depth recovered CSF-A (m)	Core on deck date (2022)	Core on deck time UTC (h)	Sections (*N*)	Comments
23X	202.7	212.4	9.7	7.89	7.89	81	202.7	210.59	1 Dec	0720	8	
24X	212.4	222.1	9.7	9.74	9.74	100	212.4	222.14	1 Dec	0800	9	
25X	222.1	226.9	4.8	5.88	5.88	123	222.1	227.98	1 Dec	0835	5	
26X	226.9	231.8	4.9	6.22	6.23	127	226.9	233.13	1 Dec	0915	6	
27X	231.8	236.6	4.8	5.89	5.89	123	231.8	237.69	1 Dec	0950	5	
28X	236.6	241.5	4.9	6.20	6.20	127	236.6	242.80	1 Dec	1025	5	
29X	241.5	246.3	4.8	6.36	6.36	133	241.5	247.86	1 Dec	1055	6	
30X	246.3	251.2	4.9	6.54	6.54	133	246.3	252.84	1 Dec	1140	6	
31X	251.2	256.0	4.8	5.71	5.71	119	251.2	256.91	1 Dec	1215	5	
32X	256.0	260.9	4.9	7.00	7.00	143	256.0	263.00	1 Dec	1250	6	
33X	260.9	265.7	4.8	6.38	6.38	133	260.9	267.28	1 Dec	1330	6	
34X	265.7	270.6	4.9	6.58	6.58	134	265.7	272.28	1 Dec	1409	6	
35X	270.6	275.4	4.8	5.35	5.35	111	270.6	275.95	1 Dec	1440	5	
36X	275.4	280.3	4.9	6.42	6.42	131	275.4	281.82	1 Dec	1515	6	
37X	280.3	285.1	4.8	5.99	5.99	125	280.3	286.29	1 Dec	1550	5	
38X	285.1	294.8	9.7	9.01	9.01	93	285.1	294.11	1 Dec	1630	7	
39X	294.8	299.7	4.9	6.59	6.59	134	294.8	301.39	1 Dec	1705	6	
40X	299.7	304.5	4.8	4.85	4.85	101	299.7	304.55	1 Dec	1745	5	
41X	304.5	309.4	4.9	6.86	6.86	140	304.5	311.36	1 Dec	1820	6	
42X	309.4	314.2	4.8	5.03	5.03	105	309.4	314.43	1 Dec	1900	5	
43X	314.2	323.9	9.7	9.66	9.66	100	314.2	323.86	1 Dec	1940	8	
44X	323.9	328.8	4.9	6.45	6.45	132	323.9	330.35	1 Dec	2020	6	
45X	328.8	333.6	4.8	5.71	5.71	119	328.8	334.51	1 Dec	2050	5	
46X	333.6	338.5	4.9	5.38	5.38	110	333.6	338.98	1 Dec	2130	5	
47X	338.5	343.3	4.8	6.04	6.04	126	338.5	344.54	1 Dec	2215	5	
48X	343.3	348.2	4.9	6.16	6.16	126	343.3	349.46	1 Dec	2255	5	
49X	348.2	353.0	4.8	6.11	6.11	127	348.2	354.31	1 Dec	2335	5	
	Hole U1588A totals:		353.0	378.37		107					327	
397-U1588B-												
1H	0.0	5.8	5.8	5.85	5.85	101	0.0	5.85	2 Dec	0400	5	
2H	5.8	15.3	9.5	9.85	9.85	104	5.8	15.65	2 Dec	0445	8	
3H	15.3	24.8	9.5	9.68	9.68	102	15.3	24.98	2 Dec	0520	8	
4H	24.8	34.3	9.5	9.92	9.92	104	24.8	34.72	2 Dec	0600	8	
5H	34.3	43.8	9.5	9.55	9.55	101	34.3	43.85	2 Dec	0635	8	
6H	43.8	53.3	9.5	9.92	10.10	104	43.8	53.90	2 Dec	0735	8	
7H	53.3	62.8	9.5	10.06	10.23	106	53.3	63.53	2 Dec	0810	8	
8H	62.8	72.3	9.5	10.62	10.62	112	62.8	73.42	2 Dec	0855	9	
9H	72.3	81.8	9.5	10.46	10.47	110	72.3	82.77	2 Dec	0935	9	
10X	81.8	86.6	4.8	6.47	6.47	135	81.8	88.27	2 Dec	1120	6	
11X	86.6	91.5	4.9	6.09	6.09	124	86.6	92.69	2 Dec	1155	6	
12X	91.5	96.3	4.8	7.40	7.40	154	91.5	98.90	2 Dec	1235	6	
13X	96.3	101.2	4.9	6.43	6.43	131	96.3	102.73	2 Dec	1310	6	
14X	101.2	106.0	4.8	7.79	7.79	162	101.2	108.99	2 Dec	1345	7	
15X	106.0	110.9	4.9	7.37	7.37	150	106.0	113.37	2 Dec	1415	6	
16X	110.9	115.7	4.8	7.25	7.25	151	110.9	118.15	2 Dec	1450	6	
17X	115.7	121.7	6.0	9.16	9.16	153	115.7	124.86	2 Dec	1525	8	
18X	121.7	126.7	5.0	8.35	8.36	167	121.7	130.06	2 Dec	1605	7	
19X	126.7	131.4	4.7	6.57	6.57	140	126.7	133.27	2 Dec	1635	6	
20X	131.4	136.3	4.9	7.00	7.00	143	131.4	138.40	2 Dec	1705	6	
21X	136.3	141.1	4.8	7.67	7.67	160	136.3	143.97	2 Dec	1740	7	
22X	141.1	146.0	4.9	7.30	7.30	149	141.1	148.40	2 Dec	1815	6	
23X	146.0	150.8	4.8	7.43	7.43	155	146.0	153.43	2 Dec	1850	6	
24X	150.8	155.7	4.9	6.50	6.50	133	150.8	157.30	2 Dec	1925	6	
25X	155.7	160.5	4.8	7.68	7.68	160	155.7	163.38	2 Dec	1955	7	
26X	160.5	162.5	2.0	3.11	3.11	156	160.5	163.61	2 Dec	2030	3	
27X	162.5	167.3	4.8	6.62	6.62	138	162.5	169.12	2 Dec	2240	6	
28X	167.3	172.2	4.9	8.00	8.00	163	167.3	175.30	2 Dec	2325	7	
29X	172.2	177.0	4.8	6.83	6.83	142	172.2	179.03	2 Dec	2355	6	
30X	177.0	181.9	4.9	8.40	8.40	171	177.0	185.40	3 Dec	0030	7	
31X	181.9	186.7	4.8	6.36	6.36	133	181.9	188.26	3 Dec	0100	6	
32X	186.7	191.6	4.9	7.01	7.01	143	186.7	193.71	3 Dec	0130	6	
33X	191.6	196.4	4.8	6.74	6.74	140	191.6	198.34	3 Dec	0205	6	
34X	196.4	201.3	4.9	6.72	6.72	137	196.4	203.12	3 Dec	0240	6	
35X	201.3	206.1	4.8	6.37	6.38	133	201.3	207.68	3 Dec	0310	6	
36X	206.1	211.0	4.9	7.14	7.14	146	206.1	213.24	3 Dec	0345	6	
37X	211.0	215.8	4.8	7.59	7.59	158	211.0	218.59	3 Dec	0420	6	
38X	215.8	220.7	4.9	7.05	7.05	144	215.8	222.85	3 Dec	0455	6	
39X	220.7	225.5	4.8	7.39	7.39	154	220.7	228.09	3 Dec	0530	6	
40X	225.5	230.4	4.9	6.45	6.45	132	225.5	231.95	3 Dec	0600	6	

Table T1 (continued). (Continued on next page.)

Core	Top depth drilled DSF (m)	Bottom depth drilled DSF (m)	Interval advanced (m)	Recovered length (m)	Curated length (m)	Core recovery (%)	Top depth cored CSF-A (m)	Bottom depth recovered CSF-A (m)	Core on deck date (2022)	Core on deck time UTC (h)	Sections (*N*)	Comments
41X	230.4	235.2	4.8	7.23	7.23	151	230.4	237.63	3 Dec	0635	6	
42X	235.2	240.1	4.9	7.37	7.37	150	235.2	242.57	3 Dec	0705	6	
43X	240.1	244.9	4.8	6.37	6.37	133	240.1	246.47	3 Dec	0740	6	
44X	244.9	249.8	4.9	7.06	7.06	144	244.9	251.96	3 Dec	0805	6	
45X	249.8	254.6	4.8	6.00	6.00	125	249.8	255.80	3 Dec	0840	5	
46X	254.6	259.5	4.9	6.56	6.56	134	254.6	261.16	3 Dec	0910	6	
47X	259.5	264.3	4.8	5.80	5.80	121	259.5	265.30	3 Dec	0945	5	
48X	264.3	269.2	4.9	6.63	6.63	135	264.3	270.93	3 Dec	1015	6	
49X	269.2	274.0	4.8	5.66	5.66	118	269.2	274.86	3 Dec	1045	5	
50X	274.0	278.9	4.9	6.55	6.55	134	274.0	280.55	3 Dec	1115	6	
51X	278.9	283.7	4.8	5.23	5.23	109	278.9	284.13	3 Dec	1155	5	
52X	283.7	288.6	4.9	6.76	6.76	138	283.7	290.46	3 Dec	1230	6	
53X	288.6	293.4	4.8	5.68	5.68	118	288.6	294.28	3 Dec	1300	5	
54X	293.4	298.3	4.9	6.16	6.16	126	293.4	299.56	3 Dec	1335	5	
55X	298.3	303.1	4.8	6.14	6.14	128	298.3	304.44	3 Dec	1410	5	
56X	303.1	308.0	4.9	5.69	5.69	116	303.1	308.79	3 Dec	1440	5	
57X	308.0	312.8	4.8	6.02	6.02	125	308.0	314.02	3 Dec	1515	5	
58X	312.8	317.7	4.9	6.46	6.46	132	312.8	319.26	3 Dec	1550	6	
59X	317.7	322.5	4.8	4.87	4.87	101	317.7	322.57	3 Dec	1625	5	
60X	322.5	327.4	4.9	6.25	6.25	128	322.5	328.75	3 Dec	1655	6	
61X	327.4	333.4	6.0	6.81	6.81	114	327.4	334.21	3 Dec	1750	6	
62X	333.4	338.3	4.9	5.84	5.84	119	333.4	339.24	3 Dec	1830	5	
63X	338.3	343.1	4.8	5.10	5.10	106	338.3	343.40	3 Dec	1905	5	
64X	343.1	350.0	6.9	9.69	9.69	140	343.1	352.79	3 Dec	1955	8	
	Hole U1588B totals:		350.0	456.08		130					396	
397-U1588C-												
11	0.0	92.0		*****Drilled from 0.0 to 92.0 mbsf*****					4 Dec	0555	0	
2X	92.0	96.8	4.8	5.57	5.57	116	92.0	97.57	4 Dec	0635	5	
3X	96.8	101.7	4.9	5.98	5.98	122	96.8	102.78	4 Dec	0710	5	
4X	101.7	107.7	6.0	8.78	8.78	146	101.7	110.48	4 Dec	0745	7	
5X	107.7	112.5	4.8	5.87	5.87	122	107.7	113.57	4 Dec	0810	5	
6X	112.5	117.4	4.9	6.61	6.61	135	112.5	119.11	4 Dec	0845	6	
7X	117.4	122.2	4.8	6.98	6.98	145	117.4	124.38	4 Dec	0915	6	
8X	122.2	127.1	4.9	7.03	7.03	143	122.2	129.23	4 Dec	0945	6	
9X	127.1	131.9	4.8	5.99	5.99	125	127.1	133.09	4 Dec	1015	5	
10X	131.9	136.8	4.9	5.74	5.74	117	131.9	137.64	4 Dec	1050	5	
11X	136.8	141.6	4.8	6.39	6.39	133	136.8	143.19	4 Dec	1125	6	
12X	141.6	146.5	4.9	7.50	7.50	153	141.6	149.10	4 Dec	1200	6	
13X	146.5	151.3	4.8	6.86	6.86	143	146.5	153.36	4 Dec	1235	6	
14X	151.3	156.2	4.9	7.47	7.47	152	151.3	158.77	4 Dec	1305	6	
15X	156.2	161.0	4.8	7.79	7.79	162	156.2	163.99	4 Dec	1340	7	
16X	161.0	165.9	4.9	7.03	7.03	143	161.0	168.03	4 Dec	1420	6	
17X	165.9	170.7	4.8	6.39	6.39	133	165.9	172.29	4 Dec	1450	6	
18X	170.7	175.6	4.9	7.12	7.12	145	170.7	177.82	4 Dec	1520	6	
19X	175.6	180.4	4.8	7.30	7.30	152	175.6	182.90	4 Dec	1600	6	
20X	180.4	185.3	4.9	7.27	7.27	148	180.4	187.67	4 Dec	1625	6	
21X	185.3	190.1	4.8	6.23	6.23	130	185.3	191.53	4 Dec	1700	6	
22X	190.1	195.0	4.9	6.99	6.99	143	190.1	197.09	4 Dec	1730	6	
23X	195.0	199.8	4.8	6.60	6.60	138	195.0	201.60	4 Dec	1805	6	
24X	199.8	204.7	4.9	7.17	7.17	146	199.8	206.97	4 Dec	1840	6	
25X	204.7	209.5	4.8	5.42	5.43	113	204.7	210.13	4 Dec	1915	5	
26X	209.5	214.4	4.9	6.07	6.07	124	209.5	215.57	4 Dec	1950	5	
27X	214.4	219.2	4.8	5.88	5.88	123	214.4	220.28	4 Dec	2030	5	
28X	219.2	224.1	4.9	6.82	6.82	139	219.2	226.02	4 Dec	2110	6	
29X	224.1	228.9	4.8	5.25	5.25	109	224.1	229.35	4 Dec	2145	5	
30X	228.9	233.8	4.9	6.44	6.44	131	228.9	235.34	4 Dec	2230	6	
31X	233.8	238.6	4.8	7.05	7.05	147	233.8	240.85	4 Dec	2310	6	
32X	238.6	243.5	4.9	5.21	5.21	106	238.6	243.81	4 Dec	2345	5	
33X	243.5	248.3	4.8	6.63	6.64	138	243.5	250.14	5 Dec	0020	6	
34X	248.3	253.2	4.9	6.55	6.55	134	248.3	254.85	5 Dec	0100	6	
35X	253.2	258.0	4.8	6.18	6.18	129	253.2	259.38	5 Dec	0135	6	
36X	258.0	262.9	4.9	6.56	6.56	134	258.0	264.56	5 Dec	0215	6	
37X	262.9	267.7	4.8	6.57	6.57	137	262.9	269.47	5 Dec	0250	6	
38X	267.7	272.6	4.9	6.36	6.36	130	267.7	274.06	5 Dec	0325	5	
39X	272.6	278.6	6.0	7.71	7.71	129	272.6	280.31	5 Dec	0415	7	
40X	278.6	284.6	6.0	9.38	9.38	156	278.6	287.98	5 Dec	0510	8	
41X	284.6	289.4	4.8	5.53	5.53	115	284.6	290.13	5 Dec	0545	5	
42X	289.4	294.3	4.9	6.04	6.04	123	289.4	295.44	5 Dec	0620	5	

Table T1 (continued). (Continued on next page.)

Core	Top depth drilled DSF (m)	Bottom depth drilled DSF (m)	Interval advanced (m)	Recovered length (m)	Curated length (m)	Core recovery (%)	Top depth cored CSF-A (m)	Bottom depth recovered CSF-A (m)	Core on deck date (2022)	Core on deck time UTC (h)	Sections (*N*)	Comments
43X	294.3	299.1	4.8	6.01	6.01	125	294.3	300.31	5 Dec	0655	5	
44X	299.1	304.0	4.9	6.72	6.72	137	299.1	305.82	5 Dec	0730	6	
45X	304.0	308.8	4.8	6.40	6.40	133	304.0	310.40	5 Dec	0800	5	
46X	308.8	313.7	4.9	6.64	6.64	136	308.8	315.44	5 Dec	0840	6	
47X	313.7	318.5	4.8	5.08	5.08	106	313.7	318.78	5 Dec	0915	5	
48X	318.5	323.4	4.9	5.83	5.83	119	318.5	324.33	5 Dec	0945	5	
49X	323.4	328.2	4.8	5.39	5.39	112	323.4	328.79	5 Dec	1020	5	
50X	328.2	333.1	4.9	6.34	6.34	129	328.2	334.54	5 Dec	1055	6	
51X	333.1	337.9	4.8	4.93	4.93	103	333.1	338.03	5 Dec	1135	5	
52X	337.9	342.8	4.9	7.19	7.19	147	337.9	345.09	5 Dec	1210	6	
53X	342.8	347.6	4.8	5.04	5.04	105	342.8	347.84	5 Dec	1245	5	
54X	347.6	353.6	6.0	7.16	7.16	119	347.6	354.76	5 Dec	1330	6	
		Hole U1588C totals:	115.0	145.45		126					303	
397-U1588D-												
1H	0.0	4.5	4.5	4.51	4.51	100	0.0	4.51	5 Dec	1755	4	Nonmag. core barrels, core orientation
2H	4.5	14.0	9.5	9.72	9.71	102	4.5	14.21	5 Dec	1845	8	Nonmag. core barrels, core orientation
3H	14.0	23.5	9.5	9.85	9.85	104	14.0	23.85	5 Dec	1920	8	Nonmag. core barrels, core orientation
4H	23.5	33.0	9.5	9.79	9.78	103	23.5	33.28	5 Dec	2005	8	Nonmag. core barrels, core orientation
5H	33.0	37.0	4.0	6.37	6.36	159	33.0	39.36	5 Dec	2045	6	Nonmag. core barrels, core orientation
6H	37.0	46.5	9.5	9.90	10.03	104	37.0	47.03	5 Dec	2125	8	Nonmag. core barrels, core orientation
7H	46.5	56.0	9.5	10.08	10.18	106	46.5	56.68	5 Dec	2245	8	Nonmag. core barrels, core orientation
8H	56.0	65.5	9.5	10.34	10.4	109	56.0	66.40	5 Dec	2325	8	Nonmag. core barrels, core orientation
9H	65.5	75.0	9.5	10.47	10.12	110	65.5	75.62	6 Dec	0045	8	Nonmag. core barrels, core orientation
10H	75.0	84.5	9.5	10.68	10.37	112	75.0	85.37	6 Dec	0125	9	Nonmag. core barrels, core orientation
11H	84.5	90.5	6.0	7.39	7.16	123	84.5	91.66	6 Dec	0210	7	Nonmag. core barrels, core orientation
12X	90.5	95.3	4.8	6.88	6.88	143	90.5	97.38	6 Dec	0240	6	
13X	95.3	100.2	4.9	7.51	7.51	153	95.3	102.81	6 Dec	0310	6	
14X	100.2	105.0	4.8	8.47	8.47	176	100.2	108.67	6 Dec	0415	7	
15X	105.0	109.9	4.9	7.59	7.59	155	105.0	112.59	6 Dec	0445	6	
16X	109.9	114.7	4.8	8.63	8.63	180	109.9	118.53	6 Dec	0520	7	
17X	114.7	119.6	4.9	6.77	6.77	138	114.7	121.47	6 Dec	0555	6	
18X	119.6	124.4	4.8	7.70	7.70	160	119.6	127.30	6 Dec	0625	7	
19X	124.4	129.3	4.9	8.29	8.29	169	124.4	132.69	6 Dec	0700	7	
20X	129.3	134.1	4.8	7.52	7.52	157	129.3	136.82	6 Dec	0735	6	
21X	134.1	139.0	4.9	7.32	7.32	149	134.1	141.42	6 Dec	0805	6	
22X	139.0	143.8	4.8	7.64	7.64	159	139.0	146.64	6 Dec	0835	6	
23X	143.8	148.7	4.9	7.03	7.04	143	143.8	150.84	6 Dec	0905	6	
24X	148.7	153.5	4.8	6.43	6.43	134	148.7	155.13	6 Dec	0950	6	
25X	153.5	158.4	4.9	7.97	7.98	163	153.5	161.48	6 Dec	1025	7	
26X	158.4	164.4	6.0	7.96	7.96	133	158.4	166.36	6 Dec	1055	7	
27X	164.4	169.3	4.9	6.90	6.90	141	164.4	171.30	6 Dec	1130	6	
28X	169.3	174.1	4.8	7.84	7.84	163	169.3	177.14	6 Dec	1200	7	
29X	174.1	179.0	4.9	7.10	7.10	145	174.1	181.20	6 Dec	1235	6	
30X	179.0	183.8	4.8	7.03	7.03	146	179.0	186.03	6 Dec	1310	6	
31X	183.8	188.7	4.9	7.20	7.20	147	183.8	191.00	6 Dec	1345	6	
32X	188.7	193.5	4.8	7.32	7.32	153	188.7	196.02	6 Dec	1420	6	
33X	193.5	198.4	4.9	7.10	7.10	145	193.5	200.60	6 Dec	1455	6	
34X	198.4	203.2	4.8	7.21	7.21	150	198.4	205.61	6 Dec	1530	6	
35X	203.2	208.1	4.9	6.63	6.63	135	203.2	209.83	6 Dec	1600	6	
36X	208.1	212.9	4.8	6.71	6.71	140	208.1	214.81	6 Dec	1635	6	
37X	212.9	217.8	4.9	7.83	7.83	160	212.9	220.73	6 Dec	1710	7	
38X	217.8	222.6	4.8	7.46	7.46	155	217.8	225.26	6 Dec	1745	6	
39X	222.6	227.5	4.9	8.03	8.03	164	222.6	230.63	6 Dec	1820	7	
40X	227.5	232.3	4.8	8.13	8.13	169	227.5	235.63	6 Dec	1855	7	
41X	232.3	237.2	4.9	6.61	6.61	135	232.3	238.91	6 Dec	1930	6	
42X	237.2	242.0	4.8	6.18	6.18	129	237.2	243.38	6 Dec	2005	5	
43X	242.0	246.9	4.9	7.36	7.36	150	242.0	249.36	6 Dec	2040	6	
44X	246.9	251.7	4.8	7.13	7.13	149	246.9	254.03	6 Dec	2110	6	
45X	251.7	256.6	4.9	5.91	5.91	121	251.7	257.61	6 Dec	2145	5	
46X	256.6	261.4	4.8	6.82	6.82	142	256.6	263.42	6 Dec	2225	6	
47X	261.4	267.4	6.0	7.65	7.65	128	261.4	269.05	6 Dec	2305	6	
48X	267.4	272.2	4.8	5.97	5.97	124	267.4	273.37	6 Dec	2340	5	
49X	272.2	277.1	4.9	7.37	7.37	150	272.2	279.57	7 Dec	0015	6	
50X	277.1	281.9	4.8	7.89	7.89	164	277.1	284.99	7 Dec	0055	7	
51X	281.9	286.8	4.9	7.29	7.29	149	281.9	289.19	7 Dec	0130	6	
52X	286.8	291.6	4.8	5.80	5.80	121	286.8	292.60	7 Dec	0210	5	
53X	291.6	297.6	6.0	7.47	7.47	125	291.6	299.07	7 Dec	0300	6	
54X	297.6	302.5	4.9	8.14	8.14	166	297.6	305.74	7 Dec	0330	7	
55X	302.5	307.3	4.8	7.05	7.05	147	302.5	309.55	7 Dec	0410	6	

Table T1 (continued).

Core	Top depth drilled DSF (m)	Bottom depth drilled DSF (m)	Interval advanced (m)	Recovered length (m)	Curated length (m)	Core recovery (%)	Top depth cored CSF-A (m)	Bottom depth recovered CSF-A (m)	Core on deck date (2022)	Core on deck time UTC (h)	Sections (*N*)	Comments
56X	307.3	312.2	4.9	8.91	8.91	182	307.3	316.21	7 Dec	0445	7	
57X	312.2	317.0	4.8	6.64	6.64	138	312.2	318.84	7 Dec	0520	6	
58X	317.0	323.0	6.0	8.41	8.41	140	317.0	325.41	7 Dec	0555	7	
59X	323.0	327.9	4.9	7.19	7.19	147	323.0	330.19	7 Dec	0630	6	
60X	327.9	332.7	4.8	6.08	6.08	127	327.9	333.98	7 Dec	0705	5	
61X	332.7	337.6	4.9	7.60	7.60	155	332.7	340.30	7 Dec	0740	6	
62X	337.6	342.4	4.8	7.72	7.72	161	337.6	345.32	7 Dec	0815	6	
63X	342.4	347.3	4.9	6.43	6.43	131	342.4	348.83	7 Dec	0855	6	
64X	347.3	352.1	4.8	6.36	6.36	133	347.3	353.66	7 Dec	0925	6	
65X	352.1	357.0	4.9	6.02	6.02	123	352.1	358.12	7 Dec	0955	5	
66X	357.0	361.8	4.8	5.79	5.79	121	357.0	362.79	7 Dec	1030	5	
67X	361.8	366.7	4.9	7.95	7.95	162	361.8	369.75	7 Dec	1105	7	
68X	366.7	371.5	4.8	7.10	7.10	148	366.7	373.80	7 Dec	1145	6	
69X	371.5	376.4	4.9	5.75	5.75	117	371.5	377.25	7 Dec	1225	5	
70X	376.4	381.2	4.8	7.93	7.93	165	376.4	384.33	7 Dec	1300	7	
71X	381.2	386.1	4.9	6.58	6.58	134	381.2	387.78	7 Dec	1340	6	
72X	386.1	390.9	4.8	6.33	6.33	132	386.1	392.43	7 Dec	1420	5	
73X	390.9	395.8	4.9	6.32	6.32	129	390.9	397.22	7 Dec	1455	5	
74X	395.8	400.6	4.8	7.60	7.60	158	395.8	403.40	7 Dec	1530	6	
75X	400.6	405.5	4.9	7.21	7.21	147	400.6	407.81	7 Dec	1610	6	
76X	405.5	412.5	7.0	9.58	9.58	137	405.5	415.08	7 Dec	1700	8	
	Hole U1588D totals:		412.5	569.44				138.00			480	

mbsf with Core 11H. An XCB barrel was deployed, and coring continued to 421.5 mbsf (Cores 12X–76X) at 1800 h on 7 December, when coring was terminated to prepare for departure. The bit was then pulled out of the hole, clearing the seafloor at 2050 h on 7 December. The rig floor was secured for transit at 0138 h on 8 December, ending Hole U1588D and Site U1588. A total of 76 cores were taken over a 412.5 m interval, and the APC system was used for 11 cores over 90.5 m (110% recovery). The XCB system was deployed for 65 cores over a 322.0 m interval (146% recovery), and half advances were used to mitigate core disturbance caused by gas.

The thrusters were raised, and at 0224 h on 8 December the R/V *JOIDES Resolution* began the sea passage to Tarragona, Spain. The 783 nmi transit was completed on 11 December 2022 at 0700 h with the first line ashore at Muelle de Baleares in Tarragona, Spain.

3. Lithostratigraphy

Three lithofacies were identified using visual descriptions, smear slides, and color (RGB values). The majority of sediments are characterized as Lithofacies 1 and 2, which can be represented as mixed ratio of two end-members: Lithofacies 1 (100% nannofossil ooze) and Lithofacies 2 (100% clay/silt). Lithofacies 3 is minor in occurrence and consists of sediments mainly composed of carbonate grains. One lithostratigraphic unit was defined. Unit I spans 0–412.5 m core depth below seafloor, Method B (CSF-B). Most sediments from Site U1588 are from Lithofacies 1 and contain varying amounts of inorganic/detrital/recrystallized calcium carbonate of indeterminate origin (hereafter carbonate) and clay. The abundance of nannofossil ooze with substantial amounts of clay and carbonate indicates the persistence of hemipelagic sedimentation and an indeterminate (recrystallized or detrital) source of carbonate at Site U1588 through the Pleistocene. Foraminifers, diagenetic features (dark patches, pyrite), and rare, subtle color banding are disseminated throughout the cores. Bioturbation varies from absent to heavy and generally increases downhole. Deformational sedimentary structures are rare and, when present, are at a decimeter scale. Drilling disturbance is present in most cores in all holes, varies from slight to severe, and is influenced by the drilling type, operation conditions, and methane gas contents of sediments.

3.1. Introduction

Three lithofacies were identified using visual observation of sediments, microscopic examination of smear slides, and RGB data, complemented with X-ray diffraction (XRD) and carbonate analy-

ses and compared to the sediment physical properties. The sediments are categorized into three lithofacies according to their primary lithologies: nannofossil ooze, clay, and carbonate. In Hole U1588A, two smear slides were taken per APC and full-advance XCB core (9.7 m) and one was taken per half-advance XCB core (4.9 m). Additional smear slides were taken when necessary to confirm lithologies in Holes U1588B–U1588D. To complement smear slide analysis and visual descriptions, two $CaCO_3$ samples and one XRD sample were taken per APC core and full-advance XCB Cores 397-U1588A-1H through 24X, one $CaCO_3$ sample was taken per half-advance XCB Cores 25X–49X, and one XRD sample was taken from each of the even-numbered half-advance XCB cores in Hole U1588A.

Site U1588 consists of one lithostratigraphic unit that spans the Quaternary to the Pleistocene. The dominant principal lithology of Unit I is nannofossil ooze. Lithologies vary between generally darker intervals of nannofossil ooze with varying amounts of clay to generally lighter intervals consisting of nannofossil ooze. Cyclicity between these lithologies is seen in color reflectance and physical properties data, including natural gamma radiation (NGR), magnetic susceptibility (MS), and L* (see **Physical properties**).

Based on constraints from biostratigraphy and paleomagnetic data, the basal ages of Holes U1588A–U1588C are estimated at 1.9 Ma and the basal age of Hole U1588D is estimated at ~2.2 Ma. The average sedimentation rate at Site U1588 is estimated at ~18 cm/ky based on onboard age models (see **Biostratigraphy**). No major deformational structures were observed across or within holes, and decimeter-scale features are found in only a few sections. Drilling disturbance was present throughout many cores in all holes, was slight to severe, and varied with the drilling type, sea conditions, and methane content of sediments, with gas expansion as the most prominent disturbance.

3.2. Lithofacies description

Three lithofacies were identified at Site U1588 (Table T2). Lithofacies 1 and 2 can be represented as a mixing ratio of two end-members: 100% nannofossil ooze and 100% clay comprising a range of siliciclastic constituents. Lithofacies 3 is primarily carbonate with a variable secondary proportion of nannofossil ooze and clay. By far the most common sediments at Site U1588 are from Lithofacies 1. Lithofacies 2 and 3 only occur in a few sections (Lithofacies 2 = Sections 397-U1588A-19X-2 and 21X-2; Lithofacies 3 = Sections 6H-7, 9H-3, 23X-4, 24X-1 through 24X-4, 24X-7, 25X-4, and 25X-CC), constituting ~1% and ~3% of lithologies, respectively, at Site U1588.

3.2.1. Lithofacies 1

Lithofacies 1 consists principally of nannofossil ooze with varying amounts of clay, detrital carbonate, and diatoms. Lithologies in this lithofacies are clayey nannofossil ooze with carbonate, nannofossil ooze with carbonate, nannofossil ooze with carbonate and clay, nannofossil ooze with clay, carbonate nannofossil ooze with clay, carbonate nannofossil ooze, diatom nannofossil ooze,

Table T2. Lithofacies 1, 2, and 3, Site U1588. Common lithologic names include prefixes (25%–50%) and suffixes (10%–25%). **Download table in CSV format.**

Lithofacies	No.	Common lithologies	Description	Lithofacies thickness (m)	Degree of bioturbation	Color	Proportion in lith. unit	Depositional environment
Nannofossil ooze	1	Clayey nannofossil ooze with carbonate; nannofossil ooze with carbonate; nannofossil ooze with carbonate and clay; nannofossil ooze with clay; carbonate nannofossil ooze with clay; carbonate nannofossil ooze; diatom nannofossil ooze; diatom nannofossil ooze with biosilica	Nannofossil ooze, often with homogeneous appearance; rare: foraminifers and other calcareous components; frequent: diagenetic overprinting.	0.2 to >100	Sparse to heavy	Light to dark gray, greenish gray, and brownish gray (with clay: brown; with carbonate: light-to-dark gray)	I: 96%	Hemipelagic/ contourite
Carbonate	2	Carbonate clay with nannofossils; clay with nannofossils and carbonate	Siliciclastic clay with varying abundance of nannofossils and carbonate grains.	0.3–3	Slight to heavy	Dark gray	I: 1%	Hemipelagic/ contourite
Clay	3	Clayey carbonate with nannofossils; nannofossil carbonate with clay	Recrystallized/inorganic carbonate grains of silt-to-clay size with varying abundance of nannofossils and clay.	0.3–1	Slight to heavy	Dark greenish gray; dark bluish gray	I: 3%	Hemipelagic/ contourite

and diatom nannofossil ooze with biosilica (Figure F8). Sediments are light to dark gray, greenish gray, and brownish gray, often with foraminifers disseminated throughout the sediment. Bioturbation ranges from absent to heavy. Trace fossils including *Chondrites*, *Ophiomorpha*, *Planolites*, *Thalassinoides*, and *Zoophycos* are commonly observed. Dark patches, nodules, and pyrite are observed throughout, although the occurrence of these features varies with depth.

3.2.1.1. Smear slides

Nannofossils are the dominant (>50%) component in the Lithofacies 1. Siliciclastic components range in abundance from trace (≤1%) to abundant (>25%–50%), and carbonate ranges from rare (>1%–10%) to abundant (>25%–50%). Foraminifers and authigenic minerals (pyrite, dolomite, glauconite, and iron oxides) are present in most of the samples and range from trace (≤1%) to rare (>1%–10%). Diatoms are present in one smear slide at a trace level (≤1%), in one as rare (>1%–10%), and in two as abundant (>10%–25%) (Samples 397-U1588A-20X-CC, 60 cm, and 21X-4, 65 cm). Sponge spicules and other siliceous biogenic components such as radiolarians range from trace (≤1%) to rare (>1%–10%). For all (biogenic and siliciclastic) components taken together, 50%–90% of grains are in the clay-size fraction, 5%–40% are in the silt-size fraction, and 1%–15% are in the sand-size fraction.

3.2.2. Lithofacies 2

Lithofacies 2 consists of sediments that are principally clay comprising a range of siliciclastics with varying amounts of nannofossils and carbonate. Lithologies include carbonate clay with nannofos-

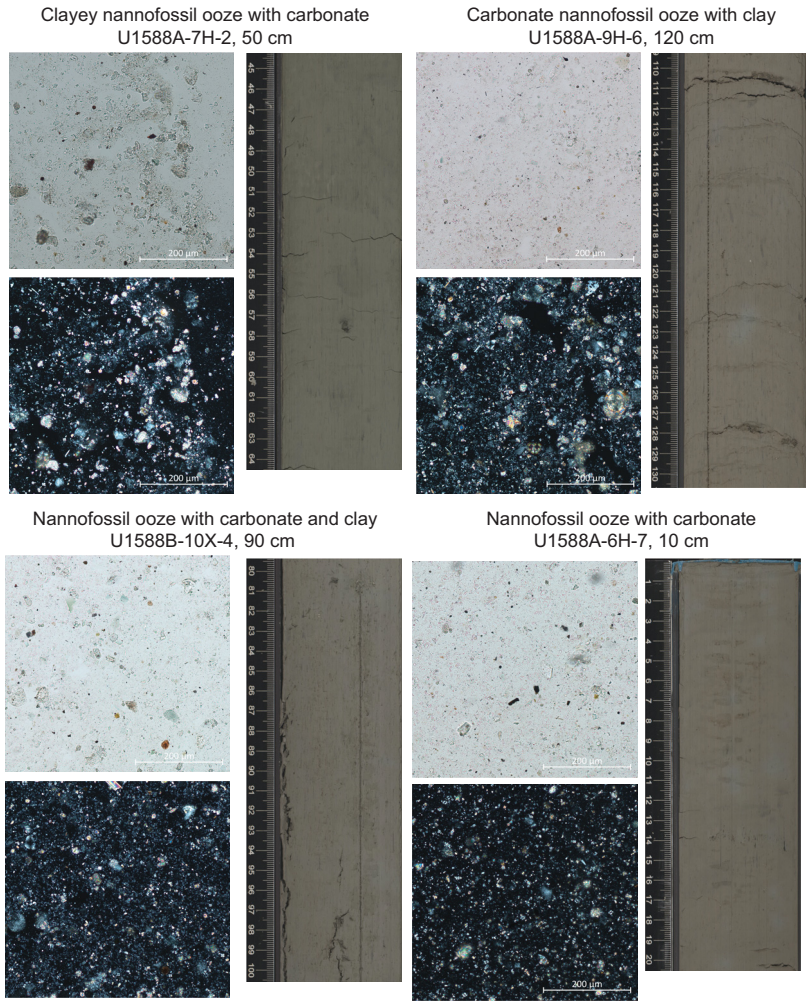

Figure F8. Lithofacies 1, Site U1588. All images: upper left = transmitted light brightfield, lower left = cross-polarized light (XPL), right = section half images, which include the interval where smear slides were taken.

sils, and clay with nannofossil and carbonate. Sediments are predominantly dark gray. Lithofacies 2 includes the same sedimentary structures, bioturbation, trace fossils, and diagenetic features described in Lithofacies 1.

3.2.2.1. Smear slides

Siliciclastic grains are the dominant (>50%) component in Lithofacies 2 and are present in two smear slides in Samples 397-U1588A-19X-2, 40 cm, and 21X-2, 48 cm. Carbonate abundance is common (>10%–25%) to abundant (>25%–50%). Nannofossils are common (>10%–25%). Foraminifers are trace (≤1%) to rare (>1%–10%). Authigenic minerals are rare (>1%–10%). For all (biogenic and siliciclastic) components, 70%–85% of grains are in the clay-size fraction, 15%–30% are in the silt-size fraction, and 1%–2% are in the sand-size fraction.

3.2.3. Lithofacies 3

Lithofacies 3 consists of sediments that are principally carbonate grains with varying amounts of siliciclastics and nannofossils. Lithologies include clayey carbonate with nannofossils and, in one instance, nannofossil carbonate with clay. Sediments are predominantly dark greenish or bluish gray. Lithofacies 3 includes the same sedimentary structures, bioturbation, trace fossils, and diagenetic features described in Lithofacies 1.

3.2.3.1. Smear slides

Carbonate grains are the dominant (>50%) component in Lithofacies 3 and are present in five smear slides in Samples 397-U1588A-6H-7, 10 cm; 9H-3, 120 cm; 23X-4, 60 cm; 24X-3, 38 cm; and 25X-4, 100 cm. Siliciclastics are abundant (>25%–50%), and nannofossils are common (>10%–25%). Foraminifers and sponge spicules are rare (>1%–10%). Authigenic minerals and diatoms occur in trace abundance (≤1%). For all (biogenic and siliciclastic) components, 50%–80% of grains are in the clay-size fraction, 20%–45% are in the silt-size fraction, and 1%–5% are in the sand-size fraction.

3.3. Lithostratigraphic Unit I

Intervals: 397-U1588A-1H through 49X; 397-U1588B-1H through 64X; 397-U1588C-2X through 54X; 397-U1588D-1H through 76X
Depths: Hole U1588A = 0–353 m CSF-B; Hole U1588B = 0–352.8 m CSF-B; Hole U1588C = 92–354.8 m CSF-B; Hole U1588D = 0–412.5 m CSF-B
Thickness: Hole U1588A = 353 m; Hole U1588B = 352.8 m; Hole U1588C = 262.8 m; Hole U1588D = 412.5 m
Age: Quaternary to Pleistocene (~0–2.2 Ma)
Primary lithofacies: 1

The sedimentary sequence at Site U1588 is contained within a single lithostratigraphic unit (Table **T2**). Unit I encompasses sediments from 0 to 350 m CSF-B in Holes U1588A–U1588C and to 412.5 m CSF-B in Hole U1588D and consists primarily of Lithofacies 1 (>95% of sediment depths), with minor occurrences of Lithofacies 2 (~1% of sediment depths) and Lithofacies 3 (~3% of sediment depths). Contacts between lithologies are color boundaries or bioturbated, straight to irregular, and gradational to sharp. Foraminifers are common throughout, and subtle color bands occur irregularly. Variations in sediment composition between and within the lithofacies (i.e., between intervals of light and dark sediments) generally occur at the decimeter to meter scale.

Sediments from ~0–75 m CSF-B (Cores 397-U1588A-1H through 8H, 397-U1588B-1H through 8H, and 397-U1588D-1H through 8H) consist mostly of clayey nannofossil ooze with carbonate, are dark gray, and do not display a clear cyclicity in color or lithology. Sediments from ~75–160 m CSF-B (Cores 397-U1588A-9H through 18X, 397-U1588B-9H through 25X, 397-U1588C-2X through 21X, and 397-U1588D-9H through 29X) consist of light gray layers of nannofossil ooze with carbonate (major) and gray or brown carbonate nannofossil ooze with clay (minor). Sediments from ~160–412 m CSF-B (Cores 397-U1588A-19X through 49X, 397-U1588B-26X through 64X, 397-U1588C-22X through 54X, and 397-U1588D-30X through 76X) consist mostly of nannofossil ooze with carbonate and clay, and other lithologies such as clayey carbonate with nannofossil and clayey nannofossil ooze with carbonate constitute a very small fraction. Sediments

throughout this interval are light-to-dark gray and do not display any clear cyclicity in color or lithology.

3.3.1. Biosilica

Smear slides observations reveal the rare-to-abundant occurrence of siliceous organisms, including diatoms, radiolarians, sponge spicules, and silicoflagellates (Figure F9). Intervals with abundant siliceous microfossils were observed in Sections 397-U1588A-20X-CC, 60 cm, and 397-U1588C-20X-2, 6 cm. In these intervals, the diatom nannofossil ooze and the diatom nannofossil ooze with carbonate and clay has an olive-green color and a coarser texture, with the occurrence of the diatom genus *Coscinodiscus* as abundant. Other genera forms observed in these intervals are *Actinoptychus senarius* and *Triceratium*. In Section 397-U1588C-20X-2, 100 cm, the nannofossil ooze with carbonate, clay, and biosilica has a dark olive-green color and a fine texture, with common occurrence of diatoms (Figure F9). In these intervals, forms of the genera *Rhizosolenia*, *Stephanopyxis*, *Thalassiosira*, and *Chaetoceros*, as well as *Chaetoceros* resting spores, are observed.

3.3.2. Diagenetic features

A layer of dark orange-brown sediment is present from approximately 0 to 100 cm CSF-B in Sections 397-U1588A-1H-1, 397-U1588C-1H-1, and 397-U1588D-1H-1. Small dark patches (centimeter scale), which often outline trace fossils and burrows, are found throughout sediments at Site U1588. Pyrite nodules and pyritized burrows are also found throughout Site U1588 (Figure F10), except in the uppermost few tens of meters of Cores 397-U1588A-1H through 5H (0–40.23 m CSF-B), 397-U1588B-1H through 3H (0–30.0 m CSF-B), and 397-U1588D-1H through 3H (0–15.0 m CSF-B), in which only dark patches occur. An extraordinarily large pyritized burrow is seen in Sections 397-U1588C-37X-3 and 37X-4 (Figure F10).

3.3.3. Bioturbation, trace fossils, and macrofossils

Bioturbation varies from sparse to heavy throughout. The majority of core in all holes shows slight to moderate bioturbation. At the tops of sections particularly in APC cores (397-U1588A-1H through 17H, 397-U1588B-1H through 9H, and 392-U1588C-1H through 11H) and shallow XCB cores containing soft sediment (e.g., Cores 397-U1588A-18X and 19X), burrow features are less clear and classification is uncertain. Trace fossils of *Chondrites*, *Planolites*, *Zoophycos*, and *Thalassinoides/Ophiomorpha* are common and generally become more distinctive downhole. Minor *Terebellina* and *Diplocraterion* are recognized. Trace fossil burrows range from millimeter

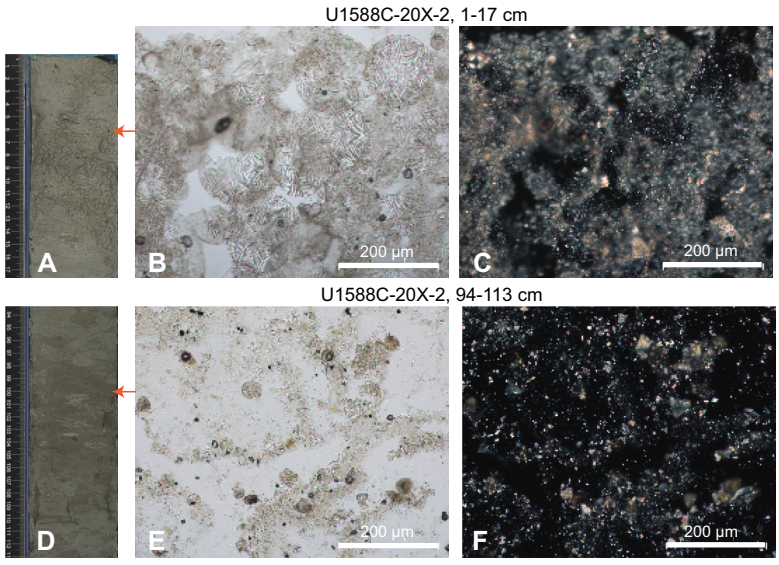

Figure F9. Nannofossil ooze with diatoms and clay, Hole U1588C. Left: section half images of (A) 1–17 cm and (D) 94–113 cm. Center: transmitted light brightfield image of smear slides of (B) 6 cm and (E) 100 cm, showing nannofossil ooze with diatoms and clay. Right: XPL image of smear slides of (C) 6 cm and (F) 100 cm.

Figure F10. 40 cm pyritized burrow, Hole U1588C. The burrow was broken during XCB drilling. Note the distinct biscuiting.

to, in rare cases, decimeter scale and often exhibit diagenetic features such as pyritization or dark outlining. Shells and shell fragments are present in many cores at Site U1588. A whole *Turritella* shell is found in interval 397-U1588A-3H-3, 36–37 cm. A deep-sea coral is seen in interval 397-U1588B-3H-1, 33–37 cm, hosted in sediments from Marine Isotope Stage (MIS) 4. The deep-sea coral is unlikely to be in situ, but the exact speciation is yet to be identified (Figure **F11**).

3.4. Complementary analyses

3.4.1. Drilling and other disturbance

Drilling disturbance is found throughout Site U1588 and varies with coring type, depth in hole, and sea state. Gas expansion is widespread throughout both APC and XCB cores at this site. Biscuiting is present in most XCB cores, with severity ranging from slight to moderate. Biscuiting is more easily observed in more consolidated sediments (XCB cores split by saw), rather than in soft sediments (split by wire). Fall-in is present throughout both APC and XCB cores, particularly in the uppermost sections of cores. In the first sections of APC cores, disturbed bedding and soupy and slurry intervals, ranging from slight to strong in severity, are often seen. Drilling and other forms of disturbance for all cores are described in Tables **T3**, **T4**, **T5**, and **T6**. Slightly disturbed strata have been omitted. Representative images of drilling disturbance types are shown in Figure **F12**.

3.4.2. X-ray diffraction mineralogy

The major minerals in XRD samples from Hole U1588A are calcite, quartz, feldspars, mica (mainly muscovite), and various clay minerals such as illite, kaolinite, smectite, and chlorite. Minor minerals include birnessite, pyrite, dolomite, siderite, titanite, magnetite, and ankerite. The major mineral assemblage indicated using XRD analyses is similar to that observed in smear slides.

Figure F11. Deep-sea coral, Hole U1588B.

Table T3. Drilling disturbance, Hole U1588A. **Download table in CSV format.**

Table T4. Drilling disturbance, Hole U1588B. **Download table in CSV format.**

Table T5. Drilling disturbance, Hole U1588C. **Download table in CSV format.**

Table T6. Drilling disturbance, Hole U1588D. **Download table in CSV format.**

The feldspars are mainly composed of Ca-bearing albite to Na-bearing anorthite. Some Rb-rich silicates are often observed, particularly in sediments taken from Sections 397-U1588A-1H-2, 5H-6, 6H-6, 10H-2, 14H-3, 19X-2, 22X-6, 23X-4, 24X-3, 38X-2, 42X-2, 43X-6, 47X-3, and 49X-3. Birnessite (Mn oxide hydrate, i.e., MnOOH) is seen throughout the hole. Mn-related mineral siderite ($MnCO_3$) is seen in Sections 23X-4 and 43X-6. Mg-bearing calcite and/or dolomite are present in sediments from Sections 1H-2, 2H-3, 5H-6, 10H-2, 13H-6, 16H-2, 18X-3, and 49X-3. Ankerite is seen in samples from Sections 4H-6, 10H-2, and 24X-3; aragonite is seen in Section 40X-1; and minor phases of titanite and rutile/anatase are seen in Sections 1H-2, 9H-6, and 44X-3. Pyrite is abundant in samples from Sections 7H-2, 20X-4, 21X-4, 40X-1, 44X-3, and 46X-2, and magnetite and/or other Fe oxides minerals are seen in Sections 24X-3 and 36X-3. Finally, Zn-related minerals (e.g., Zn oxides) are seen in samples from Sections 20X-4 and 26X-2, and Zn-bearing chlorite is seen in Sections 5H-6, 12H-1, 14H-3, 15H-2, 17H-7, 26X-2, 30X-2, 32X-3, 38X-2, and 46X-2, which is confirmed by bulk sediment inductively coupled plasma spectrometry data showing Zn enrichment in some samples (see **Geochemistry**).

3.4.3. Carbonate content

$CaCO_3$ varies from ~20 to ~50 wt% and shows little long-term trend downhole in Hole U1588A (Figure **F13**; see **Geochemistry**). The highest $CaCO_3$ values are seen at ~70 m CSF-B, corresponding to MIS 9. Sediment $CaCO_3$ appears to vary more strongly at ~60–220 m CSF-B than at shallower and deeper depths, which is also reflected in lithologies. Shallower than ~60 m CSF-B, sediments are dominantly clayey nannofossil ooze with carbonate. Deeper than ~220 m CSF-B, sediments are almost entirely nannofossil ooze with carbonate and clay. In contrast, in sediments from ~60 to 220 m CSF-B, lithologies are more variable and include nannofossil ooze with carbonate, carbonate nannofossil ooze with clay, nannofossil ooze with carbonate and clay, and clayey nannofossil ooze with carbonate. Over the entire length of sediments drilled, the correlation between $CaCO_3$ and L* is less clear than those seen at deeper sites from Expedition 397, which may be related to the location of Site U1588. Located closer to the continent at a shallower water depth, Site U1588 sediments may be composed of various types of terrigenous inputs (e.g., clay

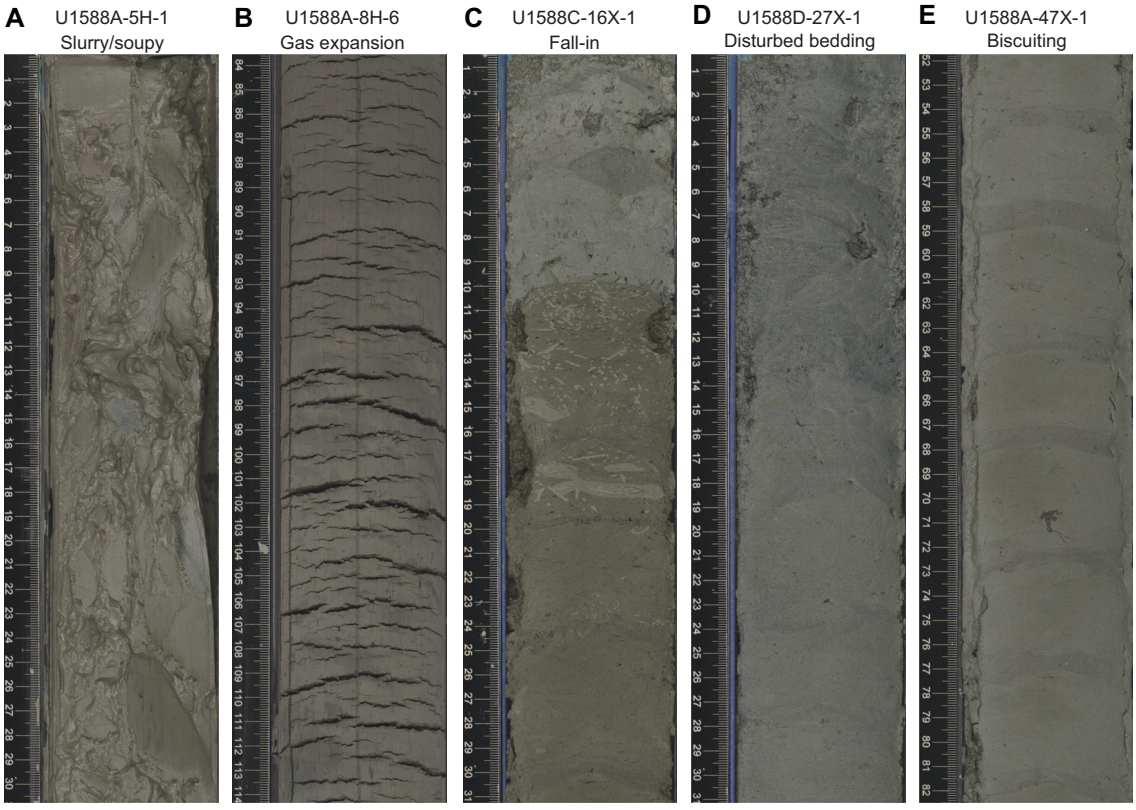

Figure F12. Drilling disturbance examples, Site U1588. A. Slurry. B. Gas expansion. C. Fall-in. D. Disturbed bedding. E. Biscuiting.

minerals and carbonates) with different color brightness, which weakens the L* to $CaCO_3$ correlation.

3.4.4. Integrating physical properties measurements with lithofacies observations

Variations in and between lithologies observed at Site U1588 were compared to downcore physical properties measurements, including NGR intensity, moisture and density (MAD) porosity and density, gamma ray attenuation (GRA) bulk density, MS from both loop (Whole-Round Multisensor Logger [WRMSL) and point (Section Half Multisensor Logger [SHMSL]) detectors, color variations (RGB) and color reflectance L*a*b* (see **Physical properties**).

Changes in physical properties are associated with variations in the siliciclastic clay content of the nannofossil ooze that is predominant throughout sediments recovered in all holes at Site U1588 (Figure **F13**). Each characteristic displays persistent decimeter- to meter-scale cycles that generally diminish in amplitude downhole. Greater clay content in the nannofossil ooze is associated with a decrease in RGB values, increase in MS and NGR, and decrease in L*. The color reflectance L* (increase) and a*, b*, and MS (decrease) all display marked shifts in the uppermost 50–60 m and then continue to vary cyclically about respective mean values that display little change from 50–412.5 m CSF-B. Calcium carbonate content similarly varies around a mean that remains approximately constant throughout each hole at Site U1588.

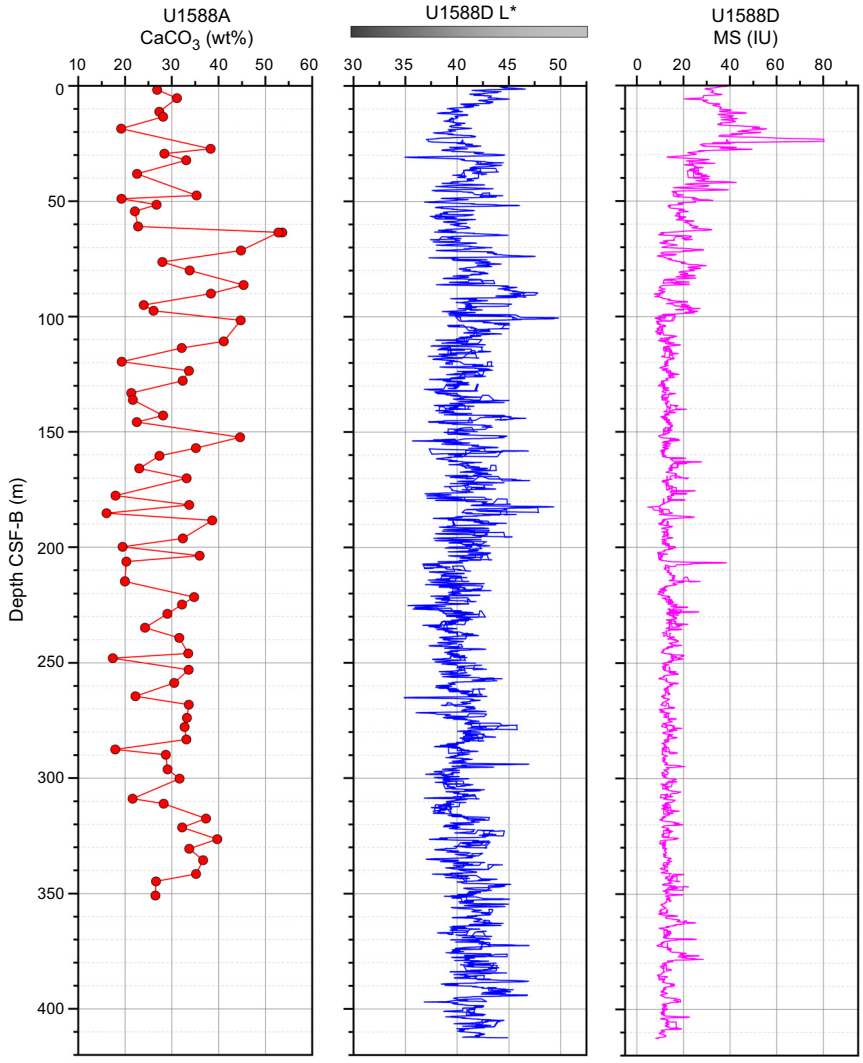

Figure F13. $CaCO_3$, L*, and MS, Site U1588.

3.5. Discussion

3.5.1. Lithology

The abundance of Lithofacies 1 indicates the dominance of hemipelagic sedimentation at Site U1588 throughout the last 2 My of the Pleistocene (Holes U1588A–U1588D) (Figure **F14**). Siliciclastic input was likely relatively high or carbonate input (or preservation rates) was relatively low during the last 250 ky at Site U1588, as indicated by the higher values of clay content, L*, and MS in the upper 50 m CSF-B (Holes U1588A, U1588B, and U1588D). Siliciclastic input and carbonate input (or preservation) appear to have varied in similar fashion throughout the preceding portion of the Pleistocene, as indicated by the relatively constant mean values of nannofossils, clay, and lightness of sediments from 50 to 412.5 m CSF-B (Holes U1588A–U1588D). Recurring variations of layers of nannofossil ooze with differing clay abundances may suggest a link between sediment composition and orbital cyclicity, which is also consistent with previous findings from Sites U1586, U1587, and U1385, as well as with variations in physical properties (see **Stratigraphic correlation**).

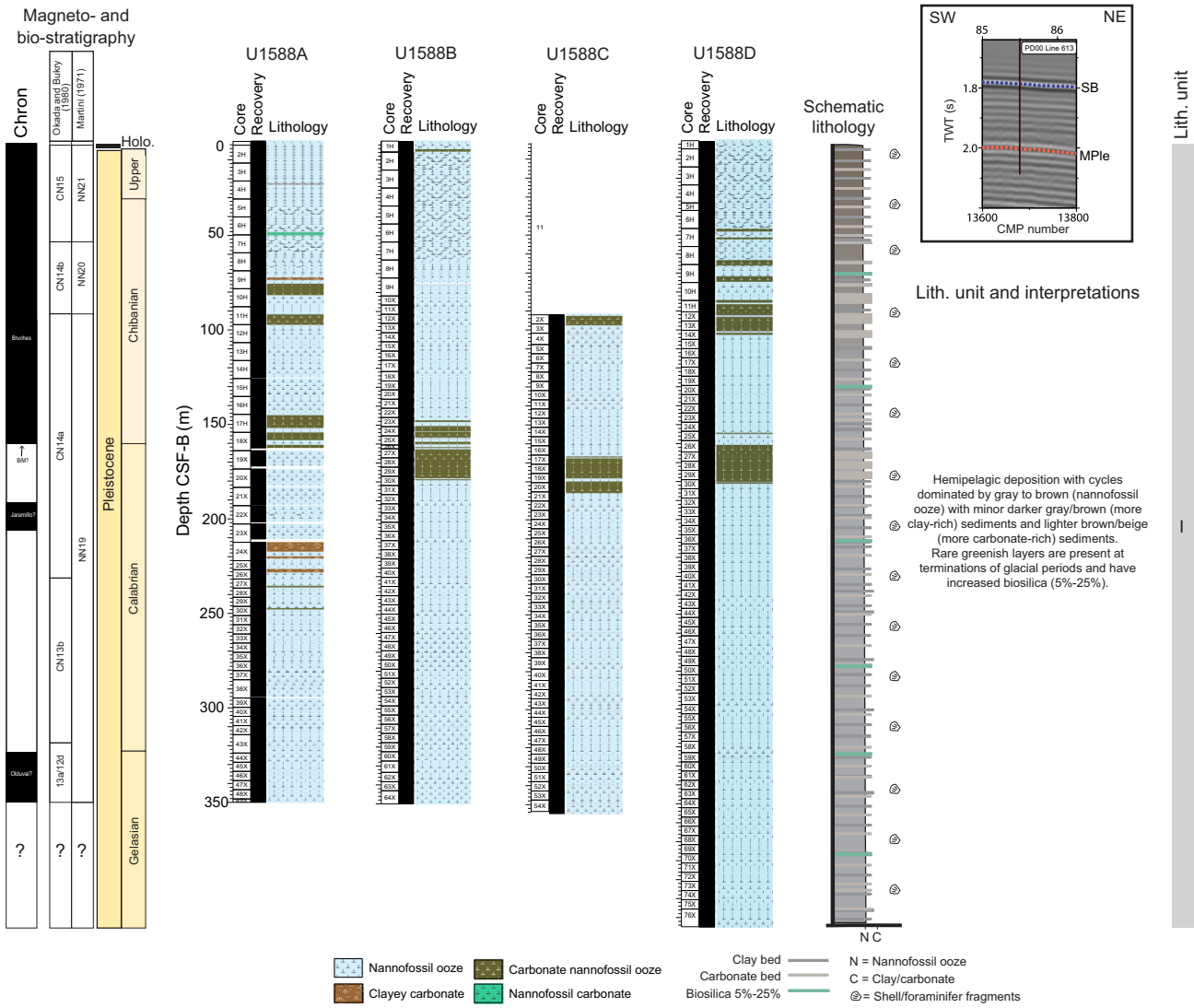

Figure F14. Lithologic summary, Site U1588. ? = uncertainty. Colors are based on visual description and L*a*b* values (see Physical properties). Color is independent of lithology and is related to relative amounts of minor constituents such as pyrite and glauconite. Nannofossil biozones and paleomagnetic boundaries are summarized from shipboard data and may disagree. Inset: cropped section of Seismic Line PD00 Line 613 showing location along transect and depth of Holes U1588A–U1588D. SB = seabed, MPle = middle Pleistocene, TWT = two-way traveltime, CMP = common midpoint.

The opal-bearing layers identifiable from sediment color are recognized on color reflectance and magnetic data in Sections 397-U1588A-20X-CC and 397-U1588C-20X-2. These were potentially deposited during MIS 26 to MIS 25 (Termination XII) and MIS 25, respectively (for age model, see **Biostratigraphy**). Past studies suggested increased productivity in the Iberian margin and Northwest Africa region during glacial–interglacial transitions (Abrantes, 1991a, 1991b, 2000). Peaks in diatom abundance have been documented in other terminations, such as MIS 10/9 (Termination IV), 6/5 (Termination II) (Thomson et al., 2000), and MIS 26/25 (Termination XII) (Ventura et al., 2017; Abrantes et al., 2017). A possible explanation for increased primary production is enhanced coastal upwelling at these glacial terminations, as evidenced by the presence of *Chaetoceros* spores. The stronger upwelling may reflect the enhancement of the Canary Current Upwelling System and a more nutrient-rich source water during some deglaciations. Alternatively, nutrients could be introduced to the site region through flooding of continental shelves related to rising sea level during deglaciation (Abrantes, 2000; Thomson et al., 2000). However, an increase in diatom preservation due to the presence of more Si-rich bottom waters cannot be excluded (Abrantes et al., 2017).

3.5.2. Diagenetic features

The orange brownish sediments in the uppermost meter or two of the first core in Holes U1588A, U1588B, and U1588D is likely a result of downward penetration of oxygen into the sediment column from the overlying seawater. The oxygen in these sediments would eventually be depleted by organic respiration. The gray sediments below this upper horizon are inferred to be reducing, leading to the mobilization of redox-sensitive elements including iron and manganese. These mobilized elements diffuse upward and precipitate out at the boundary with the oxic layer above, forming a redox horizon that migrates upward or downward relative to the seafloor as ocean ventilation and organic carbon export vary through time. This transition is gradual rather than sharp at Site U1588, possibly related to the sufficiently rapid accumulation of sediments to prevent a distinct boundary to be maintained through time at any subseafloor depth.

Pyrite (FeS_2) is a common feature at Site U1588. Pyrite occurs as discrete elongated burrow fills and as isolated nodules, evident along the face of nearly every split core below ~40 m CSF-B. The presence of pyrite suggests relatively reducing conditions in sediment pore waters. Such conditions may result from increased oxygen consumption driven by enhanced surface-ocean organic carbon export and subsequent respiration at depth and in pore waters. Abundant discrete occurrences of pyrite suggest the presence of local microenvironments, typically associated with benthic organisms. The absence of pyrite in the shallowest few cores in Holes U1588A, U1588B, and U1588D may be related to generally greater influence of oxygen in these pore waters, although the abundance of amorphous iron monosulfide patches suggests that the transition to pyrite downcore may be more related to kinetic influences on pyrite formation.

3.5.3. Drilling and other disturbance

Gas expansion is one of the most widespread drilling disturbances at Site U1588 in both APC and XCB cores. Drilling disturbance is influenced by operation conditions (weather) and thus may not show any consistency between holes. Bioturbation is present in almost all sediments from Site U1588, and its intensity generally increases or becomes more distinct downhole. Trace fossil assemblages are typical of marginal marine environments (Heard et al., 2014).

4. Biostratigraphy

At Site U1588, the ~415 m thick cored sedimentary succession ranges in age from the Holocene to early Pleistocene (Cores 397-U1588A-1H through 397-U1588D-76X). Split core and core catcher samples accounted for 21 calcareous nannofossil and 1 benthic and 5 planktonic foraminifer bioevents. Nannofossils are very abundant to common, well preserved, and generally well distributed throughout the succession. Planktonic foraminifers also are abundant and well preserved.

The zonal schemes of calcareous nannofossils and planktonic foraminifers generally agree. Integrated calcareous microfossil bioevents are provided in Figure **F15**, with nannofossil and planktonic foraminifer datums reported in Tables **T7**, **T8**, and **T9**.

4.1. Calcareous nannofossils

Calcareous nannofossil biostratigraphy at Site U1588 is based on 49 core catchers and more than 150 split core samples taken from Hole U1588A. All the samples were processed into smear slides using the standard techniques.

The nannofossil assemblage in Hole U1588A is defined by 21 groups/taxa-morphotypes, including *Emiliania huxleyi*, *Gephyrocapsa caribbeanica* gr., *Gephyrocapsa* spp. (small < 4 µm, medium, and large > 5.5 µm), *Gephyrocapsa omega*, *Pseudoemiliania lacunosa*, *Reticulofenestra* (<3, 3–5, 5–7, and >7 µm), *Reticulofenestra asanoi*, *Coccolithus pelagicus*, *Calcidiscus leptoporus*, *Calcidiscus macintyrei*, *Helicosphaera inversa*, *Helicosphaera sellii*, *Syracosphaera* spp., *Scyphosphaera*

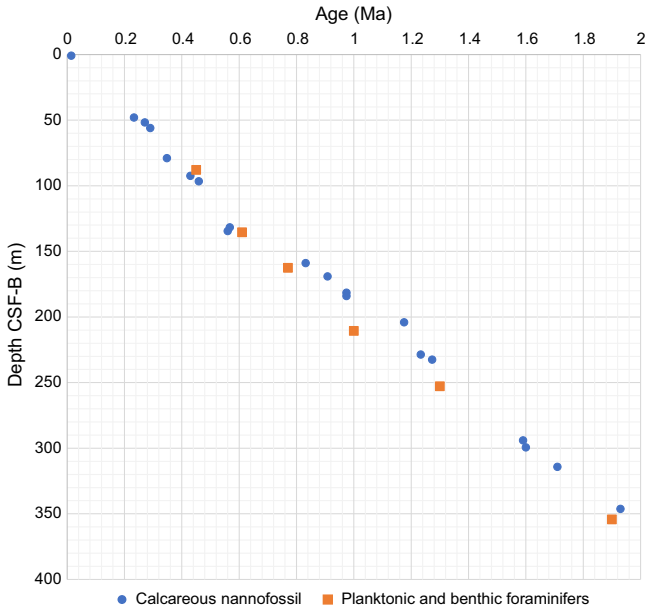

Figure F15. Preliminary age model based on calcareous nannofossils and planktonic foraminifer events.

Table T7. Calcareous nannofossil bioevents, Hole U1588A. **Download table in CSV format.**

Top core, section, interval (cm)	Top depth CSF-B (m)	Top depth CSF-A (m)	Bottom core, section, interval (cm)	Bottom depth CSF-B (m)	Bottom depth CSF-A (m)	Mean depth CSF-B (m)	Age (Ma)	MIS	Datum	Source	Okada and Bukry (1980)	Martini (1971)
397-U1588A-			397-U1588A-									
1H-1, 80	0.80	0.80	1H-1, 80	0.80	0.80	0.800	0.0142	1	HCO >4 µm *Emiliania huxleyi* large	Balestra et al. (2015)	CN15	NN21
6H-6, 71	48.03	48.41	6H-7, 33	49.11	49.59	48.571	0.233	7	CO *Gephyrocapsa caribbeanica, Emiliania huxleyi*	Balestra et al. (2015)	CN15	NN21
7H-3, 71	51.75	51.92	7H-4, 75	53.09	53.60	52.420	0.2708	7–9	*HCO Gephyrocapsa caribbeanica*	Balestra et al. (2015)	CN14b/CN15	NN20/NN21
7H-5, 75	55.92	56.42	7H-6, 75	57.32	57.94	56.619	0.290	8	*LO E. huxleyi*	Balestra et al. (2015)	CN14b	NN20
10H-1, 75	78.93	78.95	10H-2, 75	80.32	80.37	79.627	0.348	11	HO *Helicosphaera inversa*	Balestra et al. (2015)	CN14b	NN20
11H-4, 75	92.38	92.47	11H-5, 75	93.68	93.80	93.028	0.430	12	HO *Pseudoemiliania lacunosa*	Balestra et al. (2015)	CN14b/CN14a	NN19/NN20
11H-7, 75	96.49	96.67	12H-1, 75	97.91	97.95	97.203	0.459	12	LO *Helicosphaera inversa*	Balestra et al. (2015)	CN14a	NN19
14H-7, 60	134.49	134.69	15H-1, 75	126.43	126.45	130.460	0.560	14	HO *Gephyrocapsa omega*	Balestra et al. (2015)	CN14a	NN19
15H-5, 75	131.69	131.83	15H-6, 75	133.16	133.30	132.425	0.567	14	LCO *Gephyrocapsa caribbeanica*	Balestra et al. (2015)	CN14a	NN19
18X-4, 72	158.97	158.97	18X-5, 72	160.14	160.14	159.555	0.832	20	T absence *Gephyrocapsa omega*	Balestra et al. (2015)	CN14a	NN19
19X-4, 64	169.03	169.03	19X-5, 75	170.64	170.64	169.835	0.908	23	HCO *Reticulofenestra asanoi*	Balestra et al. (2015)	CN14a	NN19
20X-7, 57	181.52	181.50	21X-1, 72	184.02	184.02	182.77	0.974	23	LO *Gephyrocapsa omega*	Balestra et al. (2015)	CN14a	NN20
21X-1, 72	184.02	184.00	21X-2, 72	185.48	185.48	184.75	0.974	26	RE *Gephyrocapsa* medium	Balestra et al. (2015)	CN14a	NN19
23X-2, 6	204.05	204.05	23X-3, 60	205.02	205.20	204.535	1.175	35	LCO *Reticulofenestra asanoi*	Balestra et al. (2015)	CN14a	NN19
26X-2, 76	228.65	229.12	26X-3, 75	229.79	230.57	229.217	1.233	37	HO *Gephyrocapsa* large	Balestra et al. (2015)	CN13b	NN19
27X-1, 75	232.41	232.55	27X-2, 75	233.60	234.01	233.006	1.273	38–41	HO *Helicosphaera sellii*	Balestra et al. (2015)	CN13b	NN19
38X-CC, 71	294.04	294.04	39X-1, 77	295.37	295.57	294.707	1.590	53–55	LO *Gephyrocapsa* large	Gradstein et al. (2020)	CN13b	NN19
39X-5, 29	299.40	300.99	40X-1, 71	300.40	300.41	299.903	1.600	55–58	HO *Calcidiscus macintyrei*	Gradstein et al. (2020)	CN13b	NN19
42X-CC, 19	314.13	314.36	43X-1, 70	314.90	314.90	314.517	1.710	59–61	LO *Gephyrocapsa* medium	Gradstein et al. (2020)	CN13a/CN13b	NN19
48X-3, 75	346.25	347.01	48X-4, 75	347.46	348.51	346.853	1.930	73–78	HO *Discoaster brouweri*	Gradstein et al. (2020)	CN13a/CN12d	NN18/NN19

spp., *Discoaster* spp., *Discoaster brouweri*, and occasionally less abundant taxa (see Plate **P1** in the Site U1586 chapter [Abrantes et al., 2024b]).

A total of 21 calcareous nannofossil events were identified within the studied section. These events were dated using age calibrations by Balestra et al. (2015), Raffi et al. (2006), and Gradstein et al. (2020) (Table **T7**). Additionally, the standard biozones of Martini (1971) and Okada and Bukry (1980) were identified. For these attributions, only taxa or morphotypes with biostratigraphic significance were considered (Table **T8**).

4.1.1. Pleistocene

Nannofossils are very abundant and show good preservation throughout the Pleistocene interval (19–348 m core depth below seafloor, Method A [CSF-A]; 397-U1588A-3H-6, 76 cm, to 48X-4, 75 cm). There is significant reworking throughout the section, and Cretaceous to Pleistocene nannofossils are identified.

Zone CN15/NN21 is based on the highest common occurrence (HcO) of large *E. huxleyi* (>4 µm) found in Sample 397-U1588A-1H-1, 80 cm. Zone CN14b/NN20-21 is identified based on the HcO, lowest occurrence (LO), and highest occurrence (HO) of *G. caribbeanica*, *E. huxleyi*, and *H. inversa* found in Samples 7H-4, 75 cm, 7H-6, 75 cm, and 10H-2, 75 cm, respectively. Zone CN14b-14a/NN19-20 is based on the HO of *P. lacunosa* above Sample 11H-5, 75 cm. Zone CN14a/NN19 is defined by the presence of several nannofossil markers including the LO of *H. inversa* in Sample 12H-1, 75 cm, the HO of *G. omega* in Sample 15H-1, 75 cm, the lowest common occurrence (LcO) of *G. caribbeanica* in Sample 15H-6, 75 cm, the temporary absence of *G. omega* in Sample 18X-5, 72 cm, the HcO of *R. asanoi* in Sample 19X-5, 75 cm, and the LcO of *R. asanoi* in Sample 23X-3, 60 cm.

Zone CN13b/NN19 is based on the HO and LO of large *Gephyrocapsa* (>5.5 µm) and the HO of *C. macintyrei* above Samples 397-U1588A-39X-1, 77 cm, and 40X-1, 71 cm, respectively. Zone CN13a-12d/NN18 is based on the HO of *D. brouweri* above Sample 48X-4, 75 cm. The same calcareous nannofossil assemblage is observed in Samples 397-U1588C-52X-CC, 11–17 cm, 53X-CC, 13–19 cm, and 54X-CC, 11–17 cm; however, the scarcity of *D. brouweri* and the high abundance of reworked specimens determines that this HO should be cautiously considered (Table **T8**).

4.1.2. Planktonic foraminifers

Planktonic foraminifer biostratigraphy is based on 49 core catchers from Hole U1588A. The relative abundance of taxa and estimation of assemblage preservation is presented in Table **T10**. Planktonic foraminifers are abundant and well preserved in all the studied samples. Scanning electron microscope (SEM) images of the biostratigraphic species are shown in Plate **P2** in the Site U1586 chapter (Abrantes et al., 2024b).

Table T8. Planktonic and benthic foraminifer bioevents, Holes U1588A. Reference after species name indicates primary reference. **Download table in CSV format.**

Bioevents	Age (Ma)	Sample	Depth CSF-B (m)	Reference
LO *Globorotalia hirsuta*	0.45	397-U1588A-10H-CC-PAL	87.666	Wade et al. (2011)
HO *Globorotalia tosaensis*	0.61	397-U1588A-15H-CC-PAL	135.132	Wade et al. (2011)
HO *Stilostomella* spp.	0.77	397-U1588A-18X-CC-PAL	162.455	Hayward (2002); Kawagata et al. (2005)
LO *Globorotalia excelsa*	1.0	397-U1588A-23X-CC-PAL	210.555	Wade et al. (2011)
HO *Globigerinoides obliquus*	1.3	397-U1588A-30X-CC-PAL	251.173	Wade et al. (2011)

Table T9. Calcareous nannofossil abundance, Hole U1588A. **Download table in CSV format.**

Table T10. Preservation and estimated abundance of planktonic foraminifers, Hole U1588A. **Download table in CSV format.**

Five planktonic foraminifer bioevents are identified, and the key biostratigraphic species and associated ages defined by Wade et al. (2011) are presented in Table **T8**. The upper part of the section, to 87.66 m CSF-B (Sample 397-U1588A-10H-CC), is assigned to the late middle Pleistocene (0.45 Ma) as evidenced by the LO of *Globorotalia hirsuta*. The HO of *Globorotalia tosaensis* belongs to the middle Pleistocene (0.61 Ma) and is recorded in Sample 15H-CC (135.16 m CSF-B). The interval between Samples 15H-CC and 23X-CC (210.55 m CSF-B) is assigned an age of 1 Ma based on the LO of *Globorotalia excelsa*. Sample 30X-CC (251.17 m CSF-B) is assigned to the Calabrian Stage (1.3 Ma) based on the HO of *Globigerinoides obliquus*. The lowermost sample, 49X-CC (352.97 m CSF-B), is estimated to be younger than 1.92 Ma based on the presence of *Globorotalia truncatulinoides*.

The mudline samples from Holes U1588A and U1588D are dominated by well-preserved planktonic foraminifers. The assemblage is characterized by a typical temperate North Atlantic fauna, including *Globorotalia inflata*, *Neogloboquadrina pachyderma*, *Globigerina bulloides*, and the presence of *Globigerinoides ruber*, *G. truncatulinoides*, and *Orbulina universa* (Table **T10**).

The Pleistocene assemblages show rapid changes between species typical of North Atlantic waters (e.g., *G. inflata*, *N. pachyderma*, and *Turborotalita quinqueloba*) and species from temperate to subtropical waters (e.g., *Globorotalia scitula*, *G. ruber*, and *Trilobatus sacculifer plexus*) (Table **T10**). A high concentration of large diatoms dominates Sample 397-U1588A-20X-CC (182.575 m CSF-B). Sample 21X-CC (192.585 m CSF-B) records *N. pachyderma* (s) that can be linked to a cold event. A high-resolution study is required to document the changes in the surface condition.

4.2. Benthic foraminifers

Benthic foraminifers were examined in core catchers from Hole U1588A (49 samples) and the mudline from Holes U1588A and U1588D. The presence of benthic foraminifers in the >150 µm fraction is summarized in Table **T11**. Abundance is generally low compared to planktonic foraminifers. The assemblages are characterized by genera of *Bulimina*, *Cassidulina*, *Cibicidoides*, *Globobulimina*, *Melonis*, *Sphaeroidina*, and *Uvigerina* in varying proportions (see Plates **P3** and **P4** in the Site U1586 chapter [Abrantes et al., 2024b]). The benthic foraminifers are well preserved, and the "*Stilostomella* extinction" event (0.58–0.7 Ma) (Hayward, 2002; Kawagata et al., 2005) is placed in Sample 397-U1588A-19H-CC (162.455 CSF-B).

Mudline core top samples from Holes U1588A and U1588D were gently washed to preserve fragile agglutinated specimens with low fossilization potential. In Holes U1588A and U1588D, few benthic specimens are recorded. Some hyaline specimens are stained with rose bengal and dominate the benthic foraminifer mudline assemblage such as *Uvigerina*, *Oridorsalis*, *Melonis*, *Cibicidoides*, *Cassidulina*, and *Bulimina* species. A few tubulars, organically cemented agglutinated benthic foraminifers, are also found. The mudline samples also contain sponge spicules regularly found in the downcore samples from Hole U1588A. The presence of well-preserved pteropods in the mudline and the uppermost nine core catchers confirms the excellent calcareous preservation in the samples.

4.3. Ostracods

Ostracods were examined in the sand fraction of all 49 core catcher samples from Hole U1588A (Cores 1H–49X) and the mudline samples from Holes U1588A and U1588D. They are present (as many as 110 specimens) in most samples. Overall, ostracods are more abundant and diverse in the upper half of the sequence and their preservation is generally good. The predominant genera are *Krithe* (58%, five species, including *Krithe keyi*, a species that has been associated with MOW) (Laprida et al., 2002), *Cytherella* (11%, one species), *Argilloecia* (6%, three species), *Echinocythereis* (4%, one species), *Neonesidea* (4%, two species), *Henryhowella* (2%, one species), *Cytheropteron* (2%, three species), and *Buntonia* (2%, three species). The ostracod taxa are listed in Table **T12**.

Table T11. Benthic foraminifers in the >150 µm fraction, Hole U1588A. **Download table in CSV format.**

Table T12. Ostracod taxa, Hole U1588A. **Download table in CSV format.**

5. Paleomagnetism

Paleomagnetic investigations of sediments from Site U1588 focused on measuring the natural remanent magnetization (NRM) of archive-half sections from Holes U1588A–U1588D at 4 cm intervals. We measured all archive-half sections except Section 397-U1588A-24X-1 (which was heavily disturbed during coring) and sections from core catchers. NRM measurements were made before and after 20 mT alternating field (AF) demagnetization for sections from Hole U1588A and Sections 397-U1588B-1H-1 through 11X-2. Because of increased core flow, Sections 397-U1588B-11X-3 through 64X-7 and sections from Holes U1588C and U1588D were measured only after 20 mT demagnetization (Table **T13**). Cores 397-U1588A-1H through 17H, 397-U1588B-1H through 9H, and 397-U1588D-1H through 11H were oriented with the Icefield MI-5 (see **Paleomagnetism** in the Expedition 397 methods chapter [Abrantes et al., 2024a]). The APC core orientation data for all oriented cores are reported in Table **T14**.

We collected and measured the NRM of 35 cube samples from Hole U1588A. Squares in Figure **F16** mark the depths where cube samples were taken (about one cube sample per full core in Hole U1588A). A total of 22 demagnetization steps (with peak field up to 50 mT) were used for NRM measurements of the cube samples (Table **T13**).

We processed archive-half section data extracted from the shipboard Laboratory Information Management System (LIMS) database by removing all measurements collected from (1) void intervals caused by whole round core sampling (i.e., interstitial water [IW] and paleontology [PAL]

Table T13. Demagnetization steps and instrument used for NRM measurement, Site U1588. **Download table in CSV format.**

Hole	Section halves or cube samples	Demagnetization steps (mT)	Instrument
U1588A	All archive-half core sections measured	0, 20	SRM
	All cube samples	0, 2, 4, 6, 8, 10, 12, 15, 18, 20, 22, 25, 28, 30, 32, 35, 38, 40, 42, 45, 48, 50	SRM
U1588B	Sections 1H-1A to 11X-2A	0, 20	SRM
	Sections 11X-3A to 64X-7A	20	SRM
U1588C	All archive-half core sections measured	20	SRM
U1588D	All archive-half core sections measured	20	SRM

Table T14. Icefield MI-5 data for APC cores, Site U1588. **Download table in CSV format.**

Core	Orientation angle (°)	Orientation standard deviation (°)
397-U1588A-		
1H	63.90	1.42
2H	47.64	1.55
3H	71.97	2.81
4H	162.89	1.24
5H	8.70	1.56
6H	76.82	2.83
7H	258.91	1.64
8H	331.32	2.71
9H	333.21	3.92
10H	185.72	1.34
11H	212.54	2.83
12H	336.53	5.14
13H	99.16	2.24
14H	93.83	4.48
15H	168.11	1.55
16H	169.40	0.79
17H	323.89	1.77
397-U1588B-		
1H	202.26	1.05
2H	149.12	1.58
3H	307.55	0.90
4H	115.08	1.39
5H	338.82	1.05
6H	29.58	1.20
7H	153.81	3.11
8H	49.80	1.10
9H	142.05	2.06
397-U1588D-		
1H	90.58	1.95
2H	97.27	1.71
3H	218.44	2.39
4H	131.98	1.09
5H	147.79	1.50
6H	173.21	2.42
7H	147.10	1.92
8H	31.16	1.15
9H	286.44	3.27
10H	164.88	2.37
11H	144.36	0.72

samples), (2) disturbed core top intervals in APC cores summarized in Table **T15**, and (3) the top and bottom 8 cm of each section and an extra 8 cm for the void and disturbed core top intervals. Intervals that were severely/strongly disturbed during coring (see **Lithostratigraphy**) are indicated in Figures **F16**, **F17**, **F18**, and **F19**, and data from these intervals are typically not used for magnetostratigraphic interpretation. In addition, a significant number of NRM measurements of section-half and cube samples on the SRM were compromised due to flux jumps. We avoided using data from sections influenced by this measurement problem for interpretation and removed data from compromised demagnetization steps for NRM of cube samples.

Declination data from APC cores where Icefield MI-5 core orientation data are available were corrected for each core using the estimated orientation angles and the current declination value at the site according to the 2020 International Geomagnetic Reference Field (IGRF2020) (see **Paleomagnetism** in the Expedition 397 methods chapter [Abrantes et al., 2024a]). To analyze the NRM data of both the section-half and the discrete cube samples, we used a modified version of the UPmag software (Xuan and Channell, 2009). The processed NRM inclination, declination (including orientation-corrected declination where available), and intensity data after 20 mT AF demagnetization are shown in Figures **F16**, **F17**, **F18**, and **F19**. The processed NRM data of the cube samples are shown in Figure **F20**. Because of the high gas expansion in the cores (see **Lithostratigraphy**), we used the CSF-B depth scale for figures and tables in this chapter to avoid significant overlap in the CSF-A depth scale between adjacent cores.

5.1. Natural remanent magnetization intensity and magnetic susceptibility

Intensities of NRM after 20 mT AF demagnetization (NRM_{20mT}) for cores from Holes U1588A–U1588D are similar in magnitude for overlapping depth intervals (Figures **F16**, **F17**, **F18**, **F19**). NRM_{20mT} intensity is on the order of 10^{-2} A/m for the upper ~50 m and decreases downhole to the order of 10^{-4} to 10^{-2} A/m between ~50 and 150 m CSF-B. Below ~150 m CSF-B, NRM_{20mT} intensity is mostly on the order of 10^{-5} to 10^{-3} A/m.

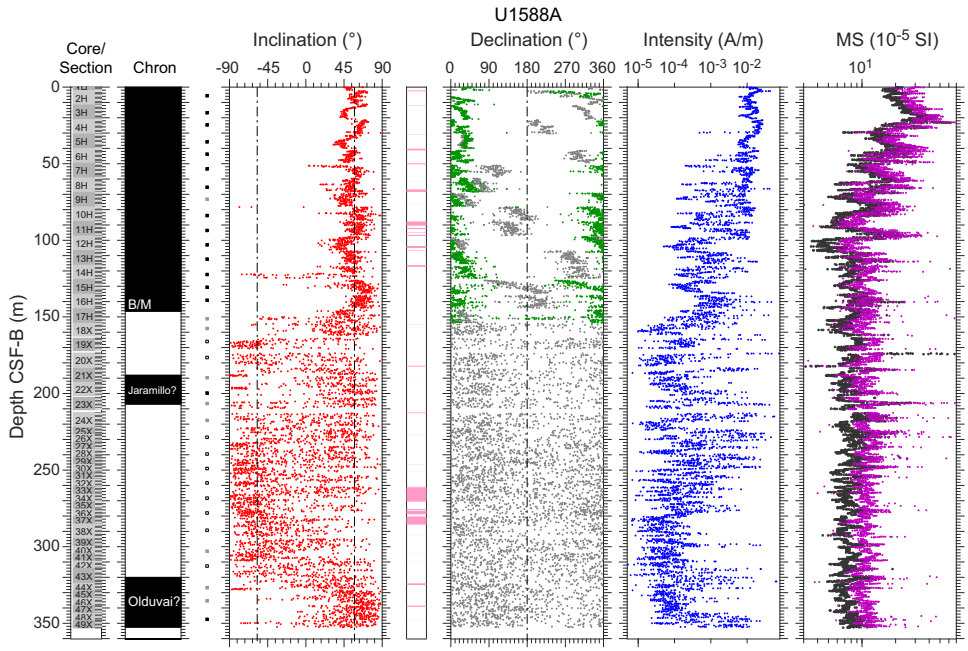

Figure F16. Paleomagnetism data after 20 mT AF demagnetization, Hole U1588A. Chron: black = normal polarity zone/boundary, white = reversed polarity zone/boundary, gray = uncertain polarity zone/boundary. Squares = depths where discrete cube samples were collected. Inclination: dashed lines = expected GAD inclinations at the site latitude during reversed and normal polarities. Pink shading = strongly disturbed intervals. Declination: gray = measured declination values, green = declination values corrected using core orientation data collected with the Icefield MI-5. Susceptibility: magenta = SHMSL, black = WRMSL.

Figures **F16**, **F17**, **F18**, and **F19** also show MS measured on whole-round cores using the WRMSL and on archive-half sections using the SHMSL (see **Physical properties**). The WRMSL- and SHMSL-acquired susceptibility values were multiplied by 0.68 × 10^{-5} and (67/80) × 10^{-5}, respectively, to convert to the dimensionless volume SI unit (Blum, 1997). MS measurements are generally consistent between the two instruments and across the different holes for overlapping depth intervals and vary mostly between 5 × 10^{-5} and 50 × 10^{-5} SI. Variabilities in MS of the sediments generally mimic those of the NRM_{20mT} intensity, suggesting that magnetic minerals in these sediments that carry NRM are similar to those that dominate MS.

5.2. Magnetostratigraphy

Magnetostratigraphic interpretations are based on combined NRM (after 20 mT demagnetization) inclination and (orientation-corrected) declination data from archive-half sections and stepwise NRM demagnetization (up to 50 mT) data from cube samples. The geomagnetic field at the latitude of Site U1588 (37.96°N) has an expected inclination of 57° (–57°) during normal (reversed) polarity, assuming a geocentric axial dipole (GAD) field model. The AF demagnetization behavior of cube samples is illustrated in Figure **F20**. A steep normal overprint appears to be largely removed after AF demagnetization with peak fields of ~5–20 mT. Polarity information determined based on the cube sample data is indicated by black (normal), white (reversed), and gray (uncertain) squares in Figure **F16**. Identified polarity reversals at Site U1588 are shown in the Chron column in Figures **F16**, **F17**, **F18**, and **F19** and summarized in Table **T16**. The interpreted magnetostratigraphy is generally consistent with the biostratigraphy of the site (see **Biostratigraphy**).

Table T15. Disturbed APC core top intervals, Site U1588. **Download table in CSV format.**

Core, section	Offset top (cm)	Offset bottom (cm)	Top depth CSF-A (m)	Bottom depth CSF-A (m)	Top depth CSF-B (m)	Bottom depth CSF-B (m)	Comments
397-U1588A-							
2H-1	0	28	2.20	2.48	2.20	2.48	Disturbed core top
3H-1	0	44	11.70	12.14	11.70	12.12	Disturbed core top
4H-1	0	36	21.20	21.56	21.20	21.55	Disturbed core top
5H-1	0	76	30.70	31.46	30.70	31.43	Disturbed core top
6H-1	0	124	40.20	41.44	40.20	41.38	Disturbed core top
7H-1	0	140	49.70	51.10	49.70	51.00	Disturbed core top
8H-1	0	32	59.20	59.52	59.20	59.50	Disturbed core top
9H-1	0	60	68.70	69.30	68.70	69.26	Disturbed core top
11H-1	0	20	87.70	87.90	87.70	87.90	Disturbed core top
12H-1	0	52	97.20	97.72	97.20	97.69	Disturbed core top
13H-1	0	24	106.70	106.94	106.70	106.94	Disturbed core top
14H-1	0	84	116.20	117.04	116.20	117.04	Disturbed core top
15H-1	0	44	125.70	126.14	125.70	126.13	Disturbed core top
16H-1	0	72	135.20	135.92	135.20	135.88	Disturbed core top
17H-1	0	68	144.70	145.38	144.70	145.37	Disturbed core top
397-U1588B-							
2H-1	0	32	5.80	6.12	5.80	6.11	Disturbed core top
3H-1	0	68	15.30	15.98	15.30	15.97	Disturbed core top
4H-1	0	44	24.80	25.24	24.80	25.22	Disturbed core top
5H-1	0	68	34.30	34.98	34.30	34.98	Disturbed core top
6H-1	0	56	43.80	44.36	43.80	44.33	Disturbed core top
7H-1	0	60	53.30	53.90	53.30	53.86	Disturbed core top
8H-1	0	28	62.80	63.08	62.80	63.05	Disturbed core top
397-U1588D-							
2H-1	0	60	4.50	5.10	4.50	5.09	Disturbed core top
3H-1	0	24	14.00	14.24	14.00	14.23	Disturbed core top
4H-1	0	68	23.50	24.18	23.50	24.16	Disturbed core top
5H-1	0	136	33.00	34.36	33.00	35.86	Disturbed core top
6H-1	0	96	37.00	37.96	37.00	37.91	Disturbed core top
7H-1	0	96	46.50	47.46	46.50	47.40	Disturbed core top
8H-1	0	60	56.00	56.60	56.00	56.55	Disturbed core top
9H-1	0	16	65.50	65.66	65.50	65.65	Disturbed core top
10H-1	0	52	75.00	75.52	75.00	75.48	Disturbed core top
11H-1	0	48	84.50	84.98	84.50	84.90	Disturbed core top

The Brunhes/Matuyama (B/M) boundary (0.773 Ma) is recorded at ~146, ~149, ~148.5, and ~144 m CSF-B in Holes U1588A, U1588B, U1588C, and U1588D, respectively. Above the B/M boundary, the NRM_{20mT} inclination of all holes varies closely around the expected GAD inclination of ~57° except for core sections for which NRM measurements were likely compromised by flux jumps (Figures **F16**, **F17**, **F18**, **F19**). Below the B/M boundary, NRM of sections from all four holes is dominated by shallow/negative inclinations. In Hole U1588A, cube samples above the boundary show well-defined characteristic remanence with positive inclinations, whereas cube samples below the boundary show uncertain or reversed polarity components (Figure **F20**).

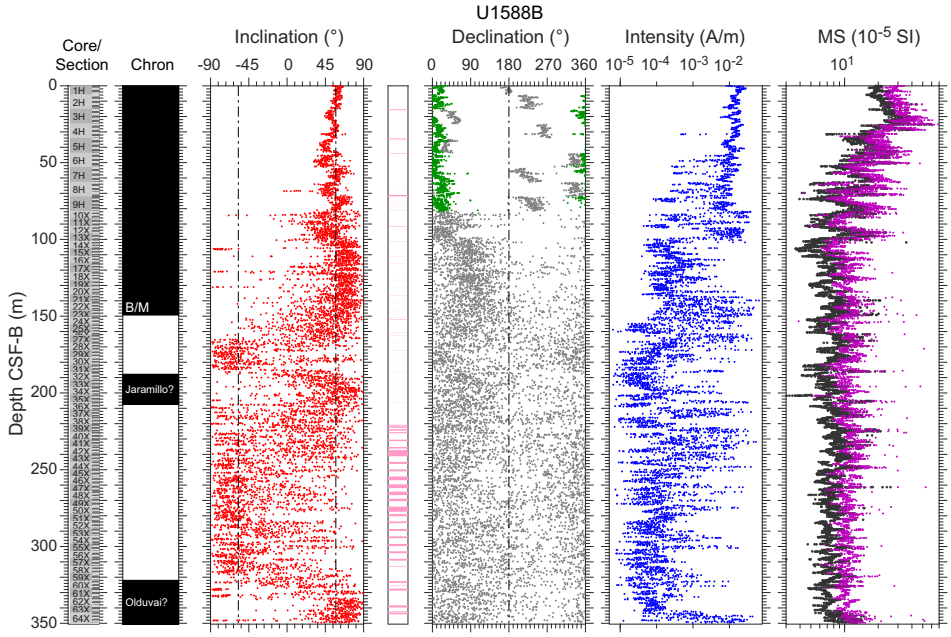

Figure F17. Paleomagnetism data after 20 mT AF demagnetization, Hole U1588B. Chron: black = normal polarity zone/boundary, white = reversed polarity zone/boundary, gray = uncertain polarity zone/boundary. Inclination: dashed lines = expected GAD inclinations at the site latitude during reversed and normal polarities. Pink shading = strongly disturbed intervals. Declination: gray = measured declination values, green = declination values corrected using core orientation data collected with the Icefield MI-5. Susceptibility: magenta = SHMSL, black = WRMSL.

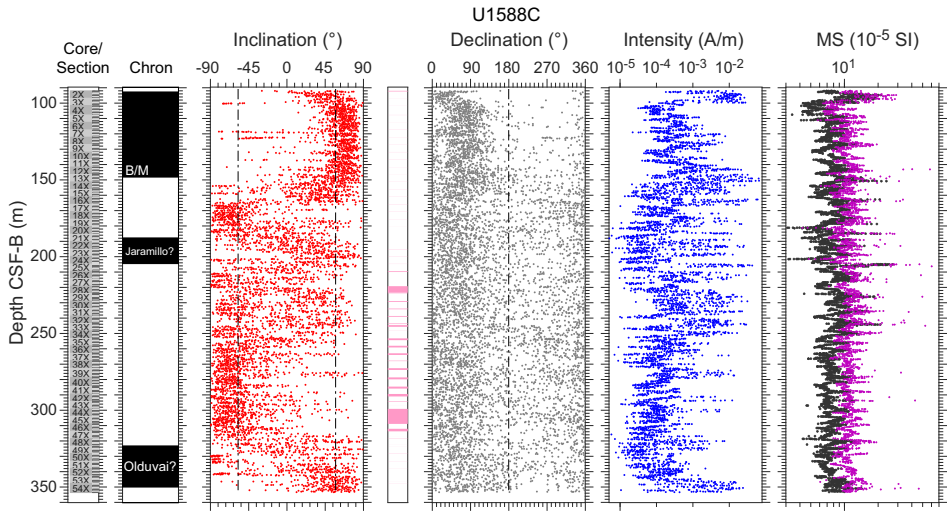

Figure F18. Paleomagnetism data after 20 mT AF demagnetization, Hole U1588C. Chron: black = normal polarity zone/boundary, white = reversed polarity zone/boundary, gray = uncertain polarity zone/boundary. Inclination: dashed lines = expected GAD inclinations at the site latitude during reversed and normal polarities. Pink shading = strongly disturbed intervals. Susceptibility: magenta = SHMSL, black = WRMSL.

The intervals at ~188–207, ~187.8–207.5, ~187.8–204.5, and ~189–206.7 m CSF-B in Holes U1588A, U1588B, U1588C, and U1588D, respectively, are dominated by positive inclinations (Figures **F16**, **F17**, **F18**, **F19**). Cube samples from this interval in Hole U1588A yielded normal or uncertain polarity (Figures **F16**, **F20**). We interpret these intervals as the Jaramillo Subchron (0.99–1.07 Ma). This interpretation is consistent with the biostratigraphy (see **Biostratigraphy**).

The top of the Olduvai Subchron (1.775 Ma) is identified at ~320, ~322, ~323, and ~322 m CSF-B in Holes U1588A, U1588B, U1588C, and U1588D, respectively. At these depths, the NRM_{20mT} inclination shifts downhole from mostly negative to positive values, scattering around 57°. NRM of cube samples from Hole U1588A above the top of Olduvai Subchron is dominated by reversed polarity components, whereas NRM of cube samples from below this depth mainly shows uncertain or normal polarity components (Figure **F20**). The bottom of the Olduvai Subchron (1.934 Ma) is identified only in the deepest Hole U1588D at ~351 m CSF-B, where NRM_{20mT} of sections appears to shift downhole from mainly positive inclinations to dominantly shallow or negative inclinations (Figure **F19**). The Matuyama/Gauss boundary was not identified in any of the holes, indicating that the base of the section is younger than 2.6 Ma (Table **T16**).

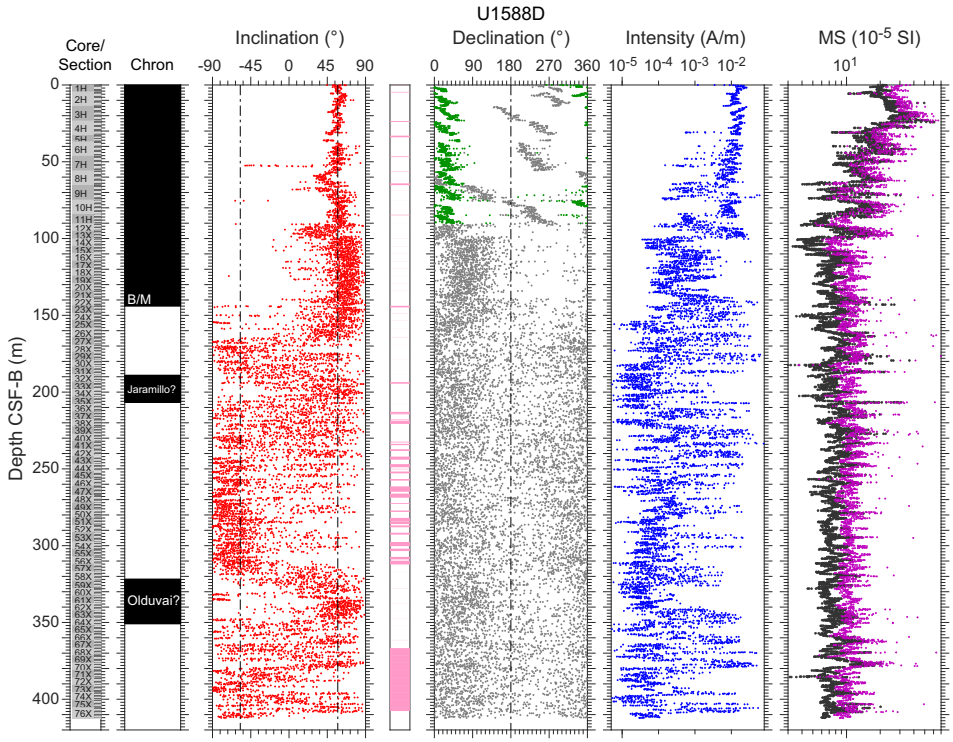

Figure F19. Paleomagnetism data after 20 mT AF demagnetization, Hole U1588D. Chron: black = normal polarity zone/boundary, white = reversed polarity zone/boundary, gray = uncertain polarity zone/boundary. Inclination: dashed lines = expected GAD inclinations at the site latitude during reversed and normal polarities. Pink shading = strongly disturbed intervals. Declination: gray = measured declination values, green = declination values corrected using core orientation data collected with the Icefield MI-5. Susceptibility: magenta = SHMSL, black = WRMSL.

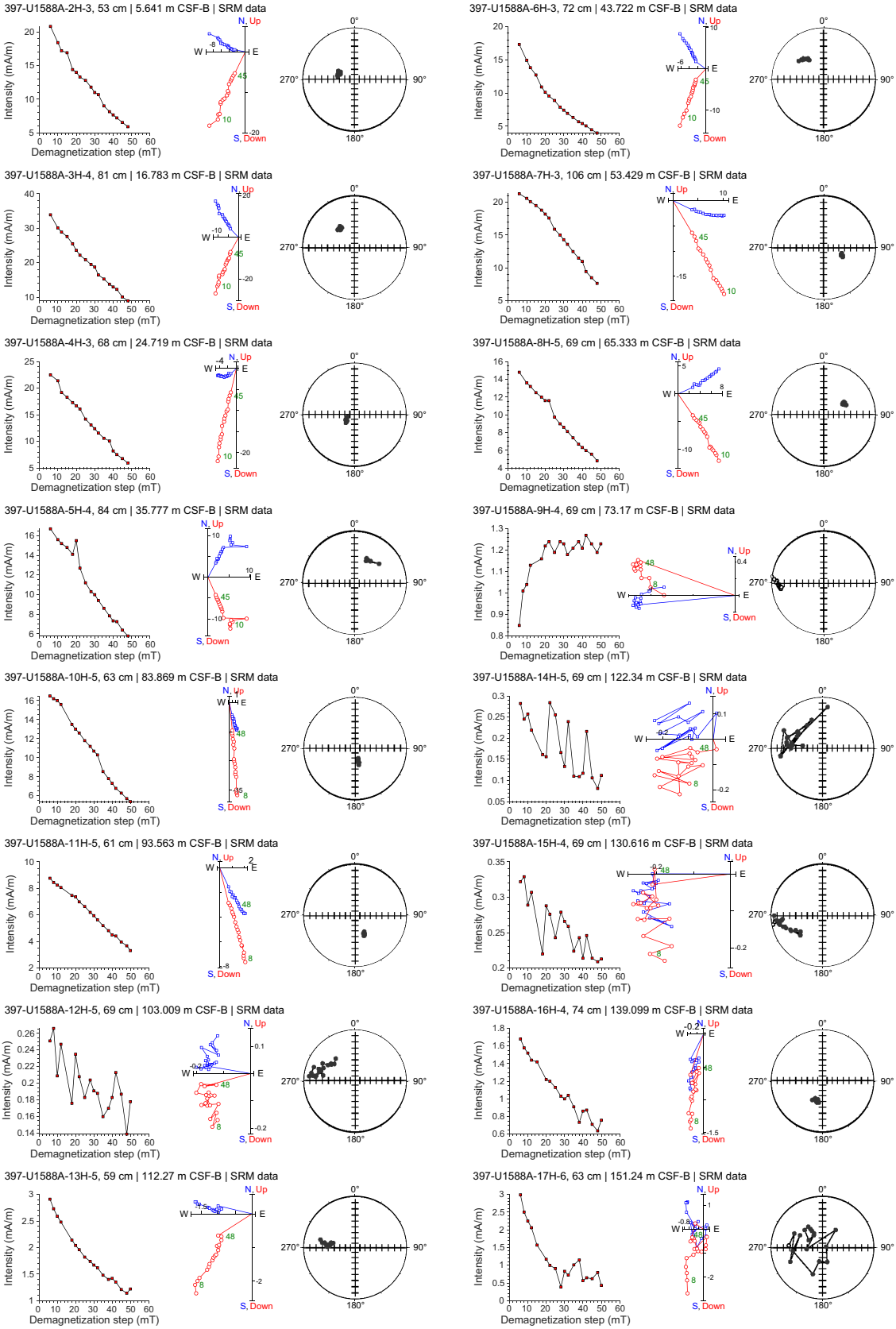

Figure F20. Discrete cube sample AF demagnetization results, Hole U1588A. Results are organized by sample depth. All samples: left = intensity variation with progressive AF demagnetization, middle = NRM demagnetization data on orthogonal (Zijderveld) projections, right = equal area projections. Orthogonal projection plots: blue squares = horizontal projections, red circles = vertical projections. Equal area projection plots: solid circles = positive inclinations, open circles = negative inclinations. Measurements that were influenced by flux jumps and measurements from the first few demagnetization steps (typically <4–10 mT) that are heavily influenced by drilling-induced overprint are removed. (Continued on next two pages.)

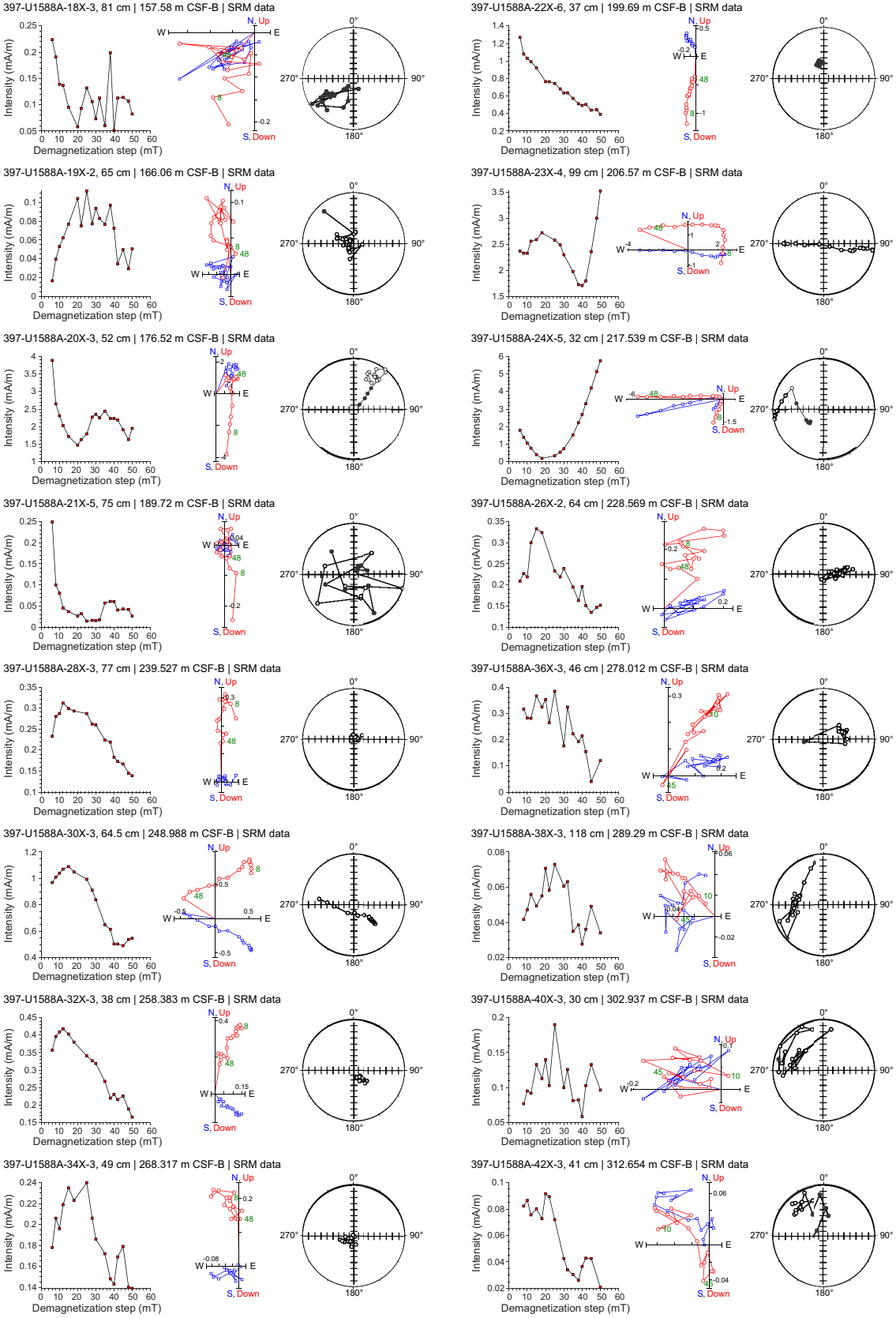

Figure F20 (continued). (Continued on next page.)

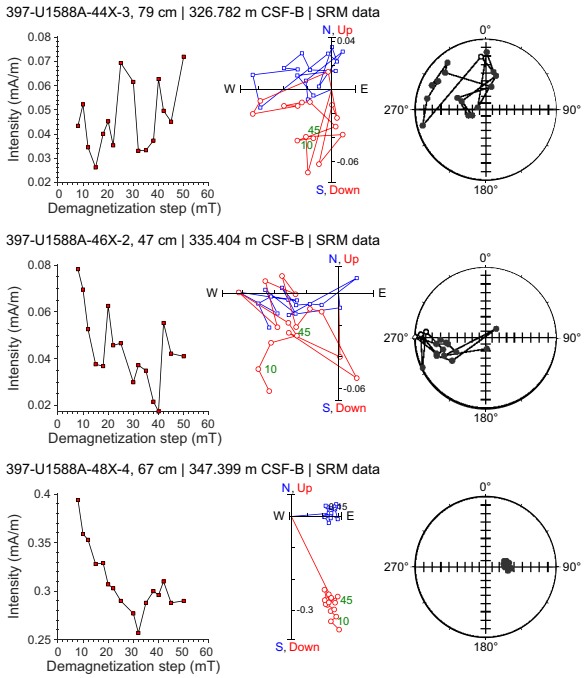

Figure F20 (continued).

Table T16. Identified polarity boundaries, Site U1588. **Download table in CSV format.**

Polarity boundaries	Age (Ma)	Top depth CSF-B (m)	Bottom depth CSF-B (m)	Midpoint depth CSF-B (m)	Depth Error (±m)
Hole U1588A					
(B) C1n (Brunhes/Matuyama)	0.773	142.80	150.00	146.40	3.60
(T) C1r.1n (Jaramillo)	0.99	185.50	190.50	188.00	2.50
(B) C1r.1n (Jaramillo)	1.07	204.00	210.00	207.00	3.00
(T) C2n (Olduvai)	1.775	316.00	324.00	320.00	4.00
(B) C2n (Olduvai)	1.934	—	—	—	—
(T) C2An.1n (Matuyama/Gauss)	2.595	—	—	—	—
Hole U1588B					
(B) C1n (Brunhes/Matuyama)	0.773	140.50	158.00	149.25	8.75
(T) C1r.1n (Jaramillo)	0.99	184.60	191.00	187.80	3.20
(B) C1r.1n (Jaramillo)	1.07	204.00	211.00	207.50	3.50
(T) C2n (Olduvai)	1.775	317.00	327.00	322.00	5.00
(B) C2n (Olduvai)	1.934	—	—	—	—
(T) C2An.1n (Matuyama/Gauss)	2.595	—	—	—	—
Hole U1588C					
(B) C1n (Brunhes/Matuyama)	0.773	144.00	153.00	148.50	4.50
(T) C1r.1n (Jaramillo)	0.99	184.00	191.60	187.80	3.80
(B) C1r.1n (Jaramillo)	1.07	201.00	208.00	204.50	3.50
(T) C2n (Olduvai)	1.775	317.50	329.00	323.25	5.75
(B) C2n (Olduvai)	1.934	—	—	—	—
(T) C2An.1n (Matuyama/Gauss)	2.595	—	—	—	—
Hole U1588D					
(B) C1n (Brunhes/Matuyama)	0.773	138.00	150.00	144.00	6.00
(T) C1r.1n (Jaramillo)	0.99	186.00	192.00	189.00	3.00
(B) C1r.1n (Jaramillo)	1.07	204.40	209.00	206.70	2.30
(T) C2n (Olduvai)	1.775	318.50	325.00	321.75	3.25
(B) C2n (Olduvai)	1.934	349.30	352.50	350.90	1.60
(T) C2An.1n (Matuyama/Gauss)	2.595	—	—	—	—

6. Geochemistry

Geochemistry at Site U1588 involved collection and measurements of IW samples for salinity, alkalinity, pH, major ions (Na, K, Ca, Cl, and SO_4), nutrients (NH_4 and PO_4), and trace elements (Sr, Li, Fe, Mn, B, and Ba); headspace gases for methane (CH_4) concentrations; and bulk sediment samples for total organic carbon (TOC), total inorganic carbon (TIC)/$CaCO_3$, total nitrogen (TN), total sulfur (TS), and for bulk mineralogical abundance (by XRD) and elemental composition (by inductively coupled plasma–atomic emission spectrometry [ICP-AES]). In total, 54 IW samples were taken from Hole U1588A (see **Geochemistry** in the Expedition 397 methods chapter [Abrantes et al., 2024a]). A 5 or 10 cm sample was taken at the base of every section for the upper 30 m, at the base of Sections 2 and 6 to 49 m CSF-A, and then at the base of Section 6 (i.e., the second to last section recovered from every core) to the bottom of the hole. IW samples show evidence of microbially mediated respiration and other diagenetic reactions.

IW alkalinity, ammonium (NH_4), and phosphate (PO_4) increase in the upper 50 m, whereas SO_4 shows a two-step decrease in the upper 50 m, indicating organic matter respiration. At this site, SO_4 reaches zero and remains low, whereas CH_4 levels increase to about 45,000 ppmv at 50 m CSF-B but decline to ~5,000 ppmv by 100 m CSF-B to the bottom of the hole.

$CaCO_3$ content ranges 16.0–53.6 wt% (average = 30.2 wt%). This coulometer-determined $CaCO_3$ content shows consistent results with stoichiometric $CaCO_3$ calculated from the elemental Ca concentrations measured by ICP-AES, and it is positively correlated with L* reflectance and negatively correlated with NGR. TOC, TN, and TS values at Site U1588 are generally low, ranging 0.30–1.89 wt% TOC (mean = 0.74 wt%), 0.042–0.189 wt% TN (mean = 0.085 wt%), and 0–3.18 wt% TS (mean = 0.291 wt%). Organic C/N ratios (3.04–16.5; mean = 8.97) suggest that organic matter is marine/lacustrine dominated.

Bulk sediment SiO_2, K_2O, and TiO_2 contents show strong positive correlations with Al_2O_3, indicating dominance of terrigenous detritus. This is also generally observed for minor elements including Sc, Y, Cr, V, and Zr. Relatively weak correlations of Fe_2O_3, MgO, Na_2O, MnO, and Ba with Al_2O_3 are observed, due to the widespread presence of authigenic and biogenic phases; that is, pyrite, dolomite, and/or Mg-bearing calcite, halite (NaCl) precipitated from seawater, Mn hydroxides, and barite ($BaSO_4$), respectively. Bulk sediment Ca primarily represents biogenic carbonate ($CaCO_3$), and because of the incorporation of Sr into biogenic carbonates, both elements show an inverse relationship with Al. Elemental ratios of Ca/Ti, Si/Al, Ti/Al, Zr/Al, K/Al, Sr/Ca, and estimated biogenic Ba are selected as useful proxies for provenance, weathering, and productivity.

6.1. Headspace and void hydrocarbon gases

Headspace samples were collected from the lowermost section of each core (or every other half core) from Holes U1588A and U1588D. CH_4 concentrations peak around 50 m CSF-B, with values around 45,000 ppmv (Figure **F21**). Headspace gas data should be treated with caution at this site because cores fractured due to high gas concentrations, opening voids upon recovery. As a result, holes were drilled in the core liner on the catwalk, venting void gas and leaving sediment with residually low gas concentrations. Since headspace samples were taken after void gas was vented and cores were split, the gas concentrations in these samples are likely much lower than in situ values. However, void gas was sampled in 7 cores, and results show they almost entirely comprise CH_4 (Table **T17**).

Despite gas loss, the methane/ethane ratios should not be affected by low absolute gas concentrations. Ethane is detectable between 49 and 412 m CSF-B, but C_1/C_2 (i.e., CH_4/C_2H_6) ratios remain high (3,500–20,000), indicating that there is no danger to drilling.

6.2. Interstitial water geochemistry

Shortly after extracting IW, aliquots of the recovered water were apportioned for salinity, chlorinity, alkalinity, and pH measurements. In addition, major and minor elemental composition were measured with ion chromatography (IC) and ICP-AES and for NH_4 and PO_4 by spectrophotometry (Table **T18**). Some of the significant trends are highlighted below.

6.2.1. Salinity, sodium, potassium, chloride

Salinity, Na, and Cl concentrations are relatively constant in Hole U1588A, with values close to seawater (Figure **F22**). Na measured with IC has a mean value of 491.9 ± 4.3 mM and is slightly offset toward lower values than data obtained using ICP-AES (504.6 ± 6.3 mM). Cl measured with IC has a mean value of 563.4 ± 7.8 mM, which is nearly identical to values obtained using $AgNO_3$ titration (557.0 ± 6.9 mM). K declines in the upper part of Hole U1588A from a value near 11.5 mM at the top of the hole to a minimum of 7.64 at 169.8 m CSF-B and then increases to the bottom, reaching values similar to those observed at the top of the hole.

6.2.2. Alkalinity, pH, ammonium, phosphate

Alkalinity, pH, NH_4, and PO_4 increase rapidly at the top of Hole U1588A and trend with depth (Figure **F21**). Alkalinity increases from 5.1 mM at the top of the hole to 12.5 mM at 10.8 m CSF-B, declines slightly to 6 mM at 85.9 m CSF-B, and then increases steadily, reaching a maximum of 29.4 mM in the lowermost sample (397-U1588A-49X-3, 140–150 cm). pH values increase from 7.58 in the uppermost sample to 7.92 at 22.58 m CSF-B then remain roughly constant, averaging 7.87 ± 0.06, to the bottom of the hole. NH_4 concentrations are lowest in the uppermost sample, 333.5 µM, increase rapidly along with alkalinity to a value of 1790.8 µM at 13.1 m CSF-B, and then continue to increase downhole at a slower rate, reaching a maximum of 8770.7 µM at 341.9 m CSF-B. The highest calibration standard run with the NH_4 samples had a concentration of 3000 µM, so all higher reported values are based on extrapolating the calibration, and exact values should thus be treated with caution. PO_4 is 12.4 µM in the uppermost sample and peaks slightly deeper than the shallow alkalinity maximum at values around 30 µM between 18.8 and 22.6 m CSF-B. PO_4 concentrations average 15.6 ± 0.8 µM between 76.5 and 200.4 m CSF-B and then increase slightly to the bottom of the hole.

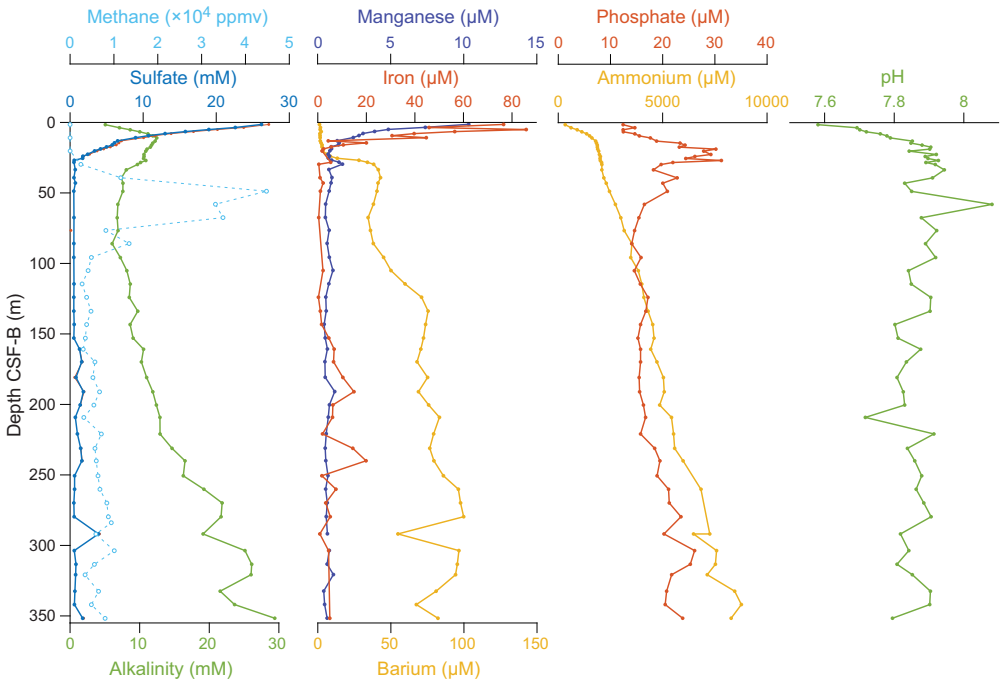

Figure F21. Dissolved SO_4 with alkalinity and headspace CH_4; dissolved Fe, Mn, and Ba; NH_4 and PO_4; and pH, Hole U1588A. Dashed line = methane data, showing that the measured concentrations are likely too low due to gas expansion and fracturing of sediment that led to gas loss.

Table T17. Headspace hydrocarbon gas concentrations, Hole U1588A. **Download table in CSV format.**

Table T18. IW chemistry, Hole U1588A. **Download table in CSV format.**

The increases in alkalinity, NH_4, and PO_4 in the upper part of Hole U1588A are the result of organic matter respiration associated with SO_4 reduction, assuming a generic composition of $(CH_2O)_{106}(NH_3)_{16}(H_2PO_4)$, which produces alkalinity (in the form of HCO_3^-), PO_4, and NH_4. However, the high alkalinity and NH_4 values observed deeper in the hole cannot be explained by SO_4 reduction and therefore must have another source (Figure **F21**).

6.2.3. Sulfate, iron, manganese, barium

SO_4 values are near seawater in the uppermost sample (26.2 mM in 397-U1588A-1H-1, 143–148 cm) and then decrease rapidly, reaching zero by 26.8 m CSF-B (Figure **F21**). The SO_4 decline at Site U1588 is not as pronounced as at Site U1385 but not as consistent as at Site U1587. The decrease from 0 to 13.1 m CSF-B is steeper than that between 13.1 and 26.8 m CSF-B, and the change in slope is nearly coincident with the peak in alkalinity at 10.8 m CSF-B. When SO_4 reaches zero, CH_4 increases, reaching a maximum of 44,800 ppmv at 48.8 m CSF-B. However, as discussed in **Headspace and void hydrocarbon gases**, the CH_4 data are unreliable owing to sediment fracturing due to gas expansion. Ba concentrations are <5 µM to 20.2 m CSF-B and increase rapidly to 42.9 µM at 39.2 m CSF-B, coinciding with the abrupt SO_4 decrease. This indicates the dissolution of $BaSO_4$. Fe and Mn concentrations decrease in the uppermost ~20 m. Mn concentrations decline faster than Fe, likely reflecting the more favorable reduction of Mn oxides over Fe oxides under anoxic pore water conditions.

These patterns, combined with the observed increase in alkalinity in the upper part of the sediment column, indicates intense SO_4 reduction and methanogenesis. The $BaSO_4$ dissolution due to the rapid and intense SO_4 reduction is also evident. Peaks in redox-sensitive elements such as Fe and Mn indicate microbially mediated respiration reactions within the sediment.

6.2.4. Calcium, magnesium, strontium

Ca concentrations in the IW decrease in the upper 27 m from a value of 10.1 mM in the uppermost sample (397-U1588A-1H-1, 143–148 cm) to 3.0 mM at 26.8 m CSF-B (Figure **F23**). There is a slight change in the steepness of the Ca decline at 13.1 m CSF-B, which coincides with the change in steepness of the SO_4 decline and is slightly deeper than the shallow alkalinity peak at 10.8 m CSF-B. Below ~25 m CSF-B, Ca concentrations are around 25 mM with only slight variability. Mg concentrations decline in the upper part of the hole from 54.9 mM in the uppermost sample to 31.4 mM at 95.7 m CSF-B and then remain roughly constant at nearly 30 mM. Sr concentrations decline from 88.0 µM in the uppermost sample to a minimum value of 62.7 µM at 22.6 m CSF-A, following a similar pattern to Ca. Below this depth, Sr steadily increases to a maximum value of

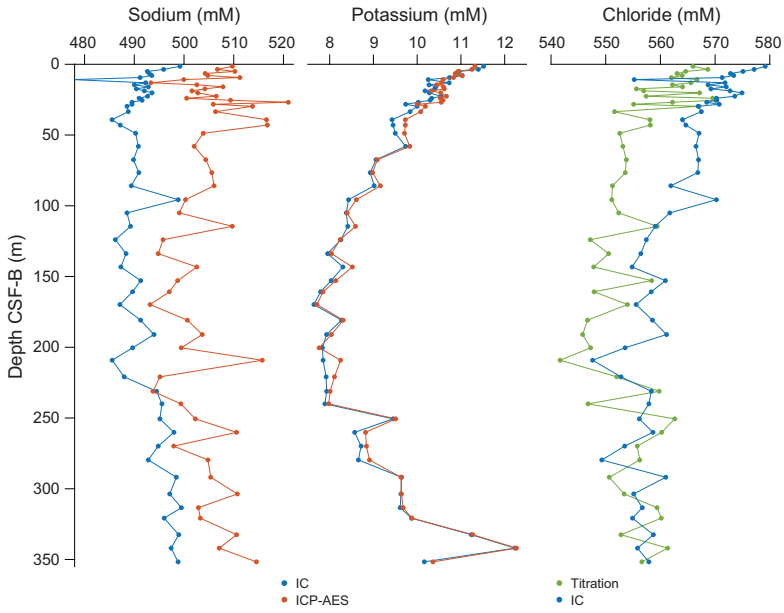

Figure F22. Dissolved Na, K, and Cl concentrations, Hole U1588A.

146.4 µM in the lowermost sample (49X-3, 140–150 cm). The Ca, Mg, and Sr decreases in the upper 20 m could be the result of authigenic $CaCO_3$ precipitation, driven by high pore water alkalinity associated with SO_4 reduction.

6.2.5. Silicon, lithium, boron

Si concentrations vary downhole, with lower values (average = 194.3 ± 78.3 µM) in the upper ~150 m CSF-B and higher values (average = 458.1 ± 87.2 µM) deeper in the hole (Figure **F24**). Li concentrations are relatively constant (~23 µM) in the top ~100 m of Hole U1588A and increase to a maximum of 212.4 µM at the bottom of the hole. B concentrations increase sharply in the upper 13.3 m from 496.0 µM in the uppermost sample to a maximum of 569.0 µM, and then concentrations decline and plateau at 260 µM by ~200 m CSF-B.

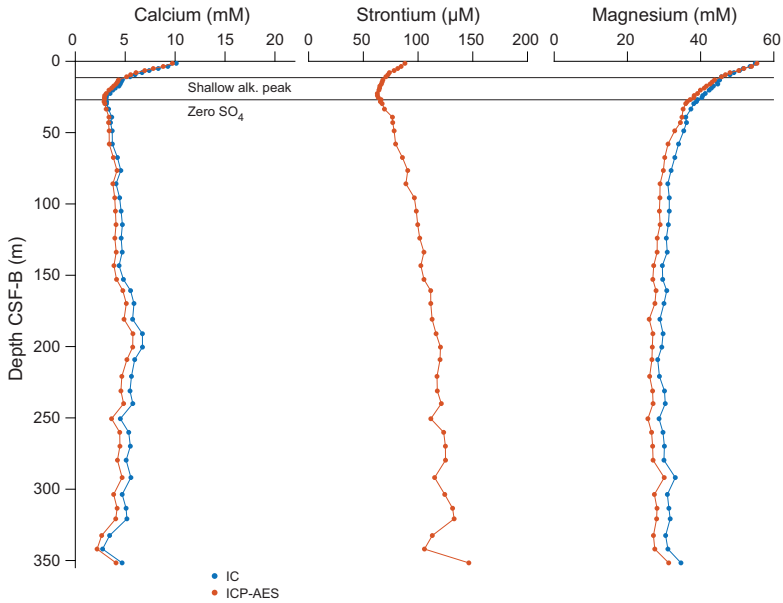

Figure F23. Dissolved Ca, Sr, and Mg, Hole U1588A.

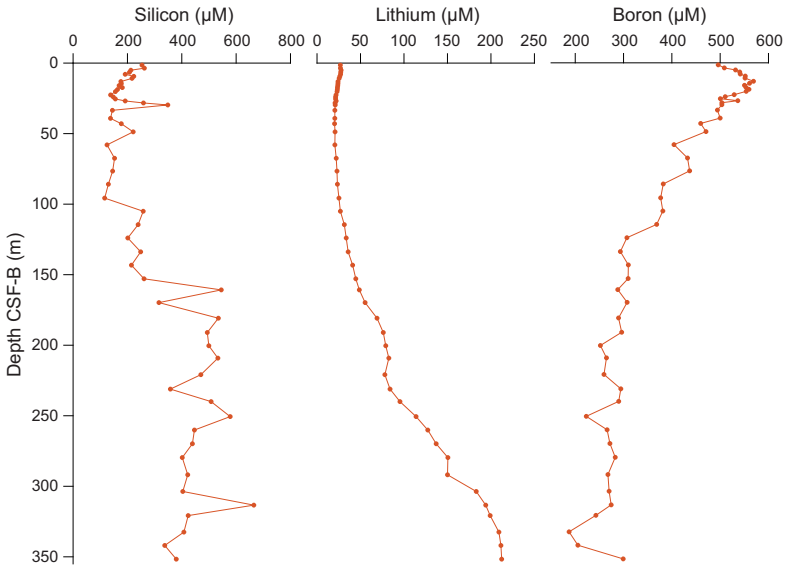

Figure F24. Dissolved Si, Li, and B, Hole U1588A.

6.3. Bulk sediment geochemistry

6.3.1. Calcium carbonate (total inorganic carbon)

In Hole U1588A, TIC and TC/TN/TS were measured in samples taken from the working half of split core sections at a resolution of two per core/one per half core. Again, the light and dark intervals were targeted to improve correlations with other physical properties.

A 100% $CaCO_3$ standard was analyzed every ~10 samples (mean = 99.99 ± 1σ [standard deviation] = 0.98 wt%; n = 12) (Table **T19**). Samples were not measured until the standard was within ~1.5% of 100 wt%.

The mean $CaCO_3$ content from Hole U1588A is 30.2 wt%, but variability is high (±1σ = 8.06 wt%; range = 16.0–53.6 wt%). $CaCO_3$ content and variability are relatively constant throughout (Figures **F25**, **F26**; Table **T20**). $CaCO_3$ correlates positively with L* reflectance (adjusted R^2 = 0.265) and negatively with NGR as documented at Site U1587 (adjusted R^2 = 0.780) (see Figures **F26**, **F27**, **F28**, and **F29** in the Site U1587 chapter [Hodell et al., 2024]). Using the measured elemental Ca concentrations from ICP-AES data, the stoichiometric $CaCO_3$ was calculated to compare with the shipboard-measured total $CaCO_3$ weight percent by coulometer (Figures **F25**, **F26**, **F27**, **F28**). Although the absolute numbers are not the same, trends in the data are similar.

6.3.2. Total organic carbon

All samples were simultaneously analyzed for TC alongside TIC, TN, and TS (Figure **F29**; Table **T21**). TOC is defined as the difference between TC and TIC.

Table T19. Carbonate standards analysis, Site U1588. **Download table in CSV format.**

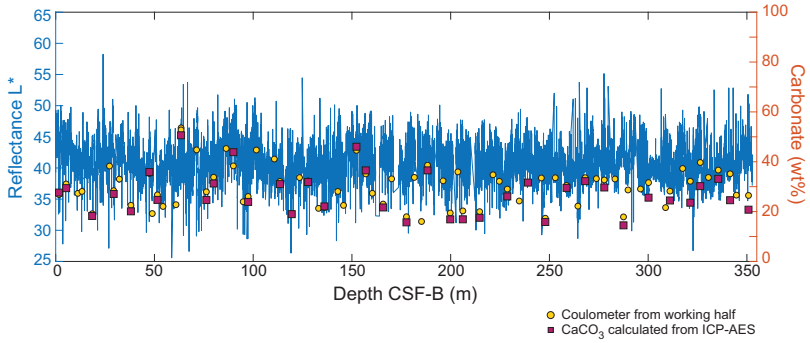

Figure F25. Discrete measurements of $CaCO_3$ by coulometry and ICP-AES L* reflectance, Hole U1588A.

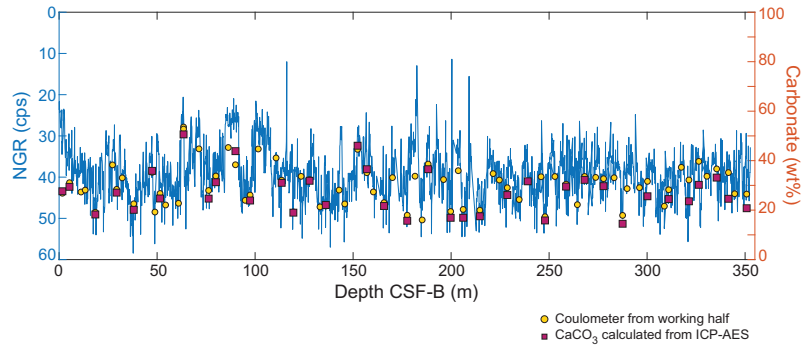

Figure F26. Discrete measurements of $CaCO_3$ with NGR, Hole U1588A. cps = counts per second.

Table T20. Inorganic carbon and $CaCO_3$ results, Site U1588. **Download table in CSV format.**

Two internal standards (sulfanilamide and Buffalo River Sediment [BRS]) were used to calibrate the elemental analyzer. BRS was used to assess the reproducibility of TC, TN, and TS and was run at least every ~10 samples; the 1σ of TC in NIST BRS (n = 10) is 0.074 wt% (Table **T22**). TOC content in Hole U1588A is generally low (mean = 0.74 ± 0.25 wt%; range = 0.30–1.89 wt%). TOC content and variability are relatively constant throughout (Figure **F29**; Table **T23**). $CaCO_3$ and TOC are not strongly correlated (R^2 = 0.10).

6.3.3. Total nitrogen

All sedimentary nitrogen is assumed to be organic. The 1σ of TN in NIST BRS (n = 10) is ±0.013 wt% (Table **T22**).

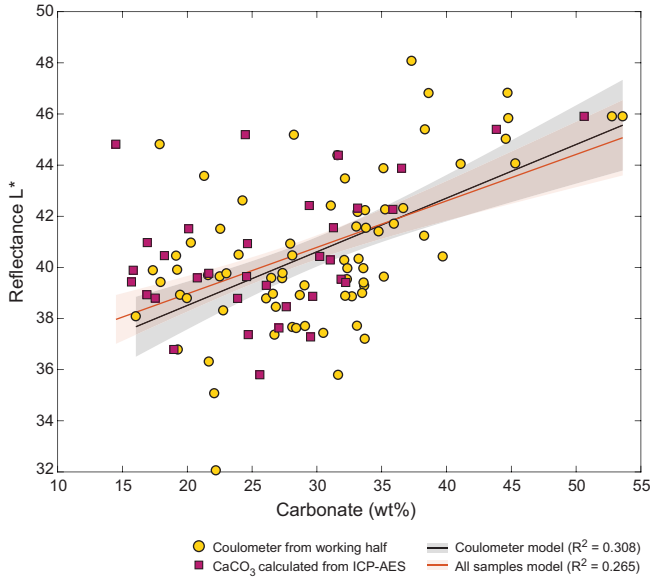

Figure F27. Crossplot and linear regression of $CaCO_3$ and L* reflectance, Hole U1588A. Red line = linear regression with 95% confidence interval (CI) for all carbonate data (including direct measurements by coulometry and calculated values from bulk sediment ICP-AES data), black solid line = linear regression with 95% CI for all coulometry data.

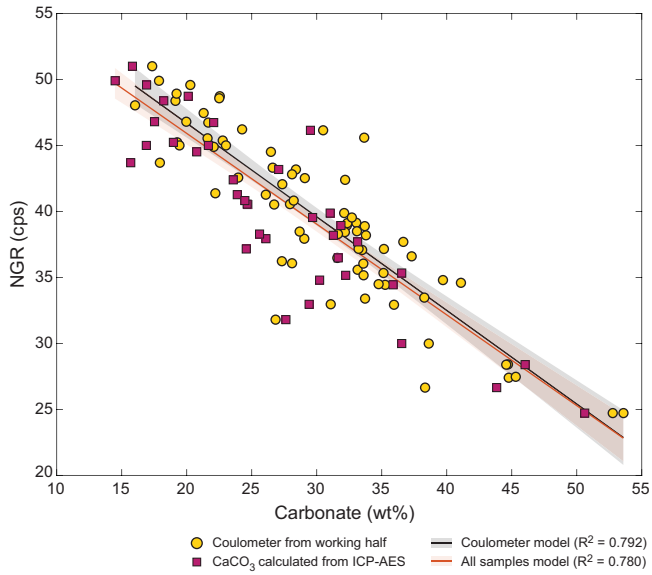

Figure F28. Crossplot and linear regression of $CaCO_3$ and NGR, Hole U1588A. cps = counts per second, red line = linear regression with 95% CI for all carbonate data (including direct measurements by coulometry and calculated values from bulk sediment ICP-AES data), black line = linear regression with 95% CI for all coulometry data.

TN levels in Hole U1588A are also very low (mean = 0.085 ± 0.023 wt%; range = 0.042–0.189 wt%) (Table **T24**). TN content and variability are relatively constant throughout (Figure **F29**).

6.3.4. Organic C/N ratios

The ratio of sedimentary TOC/TN (C/N) can fingerprint particulate organic matter: marine and lacustrine algae have ratios of 0–10, whereas terrestrial plants exist in a much broader C/N space (25–75) (Meyers 1994, 1997).

The mean C/N is 8.97 ± 2.62 (range = 3.04–16.5) (Table **T25**). C/N ratios and variability are relatively constant throughout (Figure **F29**) and diagnostic of marine/lacustrine algal sources.

6.3.5. Total sulfur

The 1σ of TS in NIST BRS (n = 10) is ±0.073 wt% (Table **T22**).

Similar to TOC and TN, TS concentrations are very low (mean = 0.291 ± 0.487 wt%; range = 0–3.18 wt%) (Table **T26**). TS content and variability are relatively constant throughout (Figure **F29**).

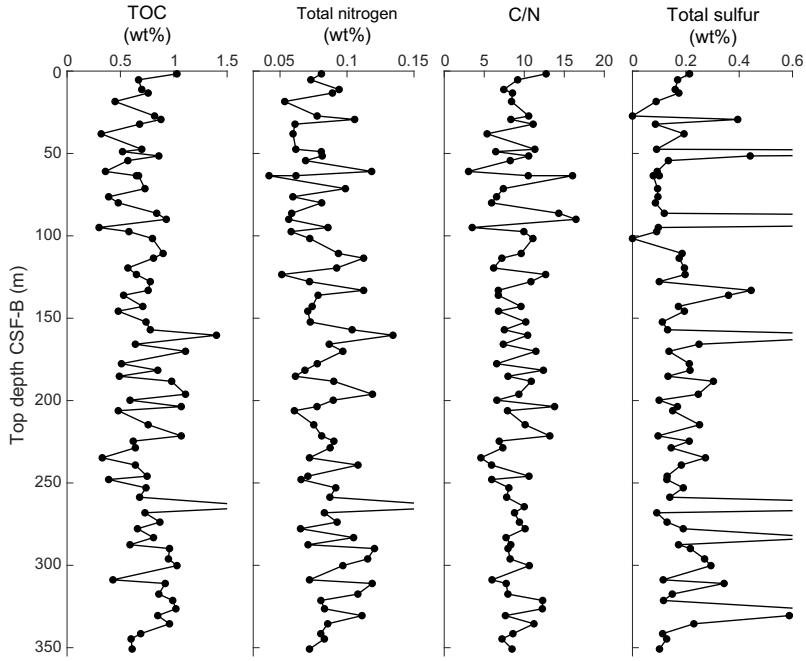

Figure F29. TOC, TN, C/N, and TS vs. top depth, Hole U1588A.

Table T21. Carbon-hydrogen-nitrogen-sulfur results, Hole U1588A. **Download table in CSV format.**

Table T22. N, C, S standards analysis, Site U1588. **Download table in CSV format.**

Table T23. TOC results, Site U1588. **Download table in CSV format.**

Table T24. TN results, Site U1588. **Download table in CSV format.**

Table T25. C/N results, Site U1588. **Download table in CSV format.**

Table T26. TS results, Site U1588. **Download table in CSV format.**

6.3.6. Major and minor elements

Major and minor element concentrations were measured on 38 samples from Hole U1588A using ICP-AES (Table **T27**). Replicate analyses of 8 international reference standards (n = 18) have relative standard deviations (RSD) of <5% for all major elements (excerpt for P_2O_5) and <10% for most of the minor elements reported.

The elemental oxides of SiO_2, K_2O, and TiO_2 show robust positive correlation against Al_2O_3 with a near-zero intercept, indicating the dominance of terrigenous detritus (Figure **F30**). This is also generally observed for the minor elements including Sc, Y, Cr, V, and Zr. Relatively weak correlations are observed for Fe_2O_3, MgO, Na_2O, MnO, and Ba against Al_2O_3, due to the widespread presence of authigenic and biogenic phases, that is, pyrite, dolomite, and/or Mg-bearing calcite, halite (NaCl) precipitated from seawater, Mn hydroxides, and $BaSO_4$, respectively. The bulk sediment Ca

Table T27. Sedimentary major and minor element concentrations, Site U1588. **Download table in CSV format.**

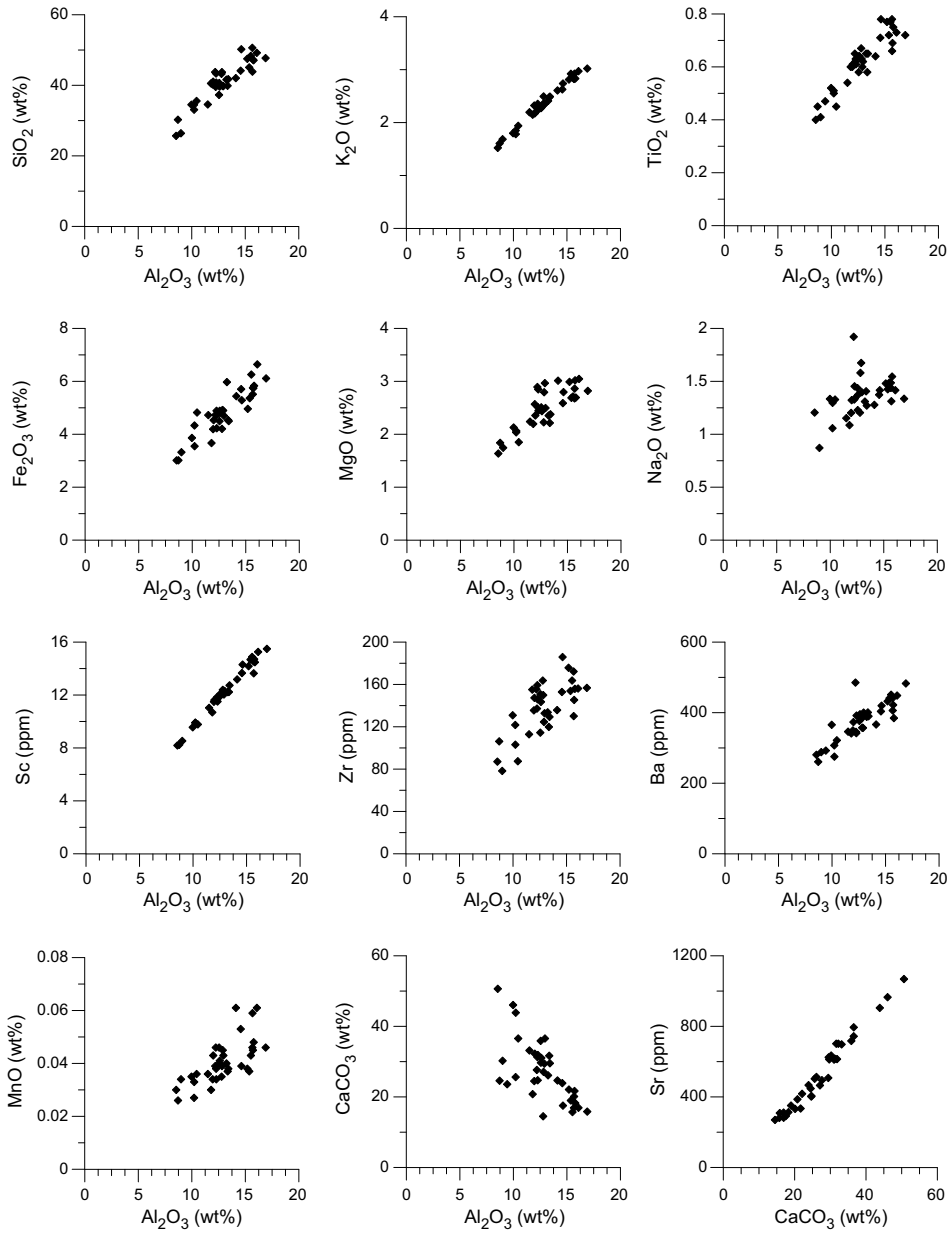

Figure F30. Crossplots of sedimentary major and minor element concentrations, Hole U1588A.

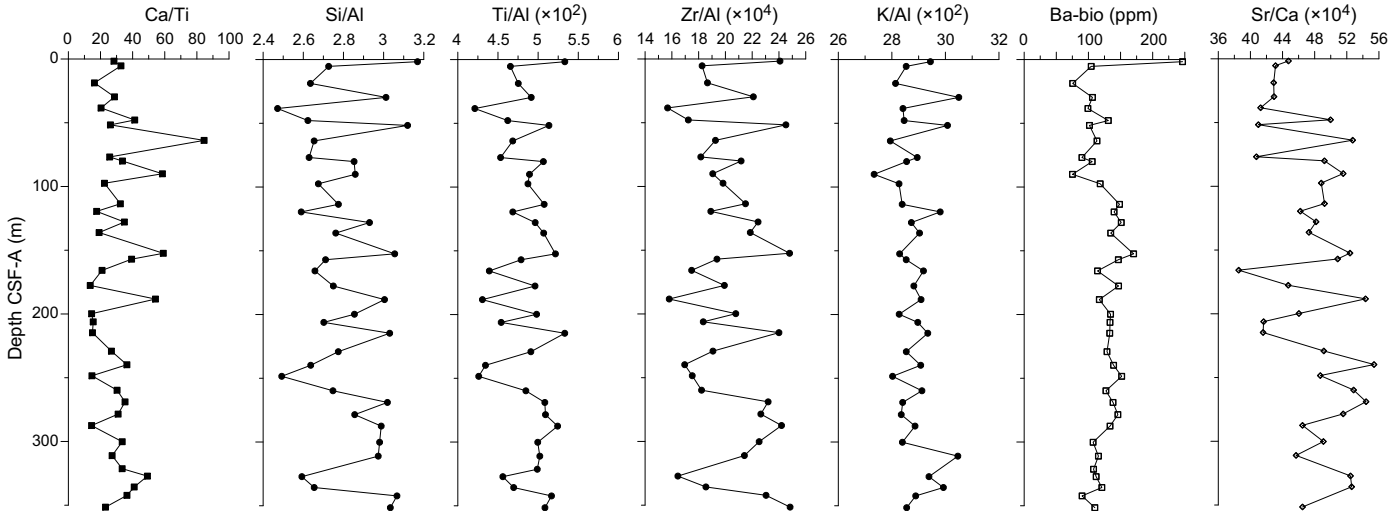

Figure F31. Downhole profiles of bulk sedimentary Ca/Ti, Si/Al, Ti/Al, Zr/Al, K/Al, biogenic Ba (Ba-bio), and Sr/Ca, Hole U1588A.

primarily represents biogenic $CaCO_3$, and because of the incorporation of Sr into biogenic carbonates, both elements show an inverse relationship with Al. In the plot of $CaCO_3$ vs. Al_2O_3, the deviating data points are due to detrital $CaCO_3$ (Figure **F30**).

The Ca/Ti ratio reflects the relative contributions of $CaCO_3$ versus terrigenous detritus in the sediments. The Ca/Ti ratios range ~13–84, with larger variations at ~50–200 m CSF-B and smaller variations in the upper 50 m and ~200–350 m CSF-B (Figure **F31**). Selected lithogenic elements are normalized to Al as a proxy for provenance, weathering, and productivity (Figure **F31**). In addition, the Si/Al ratio may serve as a proxy for grain size, mainly reflecting the abundance of quartz versus clay minerals. The Ti/Al and Zr/Al ratios in this area are widely recognized as indicators of North African dust, and the K/Al ratio is used to reflect the input of river-borne material and associated chemical weathering intensity (Wu et al., 2016). Similarities between Si/Al, Ti/Al, and Zr/Al profiles indicate changes in dust input and wind intensity. Si/Al, Ti/Al, and Zr/Al have no discernible long-term downhole trend. The K/Al profile shows larger variations in the upper 100 m and the lowermost 50 m and smaller variations at ~100–300 m CSF-A.

$BaSO_4$ content in marine sediments is a widely recognized proxy for export productivity (Paytan and Griffith, 2007). Assuming a constant Ba/Al ratio of 0.0037 for the terrigenous aluminosilicate component (Reitz et al., 2004), the biogenic Ba (i.e., Ba-bio, mostly $BaSO_4$) can be calculated. Despite possible $BaSO_4$ dissolution at this site (Figure **F21**), there may still be ~70–200 ppm residual $BaSO_4$ with relatively small changes downhole. The Sr/Ca profile shows larger variations downhole, probably linked to changes in aragonite content.

7. Physical properties

Physical properties measurements were made on whole-round cores, split cores, and discrete samples. High-resolution (2 or 4 cm steps) nondestructive measurements of GRA bulk density and MS were made on whole-round sections from all holes. NGR was measured on all whole-round sections at a 10 or 20 cm resolution. *P*-wave caliper (PWC) measurements were taken at a resolution of one per core. However, only the data from Cores 397-U1588A-1H through 7H were recorded because of extreme core expansion below Core 8H. MAD discrete samples were measured at a resolution of one measurement per core for all cores from Hole U1588A. Thermal conductivity was measured once per core for all cores from Hole U1588A. Color reflectance spectrophotometry and split core point MS (MSP) measurements were carried out at 2, 4, or 5 cm steps on all archive halves. X-ray images of whole-round sections were taken for all core sections from Hole U1588A and Cores 397-U1588D-64X through 76X. In this site chapter, we use the CSF-B depth scale instead of the CSF-A depth scale because severe sediment expansion due to the high gas

content resulted in a significant overlap of the physical properties data between cores when plotted on the CSF-A depth scale.

7.1. Bulk density

Bulk density values were measured using the WRMSL and Special Task Multisensor Logger (STMSL) for GRA bulk density and discrete samples for MAD bulk density.

GRA bulk density was measured at 2 or 4 cm resolution on all whole-round sections from all holes. Measured GRA bulk density increases from ~1.4 g/cm^3 at the top of Hole U1588A to ~1.9 g/cm^3 around 20 m CSF-B (Figure **F32**). GRA bulk density is highly variable from 20 m to the bottom of the hole due to decreases of sediment volumes in intervals of severe core expansion. Likewise, GRA bulk density also decreases with other drilling disturbances, such as cracks, voids, soupy textures, and basal flow-ins (see **Lithostratigraphy**). Despite significant core expansion, downhole cyclic variations are still visible on GRA bulk density data averaged over 20 points.

MAD measurements were taken as 10 cm^3 discrete samples at a sampling resolution of one every 10 m from Hole U1588A cores. MAD samples were taken from fine-grained sediment while avoiding locations of noticeable drilling disturbance. These samples were measured for wet mass, dry mass, and dry volume to calculate wet density, dry density, grain density, porosity, and void ratio. The grain density is nearly constant throughout Hole U1588A, ranging 2.71–2.83 g/cm^3. The measured bulk densities from the discrete samples range 1.57–2.01 g/cm^3 and show a gradual downhole increase in bulk density (Figure **F32**). Overall, the downhole increasing trends of both GRA and MAD bulk densities are likely attributed to sediment compaction.

7.2. Magnetic susceptibility

MS was measured on all whole-round cores using the WRMSL and STMSL at 2 or 4 cm resolution (Figure **F33**). In addition, split core MSP measurements were carried out on all archive halves using the SHMSL. Three different resolutions were used for the MSP measurements: 2 cm for all cores from Hole U1588A and Cores 397-U1588B-1H through 9H, 4 cm for Sections 10X-1 through 10X-3, and 5 cm for all subsequent sections from Holes U1588B–U1588D. The measured MS is characterized by cyclic variations from tens of centimeters to a few meters.

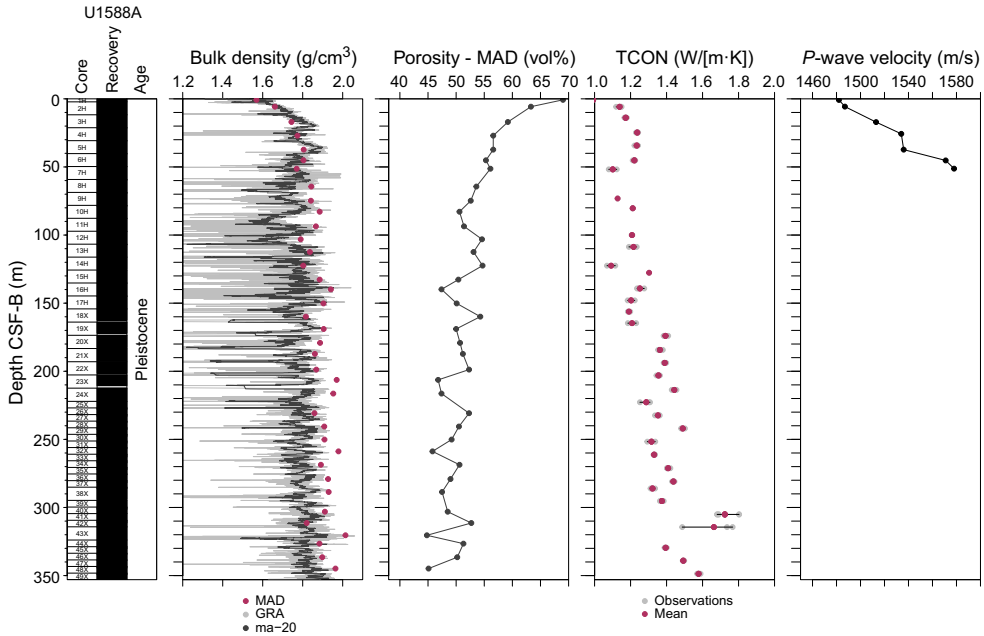

Figure F32. GRA and MAD bulk density, porosity, thermal conductivity (TCON), and *P*-wave velocity (PWC), Hole U1588A. ma-20 = moving average of 20 points.

The overall downhole trends at Site U1588 include two main intervals: a reduction of MS values from ~90 to ~15 IU with decreasing amplitude of cyclic variations from 20 to 100 m CSF-B and a consistently low MS signal of ~15 IU from 100 to 350 m CSF-B (Figure **F33**). The decreased MS in the upper 100 m is synchronous with decreased sulfate concentrations in IW due to sulfate reduction and is accompanied by increased methane concentrations (see **Geochemistry**). MS values are generally relatively higher in darker layers, showing quasiperiodic variation throughout the hole.

Whole-round MS data for all holes were acquired before the cores were equilibrated to room temperature, which may result in underestimation of MS absolute values. It is therefore recommended that postcruise quantitative analyses should use section-half MS data (MSP) because they are expected to be the most accurate MS measurements.

7.3. Porosity

Porosity was calculated using the MAD measurements of 10 cm^3 discrete samples taken at a sampling resolution of one per core for all Hole U1588A cores. Porosity ranges 44.8%–69% and decreases gradually with depth. At the top of the sediment, porosity is 69% (0.73 m CSF-B), and then it reaches <55% below 65 m CSF-B (Figure **F32**). The decreasing porosity downhole trend primarily reflects compaction and dewatering of the sediment.

7.4. *P*-wave velocity

PWC measurements were attempted at a resolution of one per core for all Hole U1588A cores; however, only the data from Cores 1H–7H are reliable because of significant core expansion below Core 8H. The *P*-wave velocity acquired with the PWC shows a steady increase from 1482 m/s at the top of the hole to 1578 m/s at 51 m CSF-B (Figure **F32**). The gradually increasing *P*-wave velocity reflects the compaction of sediments with depth in the upper 50 m.

7.5. Natural gamma radiation

NGR measurements were made with the Natural Gamma Radiation Logger (NGRL) on all core sections from all holes at a 10 or 20 cm resolution and analyzed with an integration time of 300 s/measurement. Most NGR values range 30–55 counts/s with clear cyclicity in intensity for the

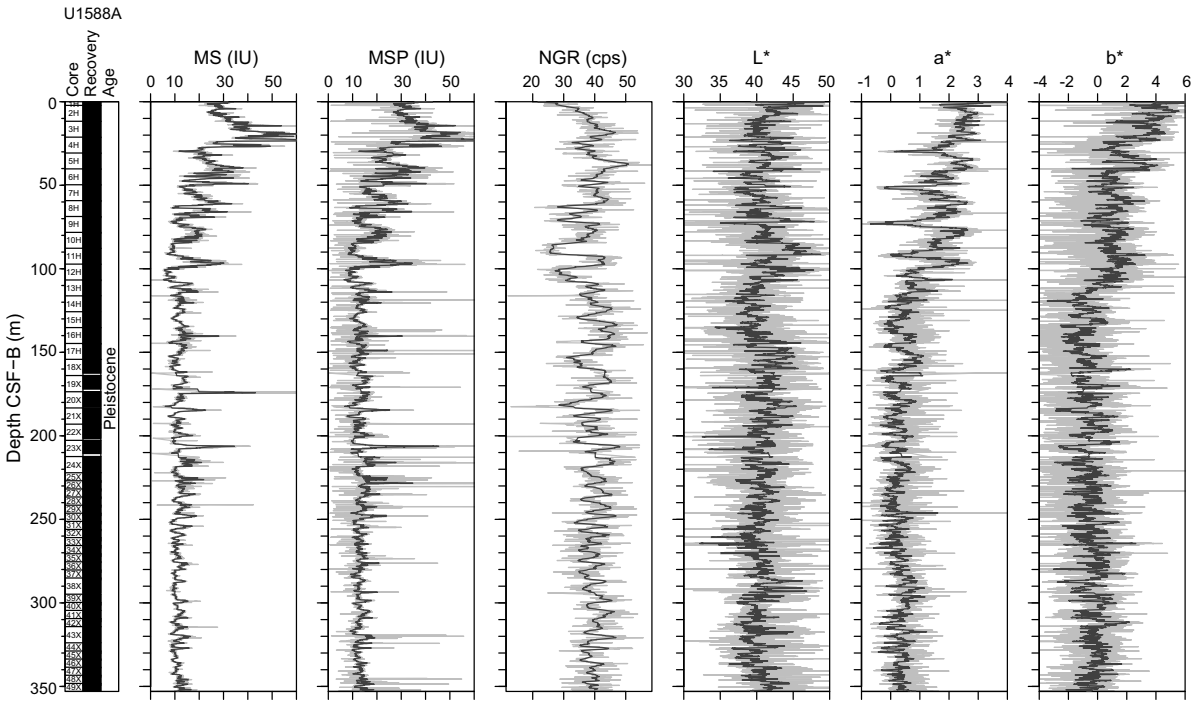

Figure F33. MS (WRMSL), MSP (SHMSL), NGR, and L*a*b* values, Hole U1588A. Solid lines = moving average of 20 points, cps = counts per second.

majority of the cores (Figure **F33**). The NGR values downhole are relatively constant and decrease in amplitude below 100 m CSF-B.

The cyclic variation of NGR intensity correlates with MS and mirrors L* values (Figure **F33**). Because L* is often related to the carbonate content in sediment (see **Geochemistry**), a higher carbonate content likely explains the low NGR and MS signals. That is, sediment physical properties parameters such as MS and NGR are closely tied to changes in lithology. Lower NGR and MS values can be interpreted as sediments dominated by calcareous microfossils (nannofossil ooze), whereas higher NGR and MS are interpreted as sediments with higher clay content (e.g., clayey nannofossil ooze).

Concentrations of K, Th, and U were calculated from the NGR spectra using the method of De Vleeschouwer et al. (2017). Downhole trends of K, Th, and U are similar to that of NGR in Hole U1588A (Figure **F34**). U/Th and K/Th ratios are essentially constant throughout the hole.

7.6. Thermal conductivity

Thermal conductivity was measured in triplicate at one position every 10 m CSF-B from all Hole U1588A cores using a needle probe on whole rounds (Cores 1H–19X) and a mini-puck sensor on the split core surface of working halves (Cores 20X–49X). Thermal conductivity ranges 1.01–1.72 W/(m·K), showing an increasing trend with depth (Figure **F32**), which is similar to the patterns of MAD bulk density.

7.7. Color reflectance

Color reflectance spectrophotometry measurements were carried out on all archive halves using the SHMSL. Three measurement resolutions were used: 2 cm for all cores from Hole U1588A and Cores 397-U1588B-1H through 9H, 4 cm for Sections 10X-1 through 10X-3, and 5 cm for all subsequent sections from Holes U1588B–U1588D.

The values of a* and b* decrease at ~100 m CSF-B in Hole U1588A and are then stable from 120 m CSF-B to the bottom of the hole (Figure **F33**).

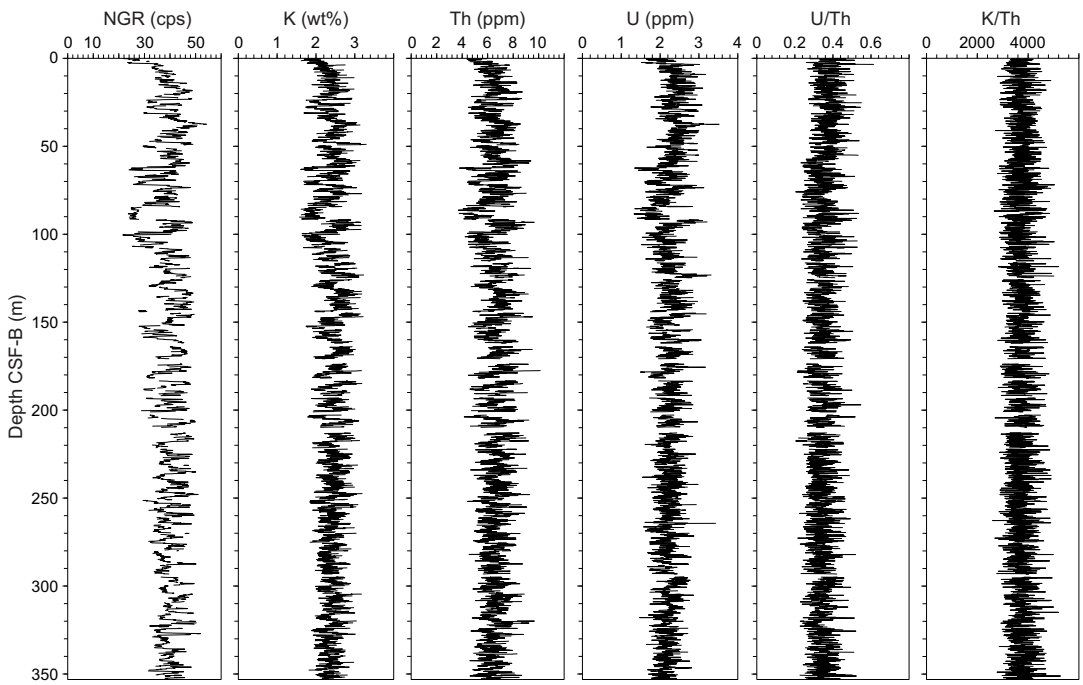

Figure F34. NGR; and K, Th, and U deconvolved and extracted from NGR spectra; and U/Th and K/Th ratios, Hole U1588A. All data from section edges (top and bottom) were eliminated. cps = counts per second.

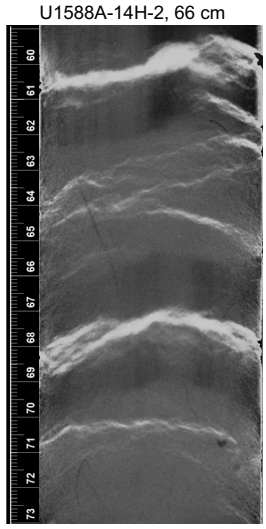

Figure F35. Whole-round X-ray image of extreme gas expansion, Hole U1588A.

L* values are negatively correlated with NGR (Figure **F33**). Calcium carbonate concentrations (see **Geochemistry**) are high in intervals where L* values are high, suggesting that the change in sediment lightness is related to the carbonate content. Carbonate content in the sediment can be affected in one of two ways: either through the dilution of potassium- and thorium-bearing detrital material (clay) by varying carbonate contents, or conversely, through the dilution of carbonate by varying detrital mineral flux (Thomson et al., 1999).

7.8. X-ray imaging

All whole-round sections from Hole U1588A (0–353.0 m CSF-B) and Cores 397-U1588D-64X through 76X (347.3–412.5 m CSF-B) were imaged using the X-Ray Logger (XMAN). The X-ray images revealed the presence of authigenic mineral grains and the morphology of lithologic contacts, burrows, and drilling disturbances such as biscuits and gas expansion. The gas expansion deformation was imaged on Cores 397-U1588A-4H through 49X, with the most extreme gas expansion disturbance observed for Cores 6H and 24X (Figure **F35**). The disturbance caused by gas expansion was still present but decreased significantly for Cores 25X–49X after transitioning to half-length XCB coring. Authigenic mineral grains, likely pyrite, were found throughout the entire depth range of Hole U1588A.

8. Downhole measurements

8.1. In situ temperature and heat flow

Four downhole temperature measurements were made in Hole U1588A using the APCT-3 tool. The calculated in situ sediment temperatures ranged from 12.12°C at 30.7 m CSF-A to 14.88°C at 116.2 m CSF-A (Table **T28**), resulting in a geothermal gradient of 33.2°C/km (Figure **F36**). The bottom water temperature (mudline temperature) averages 10.78°C and is calculated from the minimum temperatures of the four APCT-3 profiles. In situ thermal conductivity was estimated using methods described in **Physical properties** in the Expedition 397 methods chapter (Abrantes et al., 2024a). Thermal resistance was calculated by cumulatively adding the inverse of the in situ thermal conductivity values from 0 to 110 m CSF-A (Figure **F36**). A calculated heat flow of 37.8 mW/m^2 for Hole U1588A was obtained from the slope of the linear fit to the in situ temperature versus thermal resistance (Figure **F36**) (cf. Pribnow et al., 2000). This value is comparable but slightly lower than the heat flows of 49.6 mW/m^2 at Site U1587 (see **Downhole measurements** in the Site U1587 chapter [Hodell et al., 2024]) and 47.5 mW/m^2 at Site U1385 (Expedition 339 Scientists, 2013), and it is also slightly lower than the heat flow range (45–76 mW/m^2) reported for the Portuguese margin (Grevemeyer et al., 2009).

Table T28. APCT-3 results, Site U1588. **Download table in CSV format.**

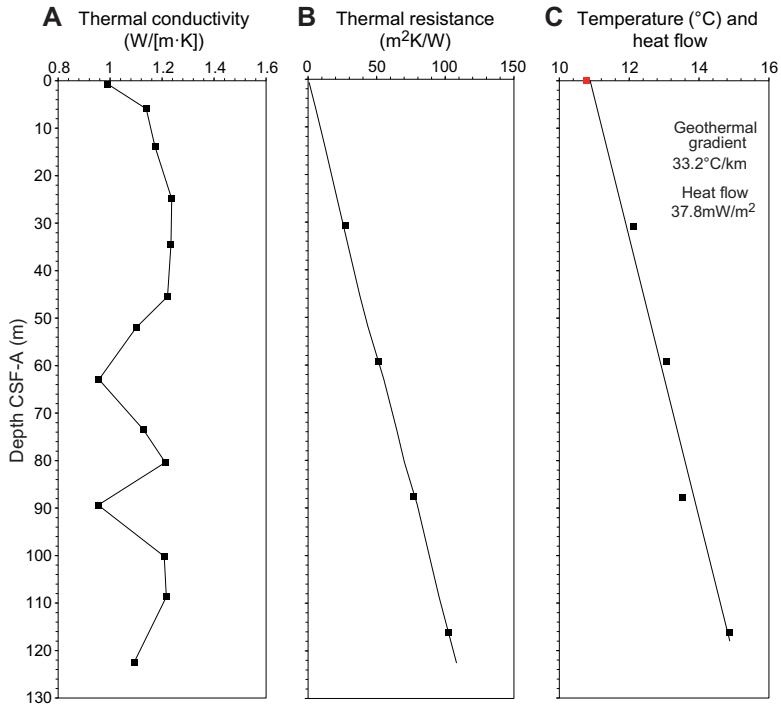

Figure F36. APCT-3 plots of heat flow calculations, Hole U1588A. A. Downcore thermal conductivity data. B. Thermal resistance calculated from thermal conductivity measurements. C. In situ APCT-3 data for Cores 4H, 7H, 10H, and 13H. Red square = average value of minimum mudline temperatures.

9. Stratigraphic correlation

Correlations between holes at Site U1588 were accomplished using Correlator software (version 4.0.1). Tie points were established using the MS from the WRMSL and NGR (Figure **F37**; Table **T29**). We constructed a splice from 0 to 366 m core composite depth below seafloor, Method B (CCSF-B), using Holes U1588A–U1588D (Figures **F37**, **F38**, **F39**; Table **T30**). The drilling and correlation strategies were unique at this site because of severely expanded cores. A mixture of APC, full-advance XCB, and half-advance XCB coring was used for different degrees of core expansion at each hole. Core expansion due to high methane contents presented a challenge to creating a composite section. Instead of the standard core composite depth below seafloor, Method A (CCSF-A), depth scale, the CSF-B depth scale was used for the correlation to compensate for apparent recoveries of up to 192%. For CSF-B, the core top is set to the driller's depth and core recovery was compressed to the nominal driller's penetration. Considering the high quality XCB cores and the high sedimentation rate at this site, the composite section (CCSF-B) is nearly complete with one potential small gap.

9.1. Approach

The CCSF-B depth scale is anchored to the mudline of Core 397-U1588B-1H, which is assigned the depth of 0 m CSF-A. From this anchor, we worked downhole using Correlator to establish a composite stratigraphy on a core-by-core basis using the CSF-B (compressed) scale. Our general approach was to avoid placing ties (1) near the section breaks as much as possible and (2) in sections where whole-round samples were taken for IW (only done throughout Hole U1588A). We also avoided full-advance XCB cores (397-U1588A-18X through 24X, 38X, and 43X) because these extruded sediment out of the core liners substantially.

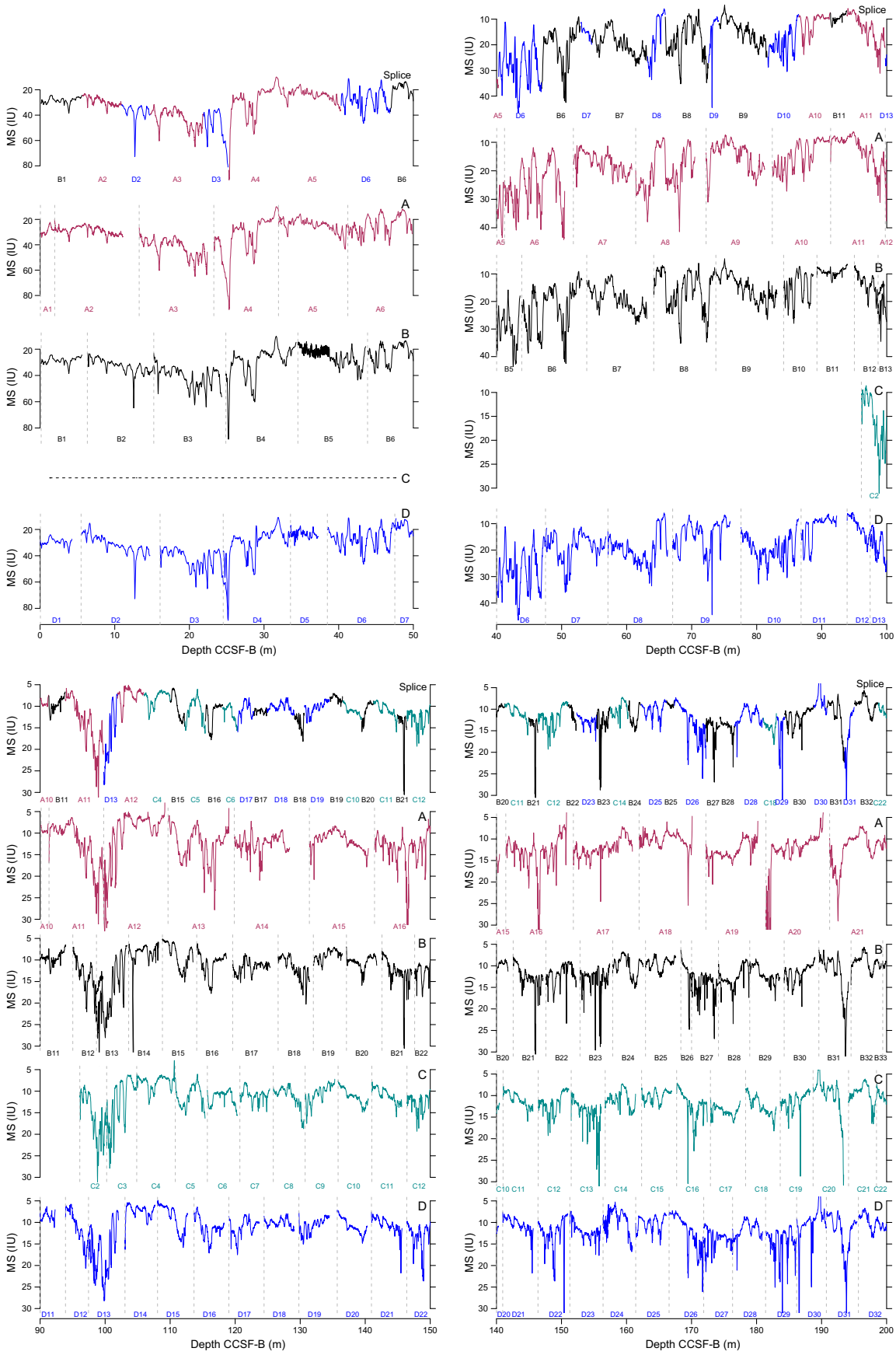

Figure F37. Composite section construction using MS in 50 m CCSF-B intervals, Site U1588. (Continued on next page.)

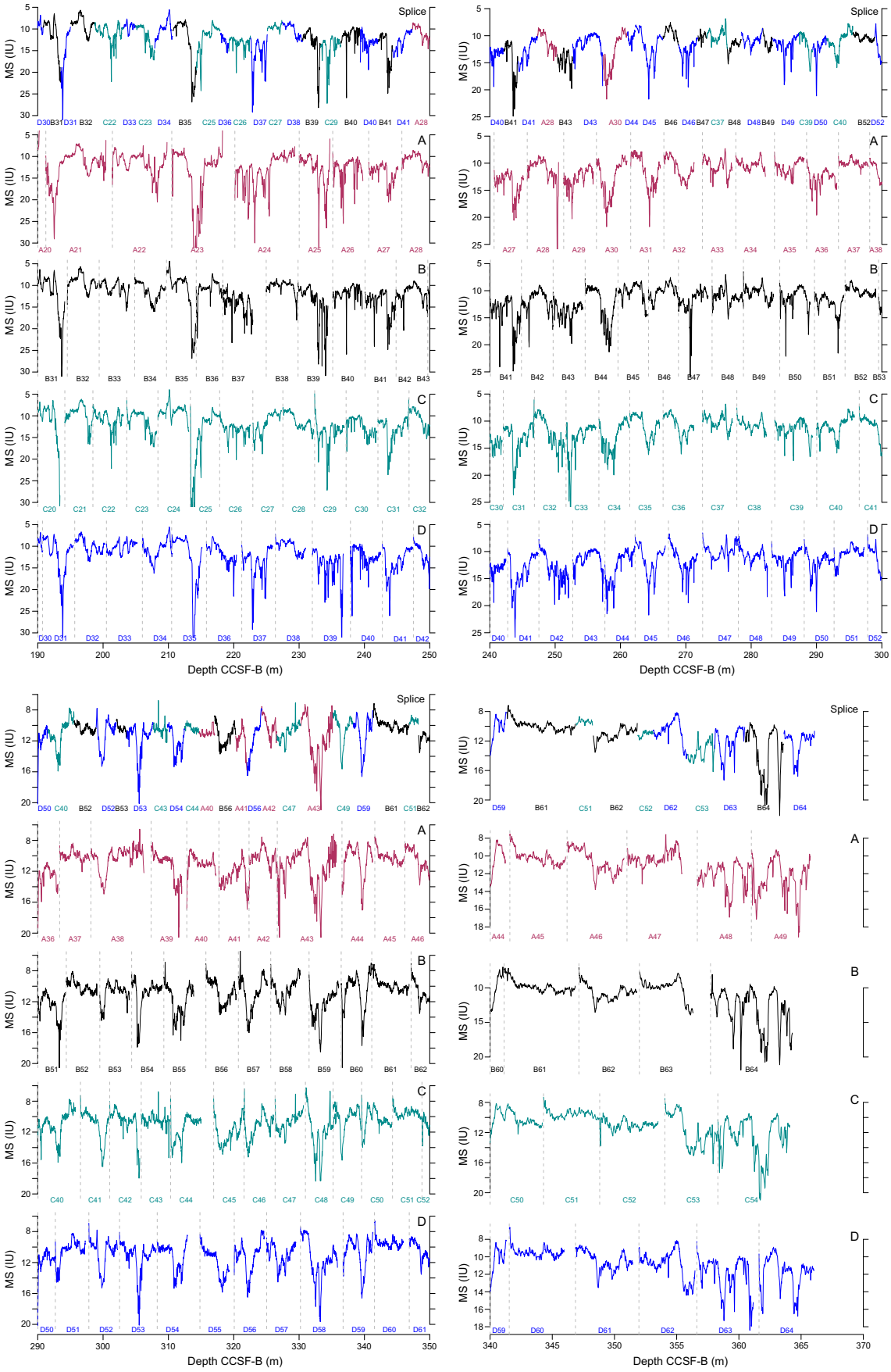

Figure F37 (continued).

A major aid in correlation came from strong, high-frequency variability in all proxy signals (MS, NGR, and color reflectance) (Figure **F38**). Fundamentally, all are controlled to first order by calcium carbonate content. After removing the spurious points at section edges in NGR, we found it especially useful when the noise of MS varies largely between holes.

9.2. Gaps

Because of the high quality XCB cores and the high sedimentation rate at this site, the composite section is overall robust with one potential small gap where the tie is uncertain. This is the tie point from Cores 397-U1588B-49X to 397-U1588D-49X in the splice, which affects Cores 397-U1588A-34X through 35X, 397-U1588B-49X through 50X, 397-U1588C-38X through 39X, and 397-U1588D-48X through 49X. In spite of the large gas expansion evident, gaps between cores are surprisingly small.

Table T29. Affine table, Site U1588. **Download table in CSV format.**

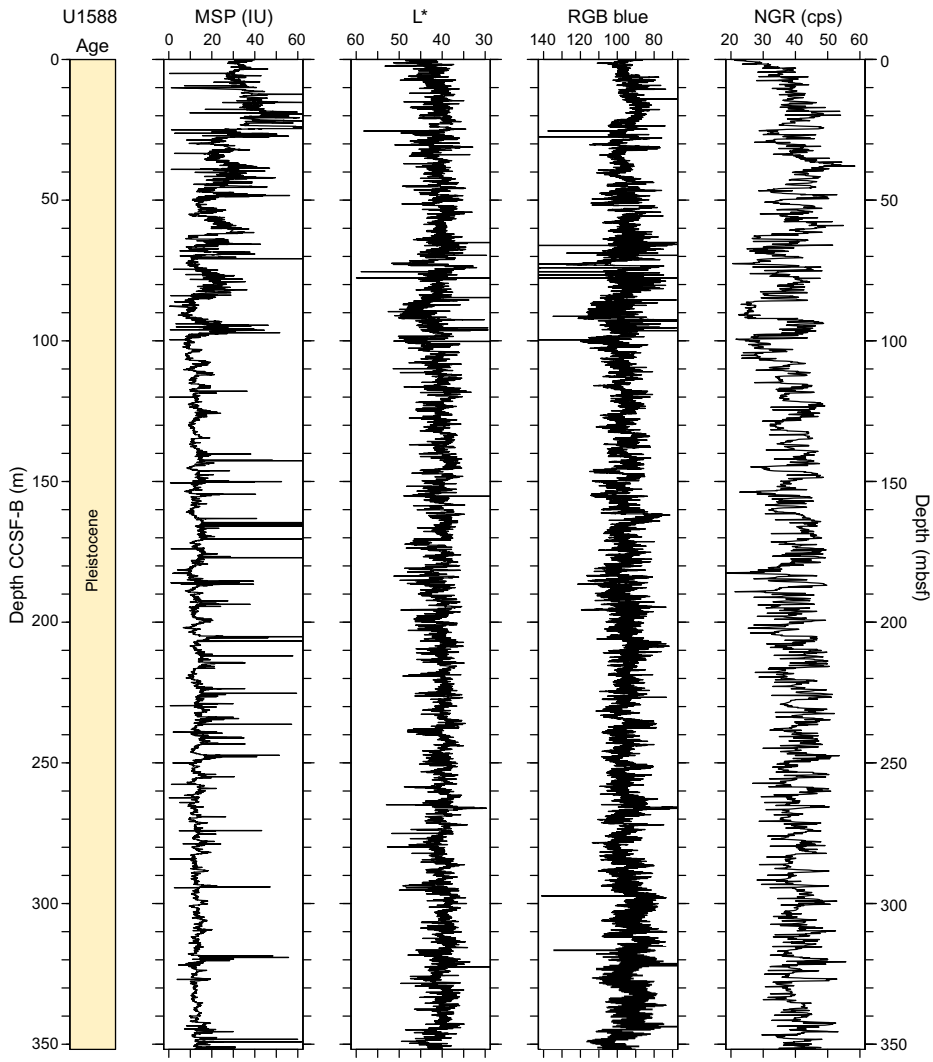

Figure F38. Spliced composite records of WRSML MS, L* color reflectance, RGB blue, and NGR, Site U1588 (CCSF-B* depth scale). The composite ends at the last tie between Holes U1588B, U1588C, and U1588D; Hole U1588D extends to 415 m (driller's depth). cps = counts per second.

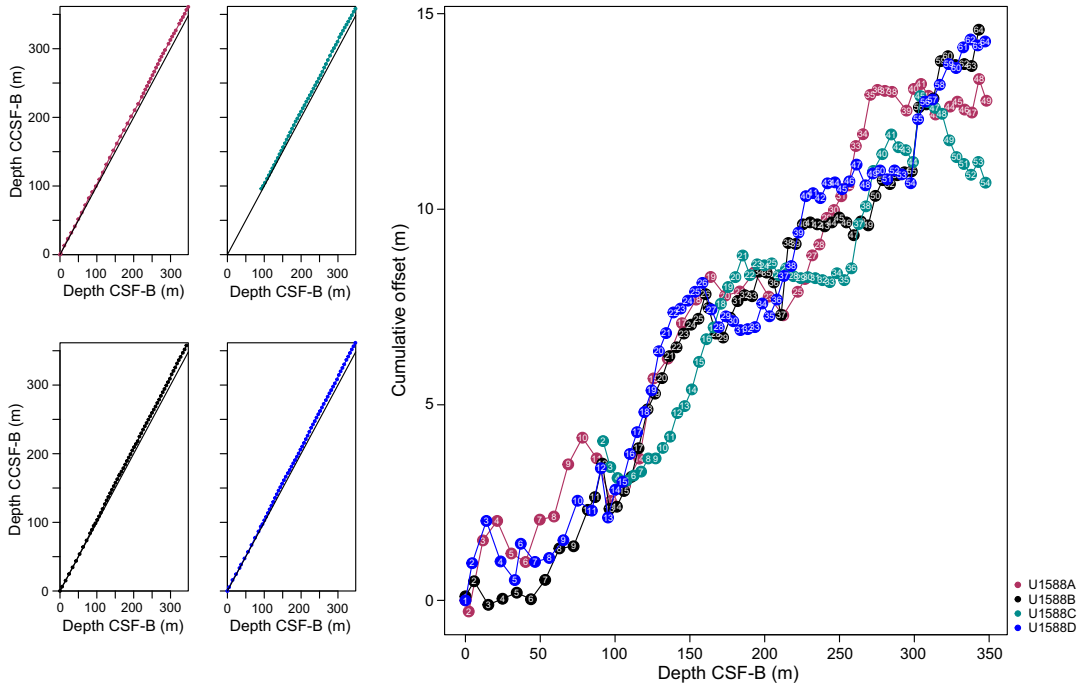

Figure F39. Depth scales, Site U1588. Left: comparison of CSF-B and CCSF-B depth scales. A 1:1 line is shown for comparison. Right: comparison of the growth of cumulative depth offset and CSF-B depth scale.

Table T30. Splice table, Site U1588. **Download table in CSV format.**

9.3. Growth rate and cumulative offset

The CSF-B depth scale compresses the core depth back to the driller's depth. The cumulative offset between the CSF-B and CCSF-B depth scales grows nearly linearly for Holes U1588A–U1588D to ~100 m CSF-B (Figure **F39**, left). The growth factor averages 1.026% but varies by core and hole. There are small changes in the growth factor and therefore in the cumulative offset with depth (Figure **F39**, right). Calculation of mass accumulation rates based on the recalculated meters below seafloor (mbsf*) depth scale (Expedition 339 Scientists, 2013) should account for differential expansion by dividing apparent depth intervals by the appropriate growth factor.

References

Abrantes, F., 1991a. Increased upwelling off Portugal during the last glaciation: diatom evidence. Marine Micropaleontology, 17(3–4):285–310. **https://doi.org/10.1016/0377-8398(91)90017-Z**

Abrantes, F., 2000. 200,000 yr diatom records from Atlantic upwelling sites reveal maximum productivity during LGM and a shift in phytoplankton community structure at 185 000 yr. Earth and Planetary Science Letters, 176(1):7–16. **https://doi.org/10.1016/S0012-821X(99)00312-X**

Abrantes, F.F., 1991b. Variability of upwelling off NW Africa during the Latest Quaternary: Diatom Evidence. Paleoceanography, 6(4):431–460. **https://doi.org/10.1029/91PA00049**

Abrantes, F., Hodell, D.A., Alvarez Zarikian, C.A., Brooks, H.L., Clark, W.B., Dauchy-Tric, L.F.B., dos Santos Rocha, V., Flores, J.-A., Herbert, T.D., Hines, S.K.V., Huang, H.-H.M., Ikeda, H., Kaboth-Bahr, S., Kuroda, J., Link, J.M., McManus, J.F., Mitsunaga, B.A., Nana Yobo, L., Pallone, C.T., Pang, X., Peral, M.Y., Salgueiro, E., Sanchez, S., Verma, K., Wu, J., Xuan, C., and Yu, J., 2024a. Expedition 397 methods. In Hodell, D.A., Abrantes, F., Alvarez Zarikian, C.A., and the Expedition 397 Scientists, Iberian Margin Paleoclimate. Proceedings of the International Ocean Discovery Program, 397: College Station, TX (International Ocean Discovery Program). **https://doi.org/10.14379/iodp.proc.397.102.2024**

Abrantes, F., Hodell, D.A., Alvarez Zarikian, C.A., Brooks, H.L., Clark, W.B., Dauchy-Tric, L.F.B., dos Santos Rocha, V., Flores, J.-A., Herbert, T.D., Hines, S.K.V., Huang, H.-H.M., Ikeda, H., Kaboth-Bahr, S., Kuroda, J., Link, J.M., McManus, J.F., Mitsunaga, B.A., Nana Yobo, L., Pallone, C.T., Pang, X., Peral, M.Y., Salgueiro, E., Sanchez, S., Verma, K., Wu, J., Xuan, C., and Yu, J., 2024b. Site U1586. In Hodell, D.A., Abrantes, F., Alvarez Zarikian, C.A., and the Expedition 397 Scientists, Iberian Margin Paleoclimate. Proceedings of the International Ocean Discovery Pro-

gram, 397: College Station, TX (International Ocean Discovery Program). **https://doi.org/10.14379/iodp.proc.397.103.2024**

Abrantes, F., Rodrigues, T., Ventura, C., Santos, C., Roell, U., Voelker, A., and Hodell, D., 2017. Past productivity conditions off SW Iberia at the transition from the 41 ky to the 100 ky world: the record of IODP Sites U1385 and U1391. Geophysical Research Abstracts, 19:EGU2017-9743. **https://meetingorganizer.copernicus.org/EGU2017/EGU2017-9743.pdf**

Balestra, B., Flores, J.A., Hodell, D.A., Hernández Molina, F.J., and Stow, D.A.V., 2015. Pleistocene calcareous nannofossil biochronology at IODP Site U1385 (Expedition 339). Global and Planetary Change, 135:57–65. **https://doi.org/10.1016/j.gloplacha.2015.10.004**

Blum, P., 1997. Physical properties handbook: a guide to the shipboard measurement of physical properties of deep-sea cores. Ocean Drilling Program Technical Note, 26. **https://doi.org/10.2973/odp.tn.26.1997**

De Vleeschouwer, D., Dunlea, A.G., Auer, G., Anderson, C.H., Brumsack, H., de Loach, A., Gurnis, M.C., Huh, Y., Ishiwa, T., Jang, K., Kominz, M.A., März, C., Schnetger, B., Murray, R.W., Pälike, H., and Expedition 356 Shipboard Scientists, 2017. Quantifying K, U, and Th contents of marine sediments using shipboard natural gamma radiation spectra measured on DV JOIDES Resolution. Geochemistry, Geophysics, Geosystems, 18(3):1053–1064. **https://doi.org/10.1002/2016GC006715**

Expedition 339 Scientists, 2013. Site U1385. In Stow, D.A.V., Hernández-Molina, F.J., Alvarez Zarikian, C.A., and the Expedition 339 Scientists, Proceedings of the Integrated Ocean Drilling Program. 339: Tokyo (Integrated Ocean Drilling Program Management International, Inc.). **https://doi.org/10.2204/iodp.proc.339.103.2013**

Gradstein, F.M., Ogg, J.G., Schmitz, M.D., and Ogg, G.M. (Eds.), 2020. The Geologic Time Scale 2020: Amsterdam (Elsevier BV). **https://doi.org/10.1016/C2020-1-02369-3**

Grevemeyer, I., Kaul, N., and Kopf, A., 2009. Heat flow anomalies in the Gulf of Cadiz and off Cape San Vincente, Portugal. Marine and Petroleum Geology, 26(6):795–804. **https://doi.org/10.1016/j.marpetgeo.2008.08.006**

Hayward, B.W., 2002. Late Pliocene to middle Pleistocene extinctions of deep-sea benthic Foraminifera ("Stilostomella extinction") in the Southwest Pacific. Journal of Foraminiferal Research, 32(3):274–307. **https://doi.org/10.2113/32.3.274**

Heard, T.G., Pickering, K.T., and Clark, J.D., 2014. Ichnofabric characterization of a deep-marine clastic system: a subsurface study of the middle Eocene Ainsa System, Spanish Pyrenees. Sedimentology, 61(5):1298–1331. **https://doi.org/10.1111/sed.12101**

Hernández-Molina, F.J., Llave, E., Stow, D.A.V., García, M., Somoza, L., Vázquez, J.T., Lobo, F.J., Maestro, A., Díaz del Río, V., León, R., Medialdea, T., and Gardner, J., 2006. The contourite depositional system of the Gulf of Cádiz: A sedimentary model related to the bottom current activity of the Mediterranean outflow water and its interaction with the continental margin. Deep Sea Research Part II: Topical Studies in Oceanography, 53(11):1420–1463. **https://doi.org/10.1016/j.dsr2.2006.04.016**

Hernández-Molina, F.J., Stow, D.A.V., Alvarez-Zarikian, C.A., Acton, G., Bahr, A., Balestra, B., Ducassou, E., Flood, R., Flores, J.-A., Furota, S., Grunert, P., Hodell, D., Jimenez-Espejo, F., Kim, J.K., Krissek, L., Kuroda, J., Li, B., Llave, E., Lofi, J., Lourens, L., Miller, M., Nanayama, F., Nishida, N., Richter, C., Roque, C., Pereira, H., Sanchez Goñi, M.F., Sierro, F.J., Singh, A.D., Sloss, C., Takashimizu, Y., Tzanova, A., Voelker, A., Williams, T., and Xuan, C., 2014. Onset of Mediterranean outflow into the North Atlantic. Science, 344(6189):1244–1250. **https://doi.org/10.1126/science.1251306**

Hernández-Molina, J., Llave, E., Somoza, L., Fernández-Puga, M.C., Maestro, A., León, R., Medialdea, T., Barnolas, A., García, M., Díaz del Río, V., Fernández-Salas, L.M., Vázquez, J.T., Lobo, F., Alveirinho Dias, J.M., Rodero, J., and Gardner, J., 2003. Looking for clues to paleoceanographic imprints: a diagnosis of the Gulf of Cadiz contourite depositional systems. Geology, 31(1):19–22. **https://doi.org/10.1130/0091-7613(2003)031%3C0019:LFCTPI%3E2.0.CO;2**

Hodell, D.A., Abrantes, F., Alvarez Zarikian, C.A., Brooks, H.L., Clark, W.B., Dauchy-Tric, L.F.B., dos Santos Rocha, V., Flores, J.-A., Herbert, T.D., Hines, S.K.V., Huang, H.-H.M., Ikeda, H., Kaboth-Bahr, S., Kuroda, J., Link, J.M., McManus, J.F., Mitsunaga, B.A., Nana Yobo, L., Pallone, C.T., Pang, X., Peral, M.Y., Salgueiro, E., Sanchez, S., Verma, K., Wu, J., Xuan, C., and Yu, J., 2024. Site U1587. In Hodell, D.A., Abrantes, F., Alvarez Zarikian, C.A., and the Expedition 397 Scientists, Iberian Margin Paleoclimate. Proceedings of the International Ocean Discovery Program, 397: College Station, TX (International Ocean Discovery Program). **https://doi.org/10.14379/iodp.proc.397.104.2024**

Hodell, D.A., Crowhurst, S.J., Lourens, L., Margari, V., Nicolson, J., Rolfe, J.E., Skinner, L.C., Thomas, N.C., Tzedakis, P.C., Mleneck-Vautravers, M.J., and Wolff, E.W., 2023. A 1.5-million-year record of orbital and millennial climate variability in the North Atlantic. Climate of the Past, 19(3):607–636. **https://doi.org/10.5194/cp-19-607-2023**

Kawagata, S., Hayward, B.W., Grenfell, H.R., and Sabaa, A., 2005. Mid-Pleistocene extinction of deep-sea foraminifera in the North Atlantic Gateway (ODP Sites 980 and 982). Palaeogeography, Palaeoclimatology, Palaeoecology, 221(3):267–291. **https://doi.org/10.1016/j.palaeo.2005.03.001**

Laprida, C., Carbonel, P., and Azpilicueta, M., 2002. Dinámica de los ostrácodos mediterráneos en el golfo de Vizcaya, océano Atlántico nororiental. Revista Espanola de Micropaleontologia, 34(2):201–214.

Llave, E., Schönfeld, J., Hernández-Molina, F.J., Mulder, T., Somoza, L., Díaz del Río, V., and Sánchez-Almazo, I., 2006. High-resolution stratigraphy of the Mediterranean outflow contourite system in the Gulf of Cadiz during the late Pleistocene: The impact of Heinrich events. Marine Geology, 227(3):241–262. **https://doi.org/10.1016/j.margeo.2005.11.015**

Martini, E., 1971. Standard Tertiary and Quaternary calcareous nannoplankton zonation. Proceedings of the Second Planktonic Conference, Roma, 1970:739–785.

Meyers, P.A., 1994. Preservation of elemental and isotopic source identification of sedimentary organic matter. Chemical Geology, 114(3–4):289–302. **https://doi.org/10.1016/0009-2541(94)90059-0**

Meyers, P.A., 1997. Organic geochemical proxies of paleoceanographic, paleolimnologic, and paleoclimatic processes. Organic Geochemistry, 27(5–6):213–250. **https://doi.org/10.1016/S0146-6380(97)00049-1**

Okada, H., and Bukry, D., 1980. Supplementary modification and introduction of code numbers to the low-latitude coccolith biostratigraphic zonation (Bukry, 1973; 1975). Marine Micropaleontology, 5(3):321–325. **https://doi.org/10.1016/0377-8398(80)90016-X**

Paytan, A., and Griffith, E.M., 2007. Marine barite: recorder of variations in ocean export productivity. Deep Sea Research, Part II: Topical Studies in Oceanography, 54(5–7):687–705. **https://doi.org/10.1016/j.dsr2.2007.01.007**

Pribnow, D.F.C., Kinoshita, M., and Stein, C.A., 2000. Thermal data collection and heat flow recalculations for ODP Legs 101–180: Hannover, Germany (Institute for Joint Geoscientific Research, GGA). **http://www-odp.tamu.edu/publications/heatflow/**

Raffi, I., Backman, J., Fornaciari, E., Pälike, H., Rio, D., Lourens, L., and Hilgen, F., 2006. A review of calcareous nannofossil astrobiochronology encompassing the past 25 million years. Quaternary Science Reviews, 25(23):3113–3137. **https://doi.org/10.1016/j.quascirev.2006.07.007**

Reitz, A., Pfeifer, K., de Lange, G.J., and Klump, J., 2004. Biogenic barium and the detrital Ba/Al ratio: a comparison of their direct and indirect determination. Marine Geology, 204(3–4):289–300. **https://doi.org/10.1016/S0025-3227(04)00004-0**

Thomson, J., Nixon, S., Summerhayes, C.P., Rohling, E.J., Schönfeld, J., Zahn, R., Grootes, P., Abrantes, F., Gaspar, L., and Vaquiero, S., 2000. Enhanced productivity on the Iberian margin during glacial/interglacial transitions revealed by barium and diatoms. Journal of the Geological Society, 157(3):667–677. **https://doi.org/10.1144/jgs.157.3.667**

Thomson, J., Nixon, S., Summerhayes, C.P., Schönfeld, J., Zahn, R., and Grootes, P., 1999. Implications for sedimentation changes on the Iberian margin over the last two glacial/interglacial transitions from (230Thexcess)0 systematics. Earth and Planetary Science Letters, 165(3):255–270. **https://doi.org/10.1016/S0012-821X(98)00265-9**

Ventura, C., Abrantes, F., Loureiro, I., and Voelker, A.H.L., 2017. Data report: diatom and silicoflagellate records of marine isotope stages 25–27 at IODP Site U1387, Faro Drift. In Stow, D.A.V., Hernández-Molina, F.J., Alvarez Zarikian, C.A., and the Expedition 339 Scientists, Proceedings of the Integrated Ocean Drilling Program. 339: Tokyo (Integrated Ocean Drilling Program Management International, Inc.). **https://doi.org/10.2204/iodp.proc.339.202.2017**

Wade, B.S., Pearson, P.N., Berggren, W.A., and Pälike, H., 2011. Review and revision of Cenozoic tropical planktonic foraminiferal biostratigraphy and calibration to the geomagnetic polarity and astronomical time scale. Earth-Science Reviews, 104(1–3):111–142. **https://doi.org/10.1016/j.earscirev.2010.09.003**

Wu, J., Böning, P., Pahnke, K., Tachikawa, K., and de Lange, G.J., 2016. Unraveling North-African riverine and eolian contributions to central Mediterranean sediments during Holocene sapropel S1 formation. Quaternary Science Reviews, 152:31–48. **https://doi.org/10.1016/j.quascirev.2016.09.029**

Xuan, C., and Channell, J.E.T., 2009. UPmag: MATLAB software for viewing and processing u channel or other pass-through paleomagnetic data. Geochemistry Geophysics Geosystems, 10:Q10Y10. **https://doi.org/10.1029/2009GC002584**

Zitellini, N., Gràcia, E., Matias, L., Terrinha, P., Abreu, M.A., DeAlteriis, G., Henriet, J.P., Dañobeitia, J.J., Masson, D.G., Mulder, T., Ramella, R., Somoza, L., and Diez, S., 2009. The quest for the Africa–Eurasia plate boundary west of the Strait of Gibraltar. Earth and Planetary Science Letters, 280(1–4):13–50. **https://doi.org/10.1016/j.epsl.2008.12.005**